Progress of Surface Science Studies on ABX(3)-Based Metal Halide Perovskite Solar Cells

Author	Longbin Qiu, Sisi He, Luis K. Ono, Yabing Qi
journal or publication title	Advanced Energy Materials
volume	10
number	13
page range	1902726
year	2019-10-17
Publisher	John Wiley & Sons
Rights	(C) 2019 WILEY-VCH Verlag GmbH & Co. KGaA, Weinheim This is the peer reviewed version of the following article: Qiu, L., He, S., Ono, L. K., Qi, Y. B., Progress of Surface Science Studies on ABX3‐Based Metal Halide Perovskite Solar Cells. Adv. Energy Mater. 2020, 10, 1902726., which has been published in final form at https://doi.org/10.1002/aenm.201902726. This article may be used for non-commercial purposes in accordance with Wiley Terms and Conditions for Use of Self-Archived Versions.
Author's flag	author
URL	http://id.nii.ac.jp/1394/00001247/

doi: info:doi/10.1002/aenm.201902726

Progress of Surface Science Studies on ABX_3 Based Metal Halide Perovskite Solar Cells

*Longbin Qiu†, Sisi He†, Luis K. Ono†, Yabing Qi**

Dr. L. Qiu, Dr. S. He, Dr. L. K. Ono, Prof. Y. B. Qi
Energy Materials and Surface Sciences Unit (EMSSU), Okinawa Institute of Science and Technology Graduate University (OIST), 1919-1 Tancha, Onna-son, Kunigami-gun, Okinawa 904-0495, Japan.
*Corresponding author: Yabing Qi, E-Mail: Yabing.Qi@OIST.jp
†These authors contributed equally to this work.

Keywords: microstructure, energy level alignment, defect state, passivation, operando

ABX_3 type metal halide perovskite solar cells (PSCs) have shown performance over 25%, which is rocketing towards its limit. To gain the full potential of PSCs relies on the understanding of device working mechanisms and recombination, the material quality and the match of energy levels in the device stacks. In this progress report, we presented the importance of designing of PSCs from the viewpoint of surface/interface science studies. For this purpose, we first present recent case studies to demonstrate how probing of local heterogeneities (e.g., grains, grain boundaries, atomic structure, etc.) in perovskites by surface science techniques can help correlate the PSC parameters. At the solar cell device level that has active areas larger than the millimeter scale, the ensemble average measurement techniques can characterize the overall averaged properties of perovskite films as well as their adjacent layers and provides clues to understand better the solar cell parameters. How the generation/healing of electronic defects in perovskite will limit the device efficiency, reproducibility and stability and also induce the time-dependent behavior of J-V curves are also the focus of this report. On the basis of these studies, we propose the strategies to further improve efficiency and stability, meanwhile reduce hysteresis.

1. Introduction

Metal halide perovskites with the ABX_3 (here A = MA^+ ($CH_3NH_3^+$), FA^+ ($CH(NH_2)_2^+$), Cs^+ or mixed A-cations; B = Pb^{2+} or Sn^{2+} or mixed B-cations; X = I^-, Br^- or Cl^- or mixed X-anions) structure have been developed and show a great potential for future solar energy applications. It has been reported that theoretically, perovskite solar cells (PSCs) could attain efficiency of 30% with a single junction structure,[1] which is higher than silicon solar cells (29.1%).[2] PSCs have reached efficiency up to 25.2%, which is already higher than polycrystalline silicon solar cells (22.3%) and other thin film solar cells like CdTe solar cells (22.1%) and approaching the record of silicon solar cells of 26.6%.[3] Perovskite-based large area solar modules are also growing in performance. Currently, the champion solar module with an area over 200 cm^2 shows a certified performance of 11.98%.[3] $MAPbI_3$ perovskite single crystals have also been applied for solar cells and demonstrated an efficiency over 21% aided by the low density of defect states.[4] All-inorganic perovskite materials such as $CsPbI_3$ with a band gap of 1.7 eV, the performance has been reported to be over 18%, which is promising for tandem structured devices with over 30% efficiency.[5] Tremendous efforts are being made into this field to further improve the device performance towards its thermodynamic limit. The factors that determine the device performance include the band gap, light absorbance, and charge generation and extraction. No matter whether it is a single junction or multi junction perovskite based solar cell, the surfaces/interfaces determine charge extraction and transfer, which dictates the overall performance. How to improve charge separation and reduce the non-radiative recombination is the main direction for the future performance improvements, which requires a perovskite photoactive layer and neighboring interfaces with superior opto-electronic properties and perfect energy level alignment match.

On the other hand, although the performance of PSCs is approaching silicon solar cells, several issues still need to be overcome. Surfaces/interfaces play a vital role on device performance in addition to hysteresis and stability. For example, the prevention of moisture infiltration with a several-nanometer-thick lead oxysalt coating layer on the $MAPbI_3$ perovskite single crystal was demonstrated by submersing the crystal under water for a long time.[6] Ion migration is considered as the origin for hysteresis phenomena in PSC current-voltage profiles. Understanding of complex physico-chemical dynamics at interfaces will help design interfaces that can further improve the efficiency and stability, while reduce hysteresis at the same time.

Regarding research efforts on technological aspects of device performance, improvements in perovskite film quality, interface structure, and defect passivation play a crucial role for overcoming device performance limits and increasing device stability. In this progress report, we present recent case studies to demonstrate how probing of local heterogeneities (e.g., grains, grain boundaries, atomic structure, etc.) in perovskites by surface science techniques can help correlate the PSC parameters (**Section 2**). Understanding local properties at the micro, nanometer, or even at the atomic scale is key to settling the several existing controversial issues in perovskite materials and solar cells. On the other hand, at the solar cell device level that has active areas larger than the millimeter scale, the ensemble average measurement techniques play also a pivotal role (**Section 3**). Characterization of the overall averaged properties of perovskite films as well as their adjacent layers (selective contacts and electrodes) provides clues to understand better the solar cell parameters, such as open-circuit voltage (Voc), short-circuit current density (Jsc), fill factor (FF), and power conversion efficiency (PCE). The functional layers within the solar cells under realistic operation conditions do not stay *static*, i.e., a variety of perturbations (light, built-in potential, temperature, environmental gases, and so on) lead to rich dynamical phenomena manifested in the final current density-voltage (J-V) curves such as hysteresis and transient behaviors in PCEs (enhancement and/or deterioration as a function of time). One of the fundamental origins for all of these time-dependent responses lies in the generation/healing[7] of electronic defects within the semiconductor band gap influencing efficiency, lifetime, as well as reproducibility (**Section 4**).[7a] How the local heterogeneities in perovskites evolve as a function of time and how *in operando* surface science techniques allow probing of properties changes in functional layers under PSC operation conditions are also the central focus of this progress report.

2. Local properties influencing solar cell parameters

The behavior of a solar cell J-V curve and corresponding parameters of Voc, Jsc, FF, and PCE are governed by the balance of charge carrier generation, recombination processes, transport across the bulk, and extraction at the interfaces. The device structure of a PSC is complex comprised of multiple stacked layers. For instance, the cell architecture that has led to the majority of the best certified efficiencies in the National Renewable Energy Laboratory (NREL) chart is composed of a transparent conductive oxide (photoanode), electron transport layer (ETL) including a mesoporous scaffold layer, a perovskite layer, hole transport layer (HTL), and a high work function (WF) electrode (photocathode). Among these stacked layers, the polycrystalline perovskite layer is often inherently nano/micro-structured with the presence of grain boundaries[8] and has varying chemical compositions and crystal structures/orientations (**Figure 1a**). Therefore, the film local structure is expected to influence the overall device macroscopic properties. Furthermore, under a certain stimulus (e.g., light, temperature, environment) the perovskite layer will respond dynamically (i.e., a time-dependent response behavior) impacting the overall device performance as a function of time. For example, a measurement condition may exist under which a parameter under the study (e.g., photocurrent, photovoltage, and so on) shows a transient behavior for a certain period of time and then reaches an equilibrium, i.e., a static condition. The time-scale of the responses will vary according to the physico-chemical processes (**Figure 1b,c**), for example, after free carriers are generated upon incident photons, hot carrier cooling processes take place within picoseconds, while the subsequent carrier transport and recombination processes occur within microseconds.[9] Trap states related processes (trapping, de-trapping, recombination) have the characteristic time-scale in milliseconds. Ion migration has a longer time-scale in seconds.[9] Description on (i) how the solar cell parameters (Voc, Jsc, FF, and PCE) can be correlated directly with the local heterogeneity effects employing spatially-resolved techniques as well as (ii) how these local heterogeneities evolve as a function of time are the central topics of this section. We discuss a selected number of scanning probe microscopy (SPM) with multi-modality imaging capabilities, electron microscopy, and spatially resolved optical microscopy techniques that showed feasibility in describing the spatially- and temporally-resolved phenomena (**Figure 1** and **Table 1**) in PSCs.

2.1. Photocurrent mapping

A few SPM techniques can provide insights into the photovoltaic characteristics of PSCs at the nanoscale. Conductive AFM (c-AFM) is able to map the electrical properties such as local charge distribution and charge transport (current distribution with sensitivity as high as a few pA). A variant of c-AFM, photoconductive AFM (pc-AFM), employs additionally a light beam that shines onto the sample. The local photocurrent characteristics as a response to the light-stimulus, can be mapped and correlated simultaneously with the microstructural (topography) features. The pc-AFM technique has been employed to understand the influences of grain boundaries on the photovoltaic performance.[10] While some studies found that the photoconductivity at the grain boundaries was higher compared to that of grain interiors,[10b, 10c] a few other studies reported the opposite, i.e., the photoconductivity within a grain was higher than that at the grain boundaries.[10a, 10f] These results have already shown the complexity of such studies, and the origin of this discrepancy can be due to the different sample preparation conditions, influence of the underneath functional layers and substrate, the environmental measurement conditions, the lack of consideration of the dynamics within the PSC such as ion migration, and so on.[11] Huang and co-workers[10g] conducted a systematic study employing spatially resolved local spectroscopy measurement in the dark by positioning the probe tip at the location of a grain boundary or on top of a grain interior. The hysteresis phenomenon was observed to occur majorly at the grain boundaries. In contrast, the measured dark current at the grain interiors have shown negligible hysteresis. Upon light-stimulus, a gradual increase in current (short-circuit conditions) was probed only when the pc-AFM probing tip was placed at a grain boundary. As comparison, the short-circuit current probed on the top but inside a grain remained almost unchanged. The similar conclusion was also corroborated by other works.[10a, 10g, 11-12] These microscopic studies show that the transient behavior in photocurrent in polycrystalline films are dominated by the faster ion migration within grain boundaries induced by a built-in potential. As a consequence of this movement of electrically charged species and accumulation at grain boundaries, it has been proposed that grain boundaries can be effective in separating and collecting charges, hence enhance photocurrent.[10b, 13] An alternative scenario exists, i.e., the presence of nonstoichiometric crystals and/or neutral or charged impurities at grain boundaries may also lead to the formation of localized electronic trap states within the band gap, which can act as recombination sites deteriorating the overall PSC performance.[14]

Large variations in photoconductivity are also observed when comparing the different grain interiors within the same scanning area.[10a, 15] Variations even inside a grain interior can be seen indicating heterogeneity (**Figure 1a**). These heterogeneities can be of various origins and were previously attributed to (i) facet-dependent density of trap states studied by c-AFM,[10e] (ii) PbI_2 passivation probed by light-modulated scanning tunneling microscopy (STM) and scanning tunneling spectroscopy (STS),[15] (iii) effects of additives (e.g., chlorine) leading to enhanced photoconductivity measured by c-AFM,[16] (iv) recombination losses at the interfaces studied by pc-AFM,[17] (vi) doping strategy in perovskite probed by pc-AFM,[18] passivation strategies such as pyridine[19] and thiophene[19b] leading to variations in PL mapping.

The abovementioned studies demonstrate that electronic charges upon light excitation are significantly affected by the structural and chemical heterogeneity of grain boundaries and grain interiors impacting the overall solar cell photocurrent. Further spatially-resolved mapping combined with probing of time-resolved dynamics in perovskite materials will likely obtain clearer pictures of the fundamental processes in photocurrent behaviors. Local photocurrent magnitude, which is associated with the strength and profiles in photovoltage across the stacked layers in PSCs is discussed next.

2.2. Photovoltage mapping

The photovoltage effect can be probed by Kelvin probe force microscope (KPFM) by comparing the differences in CPD values of photovoltaic films in dark and under illumination (ΔV). The value of ΔV cannot be directly converted to the value of Voc, but it provides qualitative information about the strength of the photovoltage effect. Furthermore, the ΔV magnitude is related to the density of charge carriers, while the polarity of ΔV is associated with the type of charge carriers (electrons or holes) on the surface.[10f, 13b, 20] The concepts above were also studied on $MAPbI_3$ perovskite samples when deposited on different layers of ETL (FTO/c-TiO_2/$MAPbI_3$,) and HTL (FTO/PEDOT:PSS/$MAPbI_3$, where FTO = fluorine-doped tin oxide, c-TiO_2 = compact layered TiO_2, and PEDOT:PSS = poly(3,4-ethylenedioxythiophene) polystyrene sulfonate).[10f, 13b] Considering the case of FTO/c-TiO_2/$MAPbI_3$ (half-cell in n-i-p configuration), the surface photovoltage value (SPV) difference when comparing under illumination and in dark revealed a positive shift ($\Delta V > 0$). This was rationalized on the grounds that (i) the photoexcited charge carriers in the perovskite layer are separated by the built-in field located at the $TiO_2/MAPbI_3$ interface, (ii) subsequently electrons are effectively transferred to the c-TiO_2 ETL back contact layer and to the ground of the KPFM system. (iii) Meanwhile, holes will be left in the perovskite and accumulate at the surface of the perovskite layer. The built-in field at the $TiO_2/MAPbI_3$ interface has little influence on ΔV and the electric field generated by the excess holes leads to the increase in SPVs (i.e., $\Delta V > 0$). To highlight the critical role played by the selective contact layers, charge separation and transfer were studied on FTO/PEDOT:PSS/$MAPbI_3$ (half-cell in p-i-n configuration). It is found that SPVs taken under illumination show lower values than those measured in dark.[13b] This opposite result from the $TiO_2/MAPbI_3$ sample is explained due to the preferential extraction of holes to the back contact of PEDOT:PSS. Hence, excess electrons are accumulated on the surface of the perovskite layer leading to a global reduction of potential variation ($\Delta V < 0$). The phenomenon of unbalanced charge extraction can be inferred when comparing the average differences of ΔV in ETL/perovskite and HTL/perovskite. In the experiment by Zhu and co-workers[13b], FTO/$TiO_2/MAPbI_3$ and FTO/PEDOT:PSS/$MAPbI_3$ samples showed ΔV of approximately +39 mV and −10 mV, respectively. On the basis of these ΔV values, it has been proposed that the ability of electron transfer at the TiO_2/perovskite interface is better than that of hole transfer at the PEDOT:PSS/perovskite interface.

KPFM is also widely employed to study the potential distribution across the stacks of all functional layers constituting the complete solar cell device (**Figure 1b**). The measurement of cross-section profiles in a full device can provide ample useful information but requires a clean and flat sample surface. The sample fabrication for cross-section measurements has to be handled carefully for the surface-sensitive techniques. The clean cross section can be prepared by cleaving,[21] or focused ion beam milling[12c], such that the full structure and functionality of each layer can be preserved. For PSCs typically the device side area outside the device boundary was notched and fractured by tension rather than by compression to expose the cross-section.[21-22] After cleaving the sample surface can be polished either mechanically[23] or by focus-ion beam milling.[12c] Scanning of CPD profiles on a cross-sectional surface provides key information of "buried interfaces" such as energy level alignments with adjacent layers, band bending, electronic trap states, and ionic accumulation at interfaces.[12c, 21-22, 24] The electrical potential distribution of highly performing device architecture that led to certified efficiencies in the NREL chart has been widely studied by KPFM.[25] These regular structured devices are typically composed of FTO/c-TiO_2/mp-TiO_2/perovskite/ 2,2',7,7'-tetrakis(N,N-di-p-methoxyphenyl-amine)9,9'-spirobifluorene (spiro-MeOTAD)/Au (or Ag).[21, 24b] Systematic studies by sequentially switching the light on and off revealed the dynamics of charge carriers of perovskites when in contact with the ETL and HTL interfaces. Under illumination, holes were observed to accumulate in the proximity to the HTL as a consequence of unbalanced charge transport in the device, i.e., a high rate of electron extraction at the TiO_2/perovskite interface was probed by cross-sectional KPFM. As a consequence, the accumulation of excess holes creates an electrical potential barrier reducing the overall Jsc.[22-23, 24b] These experiments show the importance of a careful choice of ETL and HTL for controlling the potential distribution within the PSC device. Not only the selective contacts, but also the chemical composition of $MAPbI_3$ perovskite (PbI_2-rich or MAI-rich) was also observed to affect the position of the potential drop where charge separation occurs (meaning the position of the diode junction).[22, 24e, 24f] The magnitude of the potential drop at the junction area is proportional to the local electric field. Therefore, a larger potential drop indicates a stronger electric field and efficient charge separation at the particular interface.[24d] CPD profiles by KPFM obtained for planar PSCs showed a significant potential drop at the c-TiO_2/$MAPbI_3$ interface. On the other hand, the PbI_2-rich device exhibited a significant potential drop at the $MAPbI_3$/spiro-MeOTAD.

In sharp contrast, regardless of the variations in perovskite stoichiometry, when the mesoporous layer of TiO_2 (mp-TiO_2) is employed, no localized potential drop was probed and all the potential drop was observed to occur within the $MAPbI_3$ and mp-TiO_2 layer. These results suggest that in the planar PSC, unlike the mesoporous PSC, a slight change in the precursor stoichiometry strongly influences the potential distribution and the position of the diode junction.[22] More recently, Li and co-workers[24f] demonstrated realization of a FTO/c-TiO_2/n-type perovskite/p-type perovskite/spiro-MeOTAD/Au device by controlling the stoichiometry of perovskite precursors. The homojunction interface of p-type perovskite/n-type perovskite leads to a built-in electric field promoting oriented transport of photoexcited carriers with minimum carrier recombination losses. As a proof of concept, fabricated PSCs with p-type/n-type $MAPbI_3$ perovskite homojunction structure generated a certified PCE of 20.5%.[24f]

From the studies above, KPFM has been demonstrated to provide vital information of the electronic processes taking place at the "buried interfaces" formed between perovskite and selective contacts. The time evolution of microscopic pictures of physico-chemical dynamics at the interface will have help design new device structures and strategies that can further enhance Voc in PSCs. Next, we discuss how the studies at the atomic-level in perovskite materials can help elucidate dynamical processes discussed at the device level such as ferroelectricity[26] and halide segregation.[27]

2.3. Dynamical processes at the atomic level

Perovskites are considered to possess a "soft" (or "plastic") crystalline structure[28] formed by ions exhibiting rich dynamical processes such as organic cation rotations (**Figure 1c**)[26, 29], which leads to temporal-dependent deformation in the inorganic lattice.[29a, 29b, 30] For instance, the deformation and dynamics of a metal-halide lattice is associated with several local and eventually averaged global effects such as (i) dynamic direct-to-indirect transitions in bandgap suppressing charge recombination; (ii) spatially separated localization of valence and conduction bands; and (iii) nanoscale ferroelectric domains (due to the MA^+ cation dipole moment) can assist separation of electrons and holes reducing their recombination. Chiu and co-workers[26] mapped the dynamics of the MA^+ dipole orientation pattern in $MAPbBr_3$ single crystals with atomic resolution upon light illumination employing photoexcited cross-sectional STM and STS. The initial surface structure of a dimmer pattern (or checkerboard-like pattern) in dark (**Figure 2a**) transitions to a much more complex structure with a characteristic one-dimensional valley and hill pattern along the [1-10] direction under light illumination (laser diode, 532 nm, 140 mW/cm^2) (**Figure 2b**). This drastic modification of the potential energy landscape affects significantly charge carrier transport. In dark, the non-uniform pattern of the potential energy fluctuations and the lack of orientational confinement create many crossing points of hole and electron pathways. Hence, the probability of recombination increases (**Figure 2a**). However, under illumination the reordering of the MA^+ dipoles creates deep one-dimensional potential energy wells with an average depth of ~150 meV. These aligned potential well "highways"[31] help charge transport and extraction toward the electrodes (**Figure 2b**).[32] Because these organic cations exhibit polarization phenomena, the topics / questions are relevant:[33] (i) whether ferroelectric domains walls (i.e., ferroelectricity) indeed exists in halide perovskites and if so, (ii) how do they influence the overall performance in PSCs? Ferroelectric domains were proposed to provide local internal electric fields that assist charge carrier separation and hence reduce recombination on the positive side but contribute to I-V hysteresis on the negative side. Piezo force microscopy (PFM) has been widely employed to image polarization domains and local dipole moment switching in perovskites. Currently there are still debates regarding ferroelectric properties of $MAPbI_3$[11, 34] as shown by the conflicting proposals: some groups reported the existence of ferroelectricity[33, 35] while others reported the absence of ferroelectricity.[36] As pointed out previously,[11, 33, 35b, 36c] several factors can contribute to phase contrast in PFM such as (i) ion migration, (ii) local charge accumulation (i.e., electrostatic effects), (iii) electrochemical phenomena inducing local changes in the dielectric constant. All of these factors are expected to be present in perovskites, hence it is important to differentiate the various microscopic mechanisms that contribute to the apparent piezoresponse in order to confirm its intrinsic piezoelectricity. It has also been pointed out that the identification and distinction of ferroelectricity from piezoelectricity and ferroelasticity need be considered.[36a, 37] Ferroelasticity corresponds to the mechanical equivalent of ferroelectricity.[33, 38] A ferroelastic material is a solid that exhibits a spontaneous strain in its interior. This ferroelastic switching induced by a high mechanical stress can mediate the formation of twin domains of alternating crystal phases or orientations. However, purely ferroelastic domains are mechanical in nature and do not possess electrical dipoles, hence are not influenced by external electric fields.[33] The twin domains in $MAPbI_3$ were assigned to the internal stress induced by the cubic-to-tetragonal phase transition stabilized during sample annealing. The studies above show that ferroelectric switching in perovskites is yet to be unambiguously established. Furthermore, exploration of light exposure effects on surface polarization phenomena will be technologically relevant. New strategies of strain engineering warrants further investigation and may aid designing high performing and stable PSCs.[33]

Local heterogeneities in the structure, chemical composition, and phase[39] in the perovskite layer were identified to trigger the local physico-chemical dynamics upon a stimulus leading to changes as a function of time from their starting original material. Halide segregation is an example of these local changes eventually leading to degradation in mixed-cation and mixed-halide perovskites.[40] Ginsberg and co-workers[41] performed combined cathodoluminescence (CL) mapping coupled with a scanning electron microscopy (SEM) to visualize the spatial segregation into iodide- and bromide-rich domains. After 5 min illumination at 100 mW/cm^2, small clusters enriched in iodide were observed to localize near grain boundaries. The experimental results were compared with molecular dynamics (MD) simulations explaining the fundamental processes: photoinduced phase separation arises when charged excitations generate enough lattice strain to destabilize the solid solutions, favoring phase-segregation. Their proposed model for the simulations indicates that naturally occurring small variations in perovskite compositions after sample preparation is a main factor causing phase-segregation upon light irradiation. Recently, Qi, Yan and co-workers[27] revealed the exact locations of I and Cl anions in real-space with atomic resolution on the surfaces of the $MAPbBr_{3-y}I_y$ and $MAPbBr_{3-z}Cl_z$ mixed halide perovskites by STM. The surface reconstruction of a pristine $MAPbBr_3$ surface has been previously described to show the characteristic dimmer and zig-zag structures, with preference of the dimmer structure (Figure 2c).[26, 42] The incorporation of I and Cl leads to an additional randomly distribution of bright and dark protrusions (Figure 2d,e). STM measurements probe local properties of a surface. To check the local inhomogeneity, statistic data are acquired by scanning multiple areas on the same sample surface as well as multiple samples of the same type. In Figure 2,[27] STM measurements were performed on different regions of the sample surface, and the statistical data of the STM height were provided to show that the observed local atomic structure is indeed representative for the whole sample surface. These findings are supported by the fast Fourier transform (FFT) analyses of the STM images (insets in Figure 2c-e), which do not show any additional peak at low *k*-values for the mixed-halide perovskites compared to pristine $MAPbBr_3$. On the basis of density functional theory (DFT) calculations, the single bright or dark protrusion was assigned to the substitution of Br with I or Cl, respectively. The energy barrier for the formation of two isolated Cl−Br pairs is lower than the energy formation of a single Cl−Cl pair ($E_{2(Cl-Br)} < E_{Cl-Cl}$). These results suggest that at a low coverage Cl prefers to form isolated Cl−Br pairs rather than clustering together to form Cl−Cl pairs or phase segregating. The same trend was found for the iodine case, i.e., $E_{2(I-Br)} < E_{I-I}$. This was proposed as the reason why the substitution of halide ions was mainly found to be randomly distributed at the surface of the perovskite, leading to the disordered surface structure. Furthermore, several other reports[43] corroborate variations not only in halide distribution, but also in cation distribution. Because PSCs are typically tested under AM1.5 conditions (100 mW cm^{-2}), it is necessary to develop strategies to keep perovskite systems resilient against phase segregation.[44] Perovskite materials are inherently hygroscopic, hence it is necessary to protect them against ambient air exposure for prolonged lifetime. On the other hand, controlled small amounts of O_2 and/or H_2O were shown to be beneficial for enhancing PL. For example, the impact of atmosphere (O_2, H_2O, N_2) on the local luminescence of individual perovskite grains was studied by Stranks and co-workers[45] The response of each grain to continuous light illumination and atmospheric environment was systematically studied (Figure 3). PL mapping in N_2 shows the grain-to-grain heterogeneity with bright and dark grains. When moisture is introduced in the form of N_2 + H_2O (~45% RH), PL maps reveal that both the bright and dark grains show a gradual rise in PL intensity (Figure 3a). It is noticed that the PL baseline (i.e., before any light illumination, $t = 0$) of the dark grain, which likely has a higher defect density than the bright grain, increases to double. The same experiments but performed in dry air (Figure 3b) reveal that the bright grain exhibits stable PL over time, while the dark grain shows significant PL enhancement under illumination and eventually reaches the same intensity as the bright grain. When PL mapping is measured under air + H_2O (~45% RH), an initial baseline increase ($t = 0$) in the emission intensity for both bright and dark grains is observed. Then the emission from both bright and dark grains slowly rises over time under illumination with a greater relative increase for the dark grain than the bright grain. Summarizing above findings, dark grains show substantial enhancements under illumination in the presence of O_2 and/or H_2O molecules, while bright grains show less of this effect. On the basis of DFT, oxygen in the presence of photoexcited carriers was proposed to bind strongly to iodide vacancies. As a consequence, this removes electronic trap states within the band gap, leading to an increase in PL intensity over time. Because exposure to O_2 and H_2O can lead to eventual degradation of perovskite films considering long-term exposure, it is necessary to search for alternative molecules with passivating effects (extended discussion in Section 4).

In this section, recent studies show that understanding of fundamental dynamical processes at the micro/nanoscale and at the atomic scale probed by microscopy techniques helps make connections between the structural properties and the overall performance and stability of PSCs. Simultaneous mapping of spatially- and time-resolved dynamics of perovskite materials will likely impact further the design of next-generation highly efficient and stable PSCs. Above-mentioned STM/STS is also a strong technique to probe both the valance band (VB) and conduction band (CB) at the same time. Band-edges, band-alignment and band-diagram of heterojunction solar cells can be probed by STM/STS. Pal and coworkers systematically studied the band diagram and the type of conductivity of $MAPbI_3$ with different MAI/PbI_2 ratio by STS.[46] Pal and coworkers further studied the $Cu_2O/MAPbI_3$/PCBM interface and obtained a band diagram by STS.[47] The band diagram helps check whether the interface is energetically favorable for charge separation. Further studies on the band diagram that probed ensemble averaged properties and their influence on solar cell parameters are discussed in the next section (**Section 3**).

3. Ensemble averaged properties influencing solar cell parameters

In addition to microscopy-based techniques, perovskite layers as well as their adjacent functional layers are often characterized by techniques that provide ensemble averaged bulk and/or surface properties such as XRD, UV-visible (UV-vis) spectroscopy, time-resolved PL (TRPL), time-of-flight secondary ion mass spectrometry (TOF-SIMS), x-ray fluorescence (XRF), x-ray photoelectron spectroscopy (XPS), ultraviolet photoemission spectroscopy (UPS), and inverse photoemission spectroscopy (IPES). These ensemble averaging techniques have the typical probing spot size in the micrometer to millimeter range, which are close to device sizes (solar cell active areas have sizes in the millimeter scale or even larger). Hence, the extracted averaged properties from the techniques above can provide a direct relationship with the solar cell device performance such as J-V profiles and quantum efficiency measurements. For instance, the characterization of valence and conduction band features of functional layers and their energy levels, such as Fermi level (E_F), vacuum level (E_{Vac}), WF, ionization energy (IE) or electron affinity (EA), are of paramount importance for explaining the device working principles, such as charge carrier injection properties at the interface of two adjacent functional layers and charge transport properties across the layer.[48]

In this section, we discuss determination of the energy levels in perovskites by surface science techniques of UPS and IPES. Emphasis is given to how (i) the presence of high density of defects, (ii) and how the underneath substrate influence the determination of energy levels (**Section 3.1**). We then discuss unintentional variations in the perovskite film compositions and their influence on the electronic properties (**Section 3.2**), Subsequently, we discuss the energy level alignments between perovskite and its adjacent selective contacts (ETL or HTL) (**Section 3.3**).

3.1. Electronic structures of perovskites

The most direct and quantitative measurements of IE, EA, E_F positions and WF are obtained with a combination of UPS and IPES.[48-49] The working principles of UPS and IPES, and extraction of the WF, valence band maximum (VBM) and conduction band minimum (CBM) from the raw spectra as well as calculation of IE and EA can be found in a review article.[48b] We only introduce those concepts briefly that are pertinent to this section. CBM and VBM correspond to the electron and hole single-particle transport levels, respectively. Hence, the energy difference between CBM and VBM (or EA – IE) is commonly designated as transport band gap (E_G) to distinguish from the optical band gap (E_{Opt}), which is often determined by UV-vis.[48a, 49q] When IPES is not available, it is a common practice to extract EA' by subtracting E_{Opt} from IE (i.e., EA' = IE – E_{Opt}). E_G is expected to be larger than E_{Opt}, because E_{Opt} corresponds to the excitation of an exciton (the electron-hole bound pair) by photon absorption in UV-vis.[48a] In this context, it is possible to extract the exciton binding energy ($E_{Exciton}$) from the energy difference between E_{Opt} and E_G. Gratzel, Park and co-workers reported the first UPS measurements on $MAPbI_3$ deposited on TiO_2 estimating an IE of ~5.43 eV. EA' of ~3.93 eV (i.e., EA' = IE – E_{Opt}) was extrapolated based on the optical band gap (E_{Opt} ~ 1.5 eV) determined by Tauc plots of the UV-vis spectrum. The first IPES measurements in $MAPbX_3$ ($X_3 = Br_3, I_3, I_{3-x}Cl_x$) were reported by Kahn and co-workers.[49a] In the particular case of $MAPbI_3$, a smaller EA of ~3.7 eV was extracted from IPES and when compared to EA' (~3.9 eV). Because a similar IE of ~5.4 eV was extracted from UPS, E_G is larger than E_{Opt} in agreement with the model ($E_G > E_{Opt}$).[48a] Kanai, Kera, Tang and co-workers employed UPS/IPES/UV-vis to extract $E_{Exciton}$ on perovskites with varying halide compositions: $MAPbI_3$ (~180 meV), $MAPbBr_3$ (~480 meV), $MAPbCl_3$ (~120 meV), $MAPbI_{2.1}Cl_{0.9}$ (~160 meV), $MAPbI_{2.1}Cl_{0.9}$ (~40 meV), and $MAPbBr_{1.5}Cl_{1.5}$ (~140 meV).[49q] These values are in good agreement with previous reports.[49q, 50] For example, $MAPbBr_3$ has the characteristic excitonic feature in UV-vis and it shows the highest $E_{Exciton}$. The smaller $E_{Exciton}$ means that the photoinduced excitons can dissociate easily to become free carriers, which is an important figure of merit for PSCs.

Mixed cations and mixed halide perovskites (or composition engineering) are reported to show enhanced photo, thermal, and moisture stability with high PCEs compared to counterparts of pristine $MAPbI_3$ and $FAPbI_3$.[44, 51] Efforts are being made to understand the evolution of the energy levels in perovskites as a function of composition.[49c, 49q, 51] Recently, Tao, Olthof, and co-workers determined systematically the IE and EA values of 18 primary Sn- and Pb-based perovskites using UPS and IPES (**Figure 4a,b**).[49c] DFT calculations were carried out to aid the determination of the absolute positions of VBM and CBM.[49b, 52] In addition, tight-binding analysis was performed to explain the variations in energy levels of CBM and VBM as a function of the ABX_3 perovskite composition, i.e., varying X (I, Br, Cl), B (Pb, Sn), and A (Cs, FA, MA). The analysis of varying X shows that the energy of CBM is influenced by the Pb-X distance (or the confinement effect). As the Pb-X distance decreases going from I to Br to Cl, electrons on the Pb atom become more confined and their energy increases leading to up-shift of the CBM (**Figure 4c**, left panel). VBM position shifts downward going from I to Br to Cl, which is reflected by the predominant increase in electronegativity (**Figure 4c**, left panel). When varying the B cation from Pb to Sn while keeping the X halide and A cation the same, both IEs and EAs of Pb perovskites are larger than those of corresponding Sn ones (**Figure 4c**, middle panel). This was rationalized by the fact that Sn has a smaller electronegativity than Pb. When varying the A cation, both IEs and EAs do not show a uniform trend. The A site cation does not contribute directly into the chemical bonding of the B-X framework and only influences indirectly the electronic structure of B-X when changing the ABX_3 volume or introducing distortion in the structure.[53] Increasing the size of the A cation from Cs to MA to FA leads to increase in the B-X framework. This lowers the B atomic levels due to moderation in the confinement effect leading to down-shifts in VBM and CBM, but EA is affected the most because it is more sensitive to the B levels. Structural distortion (octahedral tilting and lattice deformation) reduces the hybridization between B and X states. Again, this leads to down-shifts in VBM and CBM, but VBM is more affected because it is more sensitive to hybridization (**Figure 4c**, right panel). This type of studies not only provide the fundamental understanding of the evolution of key factors that determine the absolute energy levels (IE, EA, and E_G), but also open up possibilities for rational material design for composition- and interface-engineering strategies.

As pointed out in several reports,[49b, 49c, 52] there is a challenge to reliably extract the onset of VBM or CBM from UPS and IPES, respectively, on perovskites. Kahn and co-workers pointed out that the frontier electronic states in lead halide perovskites have a low intensity on a linear scale due to the small density of states (DOS) at the VBM and CBM frontiers. Hence, these onsets could be missed with conventional fitting procedures (linear extrapolation of the lowest binding energy features in a linear intensity scale). The logarithmic plot in intensity and the fitting of DFT-calculated DOS to the experimental DOS at the band edges were proposed to determine with better accuracy the VBM and CBM onsets. In addition to the inherent difficulties of VBM and CBM onset determinations in perovskites, these energy levels depend sensitively on the (i) orientation of crystal structure, (ii) density of defects introducing additional states at the band edges, (iii) surface morphology, (iv) chemical composition variations between grains and grain boundaries, and (v) insufficient coverage leading to the underneath substrate features overlap in UPS/IPES spectra. With the aim to attain the pristine electronic structures of perovskites without the convolution of the parameters above, Koch and co-workers studied the band structure of single crystalline perovskites of $MAPbBr_3$ and $MAPbI_3$ by using angle-resolved photoemission spectra (ARPES) and low-energy electron diffraction (LEED).[52] LEED was employed to determine the surface orientation, lattice parameters, and crystal symmetry group. LEED patterns measured on $MAPbI_3$ single crystal samples at room temperature exhibited the coexistence of cubic and tetragonal structures (**Figure 5a**).[39] The determined lattice parameters are $a^T = 7.96 \pm 0.16$ Å (assigned to the (001) surface of the tetragonal phase) and $a^C = 6.02 \pm 0.11$ Å (assigned to the cubic phase). On the basis of the LEED spot intensity analysis, it has been suggested that the $MAPbI_3$ surface is predominantly composed of the cubic phase. ARPES measurements along the high symmetry directions (X—M and X—R momentum directions, **Figure 5a**) were overlaid with the DFT calculated band dispersion showing good matching (insets in **Figure 5b**). The detailed knowledge of the single crystal band structures allows reliable determination of the VBM onset. Selected cuts through the band structure between X—M and X—R shown on a linear scale (directions of the cuts are marked in the insets in **Figure 5b**), reveal large variation in the VBM with the highest VBM onset at X (~1.9 eV) and the lowest VBM onset at R (~1.4 eV). The single crystal electronic structure can be translated to the polycrystalline $MAPbI_3$ film by integrating the individual cuts for each direction of $k_{//}$ in M—X—R (**Figure 5c**). It is observed that the VBM onset is overestimated when evaluated from the extrapolation on the linear scale. However, from the semi-log plot, the VBM onset is found at 1.40 eV matching well the global VBM found from the ARPES spectrum taken at point R. The same analysis of VBM determination in semi-log plots was also applied for $MAPbI_3$ polycrystalline thin films that are expected to have random crystal orientation (**Figure 5d**). Similar to the observations obtained for the integrated ARPES spectra in single crystals (**Figure 5c**), the logarithmic scaled intensity plots for polycrystalline film (normal-emission UPS) leads to the VBM onset value close to the global VBM (**Figure 5d**). In contrast, the linear scale plots give rise to overestimated VBM onset. This study highlight the necessity to use a logarithmic intensity scale to determine the VBM onset (with a remaining fundamental uncertainty of ~50 meV, mostly underestimating the onset).[49b, 49c, 52] On a separate note, ARPES allows the evaluation of the hole effective mass (m_h*) by performing a parabolic fit of the VBM at points R and M.[49i, 52, 54] Values of 0.18 ± 0.06 m_0 at M (along X—M) and 0.50 ± 0.10 m_0 near R (along X—R). On the basis of these m_h* values, a lower-limit hole mobility values in the range of several tens of $cm^2/V{\cdot}s$ was deduced, which is another important figure of merit for PSCs.[52]

Surface defects states lead to band bending at the surfaces of perovskite polycrystalline films and single crystals.[55] However, the electronic influences of surface bend banding and how much band bending extends to the bulk (that has a much lower concentration of defect density[56]) is still not well understood. A flat-band condition is commonly assumed for the bulk in terms of energy level alignments.[49a, 57] From theoretical calculations, the energetically favorable intrinsic defects (i.e., with low formation energies such as MA or iodide vacancies) in $MAPbI_3$ films induce shallow states that are close to either CBM or VBM.[58] Based on the different defects states, perovskites could be either n-type or p-type semiconductors depending on growth conditions and substrates. Koch and co-workers reported that for $MAPbI_3$ thin films and single crystals, E_F is strongly pinned to CBM due to the surface defect states and donor agent of Pb^0.[55b] While under light illumination, VBM detected in UPS would shift up to 0.7 eV, due to filling up of the surface trap states by photoexcited electrons and reduction of the surface band bending (**Figure 6a**).[55b] They further investigated the relationship between the band structure and the density of the surface trap states (**Figure 6b**).[55a] It is shown that with a low density of trap states, the photovoltage effect could modify the surface and reduce the surface band bending. While for a high density of the surface defect states the E_F is strongly pinned to the CBM. This surface defect states also influence the energy level alignment between perovskite surface and charge transport layers. For example, ETLs like 1,4,5,8,9,11-Hexaazatriphenylenehexacarbonitrile (HATCN) and 1,3,4,5,7,8-hexafluoro-tetracyanonaphthoquinodimethane (F6TCNNQ) with large EA values coated on top of $MAPbI_3$ with different density of surface defects were investigated (**Figure 6b**).[55a] When HATCN was coated on $MAPbI_3$ with a low density of surface defect states, the band bending is reduced and flat band structure is formed with a suitable energy level alignment between $MAPbI_3$ and LUMO of ETL. While in the case of a high density of surface states, CBM of $MAPbI_3$ is strongly pinned to E_F and there is a large energy barrier for electron transfering from $MAPbI_3$ CBM to LUMO of ETL (**Figure 6b**). On the other hand, the hole blocking properties might also be reduced due to the smaller barrier between VBM of $MAPbI_3$ and HOMO of ETL (**Figure 6b**).[55a] Differences in the density of surface states are attributed as one of the reasons leading to variations in energy level alignment properties reported in several different studies even on the same material system, for example, $MAPbI_3$/C60.[49f, 49g, 57]

In a typical PSC device, the perovskite layer is sandwiched between the selective contacts or electrodes (e.g., carbon-electrode), forming a multi-layered stacked structure with several interfaces. Hence, the energy levels dictated by the intrinsic properties of the perovskite material can also be influenced when in contact with another material, which is associated with the dipole formation and band bending phenomena at interfaces.[49s, 57, 59] In this sense, the reported energy level alignment based on the vacuum level alignment may miss the effects of interfacial states, interfacial dipoles, and band bending.[11, 48b, 48c, 59b, 60] Film deposition by vacuum methods are suitable for studying the energy level alignments because the incremental deposition followed by UPS, IPES, and XPS measurements allow detailed studies of energy levels and chemical composition across the whole film thickness. A large number of works investigated the energy level diagrams at interfaces that form heterojunctions with perovskites by depositing a top layer corresponding to commonly employed HTLs or ETLs: MAPbX/spiro-MeOTAD ($X = I_3$, $I_{3-x}Cl_x$,Br_3),[49a] $MAPbIBr_2$/spiro-MeOTAD,[61] $MAPbIBr_2$/1,4,5,6,8,11-hexaazatriphenylene hexacarbonitrile (HAT-CN),[61] $MAPbI_3$/Au,[49g, 62] $MAPbIBr_2$ and $MAPbI_3$/MoO_x,[61, 63] $MAPbI_3$/copper phtalocyanine (CuPc),[64] $MAPbI_3$/pentacene,[65] $MAPbIBr_2$/N,N'-di(naphthalene-1-yl)-N,N'-diphenylbenzidine (NPB),[61] $MAPbIBr_2$/copper-hexadecafluoro-phtalocyanine (F16CuPc),[61] and $MAPbI_3$/C60.[49d, 49g, 57, 66]

There are studies that perovskite films coated on different substrates may change the position of E_F.[49s, 57, 59a, 59b, 67] Interestingly, not only the electronic properties at the interfaces are influenced by the underneath substrate, but also the bulk properties of the perovskites (typically a film with a thickness of ~200-300 nm) are also affected.[49s, 57, 59a-c] In fact, it has been hypothesized that the underneath substrates may change doping densities in perovskites and turn the perovskites from n-type to p-type or *vice versa*.[68] The nature of the substrate not only changes the energetic alignment of the perovskite layer, but also introduces gap states and influences the film formation and morphology. In a study by Kahn and co-workers using PES and IPES, for $MAPbI_3$ films deposited on NiO and TiO_2, it is demonstrated that $MAPbI_3$ films show a slightly p-type characteristic on top of NiO and better energy level alignment with the top ETL (C60). While the $MAPbI_3$ film on TiO_2 is more n-type due to the n-type properties of the bottom oxide layer.[57]

On the other hand, a few studies succeeded in growing perovskite layers by co-evaporation in vacuum or in a step-wise deposition manner for the energy level studies of perovskites when deposited on different substrates.[59a, 59d, 60] Zou and co-workers studied the substrate effect on the surface electronic structure of evaporated $MAPbI_3$ films on Al (AlO_x), Si (SiO_x), TiO_2, ZnO, ITO, Au, PEDOT:PSS, MoO_3 (**Figure 7a,b**).[59a] Similarly the WF of $MAPbI_3$ increases with the substrate WF. The shifts in VBM to lower binding energy also indicate a transition from n-type to p-type due to the substrate effect.[59a] Olthof, Meerholz and co-workers studied systematically the electronic structure changes of vacuum-deposited $MAPbI_3$ on four different substrates (PEIE, ITO, PEDOT:PSS, MoO_3; where PEIE = polyethylenimine ethoxylate and ITO = indium-doped tin oxide) by increamental deposition with film thicknesses from 3 nm up to 200 nm.[59b] In contrast with a thick solution-prepared film, the incremental thickness helps the study of interface dipole and band bending within the perovskite layer. The WF of evaporated $MAPbI_3$ depends on the substrate within the investigated thickness. But the observed interface dipoles and band bending with increasing thickness suggest that the vacuum level alignment and flat band structure is not the case in this study.[59b]

As mentioned above, the WF determination by the substrate might be valid for a perovskite film with a gap state-free interface and a low doping concentration, as systematically studied for organic semiconductors.[67, 69] Cahen and co-workers studied the WF evolution of the lead bromide based perovskites as a function of the WF for the different substrates (**Figure 7c** and **d**). For mixed cation based perovskite ($(FA_{0.85}MA_{0.1}Cs_{0.05})PbBr_3$), the free carrier concentration is determined to be low[69] and WF increases with the increase of the substrate WF (**Figure 7c**).[67] While for other Br based perovskite films (**Figure 7d**) WF did not show a positive relationship with the substrate WF,[67] which was attributed to the higher doping density and higher free carrier densities.[69]

The above studies demonstrate that the electronic structure of perovskite materials are determined by their composition, density of surface defect states, and substrate WF. Furthermore, whether the substrate WF influences the perovskite surface energy level diagram also depends on the perovskite doping density and free carrier densities. These provide hints for the device architecture design once the energy level diagrams for each material layer are determined. On the other hand, the composition is not always uniformly distributed as in the precursor solution, especially for the two-step mixed cation perovskite formation. How the unintentional variations in the chemical composition and distribution influence energy level alignment is discussed in the next section.

3.2. Unintentional variations in chemical composition

The electronic and optical properties of perovskites are sensitive to the chemical composition (**Section 2.3**). Often a scenario exists in attempting to link the microstructure and opto-electronic properties of perovskite films and devices to the initial nominal precursor ratios or chemical composition, where a correlation cannot be found. One of the origins for these large variations and difficulties in PSC reproducibility is related to the unintentional variations in chemical composition in perovskites during film processing.[70] Perovskite films can be deposited by a diversity of techniques including solution- and vapor-based methods.[71] In addition, the several precursor materials with different stoichiometries[70, 72] as well as employment of additives[73] aiming at optimization of perovskite film morphology (e.g., uniform coating, large grains), may lead to an unintentional unbalanced chemical composition of perovskites. The commonly employed post-annealing treatment after the perovskite deposition may also change the composition and thus lead to variations on the energy levels of perovskites (VBM, CBM, WF)[49d, 72d, 74] as well as to self-doping phenomenon (showing characteristic n- or p-type behavior).[74-75] XPS is a widely employed surface science technique to investigate the surface chemical composition. A few systematic studies provide insights on the large variations in IE (ranging from 5.1 eV to 6.6 eV) and EA (3.9 eV to 4.6 eV) reported in literature.[70, 72c, 72e] Meerholz, Olthof, and co-workers investigated the dependence of chemical composition (XPS) and corresponding energetics (UPS) by preparing 15 solution processed samples and 23 vapor deposited samples with various preparation conditions such as varying precursors molar ratios and annealing parameters (**Figure 8a**).[72c] As a result, $MAPbI_3$ films with diverse surface chemical composition was observed by XPS measurements. The ratio of R_{exp}, i.e. the ratio of Pb/N content, was extracted to provide the information of the contents of PbI_2 and MAI in perovskite. R_{exp} ranging from 0.4 to 1.5 was observed to correlate proportionally to IE, showing that a perovskite film with excess PbI_2 film exhibits a higher IE, while perovskites with excess MAI show smaller IE (**Figure 8a**). This similar trend can also be found by using one step solution method and varying the precursor ratios of a lead acetate trihydrate ($Pb(Ac)_2$ $3H_2O$) and MAI.[70] Furthermore, these trends in the energy levels variations are not characteristic only to $MAPbI_3$, but also to mixed halide perovskites of $MAPb(I_{1-x}Br_x)_3$ and $MAPb(I_{1-x}Cl_x)_3$.[72e] These works highlight the low tolerance of perovskite surfaces to small deviations from the nominal precursor stoichiometry. As a consequence, self-doping phenomenon (i.e., variation in the relative position of E_F with respect to the VBM or CBM) leading to n-type (E_F close to CBM) or p-type (E_F close to VBM) behavior is observed in the same perovskite material. For example, a consensus exists that stoichiometric $MAPbI_3$ (PbI_2:MAI ~ 1.0) leads to weakly n-type behavior in $MAPbI_3$ perovskites, while a high PbI_2:MAI ratio (> 1.7) leads to heavily n-type behavior. On the contrary, $MAPbI_3$ with excess of MAI (PbI_2:MAI < 0.6) leads to only weakly p-type behavior.[49d, 72d, 74] These observations were associated with the DFT calculated point defects (**Section 4**) and associated with MA^+-deficient defect.[48b, 49d, 58a, 76] The MA vacancy (V_{MA}) leads to shallow acceptor levels within the band gap. However, a close inspection of the XPS C 1s core level signal in $MAPbI_3$ shows actually two distinct peaks meaning the coexistence of at least two C-related species; see spectrum (i) in **Figure 8a**.[49m] The peak fitting analyses lead to the assignments of the high binding energy (BE ~ 286.5 eV) species to the MA in $MAPbI_3$ crystal lattice.[49m] A careful analysis of XPS atomic concentrations after normalization by the atomic sensitivity factors (ASFs) confirms that $MAPbI_3$ shows close to the ideal ratios of [Pb] : [I] : [C($CH_3NH_3^+$)] : [N] ratios of 1 : 3 : 1 : 1. In the particular example shown in **Figure 8a**, [Pb] : [I] : [C($CH_3NH_3^+$)] : [N] ~ 1 : 2.9 : 1.1 : 1.1 was reported.[49m] The origin of the C 1s peak at a lower BE of ~284.8 eV (**Figure 8a**) remains controversial at present and it has been proposed that this peak could originate from C in CH_3I,[49m, 59b, 72a, 72b, 77] CH_3NH_2,[49m, 59b, 78] adventitious carbon,[59a, 70, 72d, 73, 75b] and/or remaining solvents.[72e] The assumption of CH_3I generation due to MAI dissociation was further corroborated by mass spectrometry[58b, 79] and soft X-ray absorption and emission techniques.[77b] Park, Qi, and co-workers performed a comprehensive study of depositing MAI with different thicknesses (ranging from 1 nm up to 32 nm) by vacuum evaporation on the surface of $MAPbI_3$ perovskite (**Figure 8a**).[49m] While no changes are observed in Pb 4f, I 3d, and N 1s (no O 1s features were observed in this study) core levels, C 1s shows the appearance of additional two species as MAI content is increased. The assignments of these two species were performed on the basis of atomic ratios analyses. MAI deposition up to 4 nm leads to [C] : [N] ~ 1.5 : 1 indicating the excessive carbon from the dissociated MAI species. The nitrogen signal did not follow the carbon contents, most likely due to release of ammonia gas[58b, 79] or other nitrogen-containing gas species. Upon 32 nm MAI deposition on $MAPbI_3$, the [N] : [I] ratio decreased from ~1 : 3 (corresponding to pristine $MAPbI_3$) to approximately 1 : 2 meaning that approximated closer to optimal MAI ratio of [N] : [I] ~ 1 : 1. Similar trends of partial MAI decomposition were reported when deposited on different substrates.[59a, 59b, 59d] More importantly, the analysis of UPS showed a better alignment of VBM of $MAPbI_3$ with the highest occupied molecular orbital (HOMO) level of spiro-MeOTAD HTL when excess of MAI (4 nm) was deposited on $MAPbI_3$ (left panel in **Figure 8b**). On the basis of XPS, it has been concluded that it is not the MAI layer, but the dissociated species of MAI that lead to the interfacial energy-level tuning. The optimized interface energetics were verified with solar cell performances (right panel in **Figure 8b**), showing an enhancement of 19% in average steady-state PCE. These studies demonstrate that although UV-vis, SEM, and XRD that provides bulk-related properties show marginal changes in the perovskite film quality, the surfaces and interfaces of perovskites show large variations in chemical composition. Hence, a strong dependence of the overall PCEs with the surface and interface phenomena of stoichiometry ratios (right panel in **Figure 8b**). These studies clearly underscore the necessity of performing surface science studies in parallel to device research.

The photoemission spectra determine not only the surface electronic properties and composition, but also provide information for the bulk. Synchrotron-based techniques are strong and complementary tools for this purpose.[80] Here the usage of hard x-ray photoelectron spectroscopy (HAXPES) is discussed. XPS is mainly for surface composition information. While how the cations distribute inside the bulk is related to the bulk properties, especially for recently developed quadruple cation perovskite with Cs, Rb, MA and FA. Philippe, Saliba and co-workers applied HAXPES with different energies, thus probing different depths within the film to understand the chemical distribution of the four cations.[43g] With a higher energy of 4000 eV the probing depth could be up to 18 nm, which could be considered as the bulk composition. As reported there is a remaining PbI_2 in the double- and triple- cation perovskite. For double cation, even the unreacted FAI is present at the surface. With the increase of cation numbers, the excess PbI_2 reduced and in the quadruple cation perovskite there is no excess of PbI_2. In addition, the insertion of Cs could uniformly distribute both at the surface and in the bulk, while Rb tends to locate towards the bulk.[43g]

To conclude this part, the surface electronic properties rely on the surface composition. However, the surface composition is not always the same as in the precursor solution. Furthermore, the distribution of cations and halides is different from the surface to the bulk. Intentional addition of extra PbI_2 or MAI in the interface will be helpful to passivate the surface defect states, which reduces the non-radiative recombination and enhances the charge transport with better energy level alignment. This also highlights the importance of surface passivation, which is discussed in **Section 4**.

3.3. Energy level alignment at interfaces and the universal energy level tailoring

One important role for achieving high Voc and Jsc is the optimally aligned energy levels throughout the whole device. The energy level diagram is often adopted as a versatile tool to understand how the combination of functional layers could serve to transfer the charges and block recombination. However, this is only one of the considerations and does not completely determine the overall device efficiency. The in-gap states and built-in potential related to the interfacial defect states are also crucial for achieving high Voc.[67] Voc of a solar cell is considered as the difference between the quasi Fermi levels of perovskite under illumination.[81] Energy level matching is required in the interface between ETL/perovskite and HTL/perovskite for electrons and holes to be transferred with minimum energy losses (Voc deficit). For example, one can determine the electron/hole transfer or blocking properties from combined UPS/IPES spectra.[82] The widely employed NiOx, PEDOT:PSS, spiro-MeOTAD, poly(3-hexylthiophene-2,5-diyl) (P3HT) and poly(triaryl amine) (PTAA) are characterized as good HTLs.[49h, 83] Similarly, TiO_2, SnO_2, C60, and phenyl-C_{61}-butyric acid methyl ester (PCBM) are characterized as good ETL because the CBM of the mentioned ETL matches well with CBM of the typically used perovskite for single junction solar cells.[57, 82a, 84] Other than the CBM matching with ETL for efficient charge transfer, the hole blocking property with a deep VBM level is also required to reduce recombination. For example, C60 is a suitable layer for electron extraction from perovskite, but the small band gap leads to recombination processes. The barrier for hole blocking is small, and is considered to be the main reason for the lower Voc for inverted structure device compared with normal structure device.[57] The interfacial defect states from the ETL also influence the device performance. Qi and co-workers recently studied systematically the in-gap states of the sputtered SnO_2 induced by Ar plasma.[84a] It is shown that with minimized Ar plasma power and processing time during the sputtering deposition of SnO_2 layer, the interfacial defect states is much reduced leading to improved Voc in devices with normal structure.

Recently, Neher and co-workers studied systematically the energy level alignment of the following stacks: ITO/perovskite, PEDOT:PSS/perovskite, P3HT/perovskite, perovskite/spiro-MeOTAD, PTAA/Poly((9,9-bis[30-((N,N-dimethyl)-N-ethylammonium)-propyl]-2,7-fluorene)-alt-2,7-(9,9-di-n-octylfluorene)) dibromide (PFN)/perovskite, SnO_2/perovskite, TiO_2/perovskite, perovskite/PCBM, perovskite/C60, perovskite/LiF/C60; which are commonly used in normal and inverted structure PSCs.[81] The quasi Fermi levels determined in above mentioned stacks were observed to correlate directly with the Voc of corresponding high performance devices. For poor performing devices, the Voc is substantially lower than the quasi Fermi level, which is due to the energy level misalignment at the HTL.[81] More detailed descriptions about the energy level alignment for specific interfaces can be found from several recent review articles.[48b, 48c]

Regarding the design of interfaces favorable for charge extraction and transport, a promising approach is searching for energy-level tailoring molecules/polymers as interface modifiers and is a hot topic recently. In recent studies, the heterojunction or homojunction structure with inter band energy level alignments help further improve the charge transfer. In recent works, there are many works reporting the gradient perovskite structure, for example 2D/3D hybrid interface or homojunction formation. As we discussed above, the electronic properties of perovskites formed on different substrates are different.[57, 59b] On a n-type substrate the perovskite is more n-type and on a p-type substrate the perovskite behaves as p-type as studied by Kahn and co-workers.[57] This is especially important for optimization in p-i-n junction structured device because a p-type surface will be formed in contact with top ETL. Yan and co-workers recently reported that with a treatment of guanidinium bromide (GABr) aiming wide band gap perovskite in inverted structure device, the surface is n-type with Fermi level shifting towards vacuum level. The as prepared device showed improved Voc with a better energy level alignment.[85] In a work by Bawendi and co-workers, the formation of layered perovskite interface helps reduce voltage loss by the formation of electron blocking layer that reduce the interface recombination.[86]

Energy level alignment determines the quasi Fermi level for a perovskite film under light illumination. This section highlights the importance of the energy level alignment of perovskite materials and the design of neighboring interfaces. With better energy level alignments (i.e., less energy barrier for charge transfer), the device efficiency could be further improved with less non-radiative recombination and higher Voc.

4. Defects and interface engineering

The fundamental origin of the dynamical processes discussed in **Sections 2** and **3** are closely related to defects in perovskites.[58b] For example, ion migration can be mediated by point defects in perovskites (**Figure 9a**);[87] the type of defects such as MA^+ vacancies (acceptor) and I^- vacancies (donor) determines the p-type and n-type behavior in $MAPbI_3$ (**Figure 9b**);[58a, 76a, 88] carrier density enhancement and light-induced degradation in $MAPbI_3$ are related to defect dynamics leading to I_2 generation as discussed later in details (**Figure 9c**),[89] and so on. In semiconductor technology, the generation of electronic defects within the semiconductor band gap limit performance, lifetime, as well as reproducibility.[7b, 14f, 87d, 90]

In this section, discussion on the current understanding of the origin and nature of defects in perovskites and their impact on the dynamical processes as well as their influences on the overall solar cell performance will be discussed. The characterization of defects based solely on experimental techniques are usually inconclusive. The combination of experiment and theory is necessary to gain the understanding of the system being studied. The classification of defects in semiconductors and their electronic properties are important to be understood first (**Section 4.1** and **Table 2**). Efforts are being made to verify experimentally the theoretical predictions of trap states energy levels and trap densities. The commonly employed techniques will be discussed further (**Section 4.2** and **Table 2**). Last, approaches (interface or passivation engineering) and their passivated effects on device performance used to lower the density of defects in crystals and layers are presented and discussed (**Section 4.3** and **Table 2**).

4.1. Theories on the type of defects and experimental results

Formation of defects is unavoidable during the crystal growth and post-treatment processes due to a relatively fast crystal growth dynamics of perovskite films. Further generation of defects are also expected during the operation of PSCs. Compared with the perfect structure of perovskite, the possible different types of defects are summarized in **Figure 9d**.[91] It can be divided into two categories including point defects and dimensional defects.

4.1.1. Point defects

For the basic point defects, they are formed from intrinsic vacancy, interstitial, antisite substitution, or by extrinsic introduction of foreign atoms (**Figure 9d**). Based on the point defect theory, the two common defect pairs are Frenkel defects, i.e. simultaneous vacancy and interstitial of the same ion, and Schottky defects, i.e. vacancies of two different anions and cations.[90c] Furthermore, while DFT results have shown that Frenkel defects (e.g., Pb^{2+}, I^{-}, Br^{-}, MA^{+}) lead to both deep and shallow trap states in perovskites,[58a, 76a] Schottky pair defects (e.g., PbI_2 and $PbBr_2$ vacancies and MAI and MABr vacancies) do not generate trap states within the band gap.[90f, 90g, 92] DFT is one of the important tools that provide useful guidance to deeply understand point defects and defect pairs and to further help the design of perovskite preparation with a minimal defect density associated with high performing devices. The formation energies of different defects are calculated by first-principle calculations to evaluate the expected type of defects in perovskites.[76a, 93] $MAPbI_3$ has been the most investigated perovskite materials as it is one of the most well-known perovskite absorber, but the calculations have shown conflicting results. All possible intrinsic point defects in α-$MAPbI_3$ (pseudo-cubic high-temperature phase)[94] was first studied: three vacancies (V_{MA}, V_{Pb}, V_I), three interstitial (MA_i, Pb_i, I_i), two cation substitutions (MA_{Pb}, Pb_{MA}), and four anti-site substitutions (MA_I, Pb_I, I_{MA}, I_{Pb}) using the generalized gradient approximation without spin-orbit coupling (SOC).[58a] It was found that defects of V_{MA}, V_{Pb} V_I, MA_i, I_i, MA_{Pb} Pb_{MA}, MA_I have low formation energies leading only to shallow energy levels. Defects of Pb_i, Pb_I, I_{MA}, I_{Pb} have relatively high formation energies with deep energy levels (**Figure 10a**). It was suggested that $MAPbI_3$ is an ionic material showing very weak covalence, which is the key for the absence of deep-level defects, contributing to the good defect tolerance properties.[76a] On the contrary, DFT calculations by Sun, Zhang, and co-workers identified a strong covalency of both the Pb cations and I anions in β-$MAPbI_3$ (tetragonal room-temperature phase),[94] leading to formation of Pb dimers and I trimmers (**Figure 10b**).[95] The consequence of the strong covalency in $MAPbI_3$ is that it leads to deep charge-state energy levels (**Figure 10c**). For example, when iodine vacancy (V_I) is generated, which leads to only a shallow-level state within the band gap, actually the structure undergoes a significant distortion (because the V_I defect becomes negatively charged). Furthermore, upon capture of an extra electron, the two Pb atoms that are originally separated move towards each other and form a dimer (**Figure 10b**).[95] On the basis of band structure calculations, the formation of the Pb dimer leads to a deep defect level within the band gap (**Figure 10c**).[95] For the I_{MA} case, it has been proposed that the deep level state (**Figure 10a**) arises from the formation of an I trimmer in the neutral state (**Figure 10a,b**).[95] This work highlights the importance of the dynamical processes taking place after a I-related defect is generated in $MAPbI_3$. Qi and co-workers proposed that the generation of I_2 would lead further to subsequent degradation in a cascade effect highlighting the importance of iodine management.[79a, 96] Recently, it was shown that I_2 generation is mediated by I_i^+/I_i^- defect pair (**Figure 9c**).[89] Du studied also the defects in β-$MAPbI_3$ by partially correcting the self-interaction error and including the SOC.[94] It was shown that only the I_i[94] and its complexes (such as I_{MA}) induce deep levels inside the band gap, acting as nonradiative recombination centers.[97] γ-$MAPbI_3$ (orthorhombic low-temperature phase) was also studied with SOC to show that Frenkel defects V_{Pb}, V_I, and V_{MA} are shallow-level defects and the Schottky defects do not generate trap states within the band gap.[92] Besides $MAPbI_3$, intrinsic defects of Pb-free halide perovskites such as $CsSnI_3$[98] $CsGeI_3$[99] halide double perovskites such as $Cs_2AgInBr_6$[100] $Cs_2AgBiBr_6$[101] have also been systematically examined theoretically.

Most of theoritcal studies show that the deep-level point defects of $MAPbI_3$ are related to iodine. It should be paid more attention to this type of defects as point defects of perovskite especially the deep level defects severely limit the performance of the solar cell due to the nonradiative recombination losses caused by the defects. Having a good understanding of deep-level defects can help us to develop suitable strategies to passivate these defects to achieve higher efficiencies of PSCs.

For dimensional defects, they are formed by combining the point defects with defect pairs including one-dimensional defects, i.e. edge dislocation in plain; two-dimensional defects, i.e. the grain boundaries produced by differently oriented crystallites in contact; and three-dimensional defects, i.e. volumetric defects produced by precipitation, voids and second-phase domains (**Figure 9d**).[90c] In addition to perovskite bulk properties, characterization of surfaces and interfaces is equally important as they influence significantly on the performance of PSCs. In the following subsections, the dimensional defects are separated into atomic structures and defects of surfaces (i.e., the interface between perovskite atomic structure and a vacuum slab) (**Section 4.1.2**), heterojunction interfaces (i.e., the boundary between perovskite and a dissimilar material, e.g., ETL and HTL; **Section 4.1.3**), and grain boundary (i.e., the interface between two adjacent perovskite atomic structured layers; **Section 4.1.4**) to be discussed.

4.1.2. Surface defects

In DFT calculations, the 3D periodic boundary condition is a requisite. The perovskite surfaces are often modelled as a supercell slab with atomic structured layers and a vacuum layer.

Evaluation of the number of atomic layers and the top vacuum layer thickness is important to ensure that the total DFT energy (e.g., surface formation energy) is not influenced by the modelling parameters.[90h] The atomic structure of surfaces of $MAPbI_3$,[56, 102] $MAPbBr_3$,[103] and $CsPbBr_3$[104] perovskites were described on the basis of DFT calculations. Various thermodynamically stable $MAPbI_3$ surfaces along the different crystallographic directions such as (110), (100), (101), and (001) were characterized.[56, 102] Corroborated by STM studies (**Section 2.4**),[11, 26-27, 38, 42a-d] DFT calculations revealed that the (001) $MAPbI_3$ surface was the most thermodynamically stable, hence it has been extensively modelled. Two different terminations for the (001) $MAPbI_3$ surface found to be stable at room temperature were proposed: PbI_2- and the MAI-terminated surface (**Figure 11a**).[56, 102] The perovskite surfaces were characterized to have some similarities in electronic properties compared to their bulk counterparts. For example, these surfaces do not show the presence of neither deep surface states nor shallow surface states; the valence and conduction bands are characterized by the I-5p and Pb-6p orbitals. However, in comparison to their bulk structure, the surface of $MAPbI_3$ shows a larger band gap (**Figure 11b**). Experimentally, monolayers of ultrahigh vacuum deposited $MAPbI_3$ films and scanned by STM revealed the presence of only MAI-terminated surfaces.[11, 26-27, 38, 42a-d] Similarly, vacuum cleaved $MAPbBr_3$ single crystals also revealed the presence of only MABr-terminated surfaces.[42a] A question prevails on the non-observation of PbI_2- or $PbBr_2$-terminated surfaces experimentally under ultrahigh vacuum (UHV), which is under investigation.[42a] Nevertheless, it is pointed out that the preparation conditions of perovskite polycrystalline films lead to a myriad of surface terminations in addition to the introduction of several defects as probed by several techniques of XPS (i.e., non-stoichiometric perovskite surface composition) and PL (i.e., carrier recombination events).[19a, 72c, 105] The several types of intrinsic point defects such as vacancies (V_I, V_{MA}, V_{Pb}), interstitials (I_i, Pb_i), and anti-sites (Pb_I, Pb_{MA}) were simulated on the different $MAPbI_3$ terminated surfaces (**Figure 11b**).[102c] The defect energy levels within the band gap and defect formation energy resulted from surface point defects were analyzed. On the MAI-terminated surface, MA vacancies (V_{MA}) can be easily formed due to low formation energy (i.e., high volatility of MA^+). However, V_{MA} does not lead to the deep defect state meaning that very few carrier traps form on the MAI-terminated surface regardless of sample preparation conditions. When the perovskite film is prepared under I-rich conditions, excess of I in the form of iodine interstitials (I_i) can be introduced. This I_i on both MAI- and PbI_2-terminated surfaces has a remarkably low formation energy (–0.03 eV) and leads to deep carrier-trapping states. Recently, Meggiolaro, Mosconi, and De Angelis proposed an alternative model of the dynamics of I_i^-/V_I^+ Frenkel pair defect formation (charge neutrality is obeyed) at the surfaces of $MAPbI_3$ (**Figure 11c**).[56] The formation of an interstitial iodine (I_i^-) is followed by the formation of iodine vacancy (V_I^+) upon stimulus (e.g., photo, thermal, etc.), that could take place in the bulk or at different terminated surfaces (**Figure 11c**). However, formation of the I_i^-/V_I^+ Frenkel pair defect is favorable at the surface than in bulk because of the steric hindrance required to accommodate the extra iodine in the bulk lattice. Despite the fairly high density of defects determined experimentally (**Table 2**) in the order of 10^{16} to 10^{18} cm^{-3}, only the less abundant I_i defects were shown to introduce deep electron/hole traps in $MAPbI_3$.[106]

The above discussions highlight the negative impact of excessive iodine on the performance of PSCs and the importance of iodine management or surface passivation for enhancing PCE (**Table 2**).[79a, 89, 96, 102c, 106]

4.1.3. Interfacial defects

When two materials with different structural symmetries are contacted together forming an heterojunction interface, the physico-chemical interactions may lead to complex structural faults, distortions, and stoichiometrically deficient interfaces.[107] The electronic structures of the heterojunction interfaces formed with perovskites were described by UPS and XPS techniques. However, the atomic structure of the heterojunction interface such as the type of coordination formed was mainly described by computational simulations due to lack of experimental tools to probe the buried interfaces. In this sub-section we focus on the theoretical description of defects at the two interfaces of perovskite/ETL and perovskite/HTL systems.

The atomic structure of perovskite/ETL interfaces such as $MAPbI_3/TiO_2$,[87a, 108] $MASn_xPb_{1-x}I_3/TiO_2$,[109] $MAPbI_3/ZnO$,[110] $MAPbI_3$/C60[102e], $MAPbI_3$/PCBM,[102f] α-$FAPbI_3/TiO_2$,[111] $CsPbBr_3/TiO_2$[112] were described using first-principle calculations. In particular, the interfacial atomic structure and the electronic properties of the interface between TiO_2 and $MAPbI_3$ were extensively studied, which is discussed next.[87a, 102e, 102f, 108] On the planar TiO_2, they found that $MAPbI_3$ and $MAPbI_{3-x}Cl_x$ perovskite grows preferentially with (110)-oriented film than (001) orientation.[108a] The TiO_2 with the (110)-oriented perovskite has a stronger interaction, leading to a stronger interfacial coupling and to TiO_2 conduction band energy upshift. On the meso-structured TiO_2 (MS-TiO_2), by combining several spectroscopic techniques it was also demonstrated that the perovskite close to the MS-TiO_2 surface was locally ordered, which was induced by interfacial interactions. The locally ordered layer enhances generation of free charge carriers and efficient charge carrier transport to the contact.[108d] Transfer of the photoexcited electrons in $MAPbI_3$/planar TiO_2 is more difficult compared to $MAPbI_3$/MS-TiO_2.[108f] This may account for the reason why PSCs based on the MS-TiO_2 usually show better performance than those based on the planar TiO_2. It seems that no deep defect states were found at the $MAPbI_3/TiO_2$ interface, which is consistent with experimental observations that the $MAPbI_3/TiO_2$ interface is more electrically active than the $MAPbI_3$/HTL interface.[113] The residual PbI_2 at grain boundaries of $MAPbI_3$ was shown to have a detrimental impact on the performance of PSCs.[114] However, PbI_2 at the interface of $MAPbI_3/TiO_2$ can enhance the interfacial electronic coupling.[108c] The calculated results are also consistent with the experimental results.[115] A few studies describe the atomic structures at perovskite/HTL interfaces based on DFT calculations.[102a, 102b] By examining the various types of PbI_x polyhedron terminations, a PbI_x vacant-type terminated surface is not beneficial to the hole transfer to the HTL. PbI_2-rich terminated surface enables the photogenerated holes to transfer to HTL smoothly. This is in agreement with another reported calculation, which shows that nonpolar $MAPbI_3$ (001) and (110) surface tends to favor hole injection to Spiro-OMeTAD.[102f] While, for PCBM, it is the polar $MAPbI_3$ (100) surface that tends to facilitate electron transfer to PCBM due to largely delocalized surface states and orbital coupling.[102f]

DFT calculations show that heterojunction interfaces can lead to defect states within the band gap, impacting significantly not only solar cell efficiency, but also stability and hysteresis. The passivation of the interface between the perovskite layer and HTL / ETL are vital to the further improvement of the solar cell performance.

4.1.4. Grain boundary

In regard to dimensional defects, grain boundaries are a central discussion in perovskite research. The formation of grain boundaries is inevitable as perovskite films for PSCs are fabricated with multicrystalline nature. It is well-know that grain boundaries play a vital role in conventional inorganic photovoltaic polycrystalline absorbers (GaAs, CIGS, CZTS, and CdTe). Grain boundaries produce deep trap states within the bandgap, which in turn increase carrier recombination rate and reduce Voc significantly.[116] The coincidence site lattice (CSL) model is a mathematical tool often employed to characterize grain boundaries in computational studies.[117] This model provides the idea that grain boundaries are not formed randomly based on the principle of energy minimization of the system upon its formation. Briefly, a grain boundary is modeled as two adjacent grains connected forming an interface (**Figure 12**).[117d]

This interface or grain boundary can be generated by (i) the two aligned adjacent lattices of grains (or Ruddlesden-Popper faults), (ii) twisting a grain with the axis of rotation corresponding to the normal plane, (iii) tilting a grain with the axis of rotation perpendicular to the normal plane, or by a combination of all the geometrical operations above (**Figure 12**).[117d] The atomistic models of grain boundaries will exhibit a variety of interfacial structures. Because of the periodicity in the crystal structure, the geometrical operations above (**Figure 12**) may also generate atomic arrangements at the interface with certain periodical features (suitable for DFT calculations). The grain boundaries that have a certain number of atoms sharing the same lattice in both of two adjacent grains (or CSL) are of particular interest in many computational studies due to their periodicity (i.e., a more realistic non-periodic atomic structures require large computational efforts). These special type of grain boundaries are distinguished by the reciprocal of Σ = (number of coincidence sites in the unit cell) / (number of all lattice sites in the unit cell) value and specifying the combination of the grain boundary planes (**Figure 12a**).[117] For easy visualization, some of the crystallographic planes for β-$MAPbI_3$ are provided in ref. [118]. A large reciprocal value of Σ means the periodicity is long-ranged (characterized as random boundary). This random boundary possesses a high interfacial energy because the atomic arrangement differs significantly from its original bulk structure.[117b] On the contrary, low Σ values have short-range periodicity (i.e., larger number of atomic coordination at the boundary interface between two adjacent grains), thus leads to lower interfacial energy than random boundaries. Yan and co-workers provided the first DFT calculations of [100](111)Σ3, which corresponds to a twin grain boundary with two (111) planes of $MAPbI_3$ oriented along [100] direction (**Figure 12a**; i.e., the simplest boundary when the crystals on each side of a plane correspond to mirror images of each other. There is no region of disorder and the boundary between the twinned crystals will be a single plane of periodic atoms. DFT calculations showed that [100](111)Σ3 structured grain boundaries are electronically benign, i.e. they do not introduce deep trap states.[76] The other type of [100](310)Σ5, which also shows symmetric and periodic atomic structured grain boundary (supercell depicted in **Figure 12b**) was considered based on the fact that atomic structure in this type of grain boundary was previously observed in $SrTiO_3$ perovskite by high resolution transmission electron microscopy (HR-TEM).[119] MD simulations were performed on the [100](310)Σ5 grain boundary (**Figure 12b**) at 300 K to implement the temporal evolution of structural disorder and imperfections due to thermal fluctuations. MD simulations were unable to show generation of deep defects states within the band gap.[76, 119a] The grain boundary sites in [100](310)Σ5 were found to increase the hole effective mass leading to only shallow trap state near VBM.[76b]

Experimental mapping of grain boundaries in organic lead halide-based perovskites is challenging because of their inherent sensitivity to vacuum and when exposed to excitation probes (e.g., electron beam, X-ray, light, etc.).[79a] In contrast, inorganic perovskites (e.g., $CsPbBr_3$) have a better structural stability and efforts have been made to characterize the grain boundaries by electron microscopy techniques.[8a, 120] For example, Mishra and co-workers determined the atomic structures of grain boundaries in inorganic $CsPbBr_3$ perovskite nanocrystals by scanning transmission electron microscopy-annular dark field (STEM-HAADF) imaging combined with DFT modeling (**Figure 12c**).[8a] The grain boundary planar defects of Ruddlesden-Popper (RP) and Br-terminated and Br-deficient [001](210)Σ5 were identified. Statistically, the Br-terminated [001](210)Σ5 type grain boundary was the majority (amounting to 19 out of 42 analyzed). Other type of asymmetrical grain boundaries such as [001](110)(260)Σ17 were also identified, but with a lower frequency of occurrence. The other typical planar defect analyzed is the RP planar faults, which consists of two CsBr layers stacked between two $CsPbBr_3$ domains. The RP planar faults propagate along the (010) and (100) planes forming a 90° steps at each intersection (**Figure 12c**). Further examination of the band diagram across the grain boundary reveals that neither of Br-terminated [001](210)Σ5, RP planar fault, as well as [001](110)(260)Σ17 induce deep defect levels. However, the Br-deficient [001](210)Σ5 associated with the presence of Pb dangling bonds or Pb-Pb bonds were identified to lead to deep trap levels. Calculations by Guo, Wang, and Saidi also corroborates that grain boundaries in $CsPbX_3$ (X = Cl, Br, and I) as well as $MAPbI_3$ perovskites do not generate midgap states inducing only shallow states near the VBM.[121] As comparison, grain boundaries in lead-free halide double perovskites of $Cs_2AgInCl_6$, $Cs_2AgBiCl_6$,[122] as well as kesterite of $Cu_2ZnSnSe_4$,[123] were also evaluated using DFT. The simulated [001](310)Σ5 grain boundaries of $Cs_2AgInCl_6$ and $Cs_2AgBiCl_6$ and [001](114)Σ3 grain boundaries of $Cu_2ZnSnSe_4$ with low-formation-energy can result in deep-level defect states in the bandgap and act as the carrier recombination centers deteriorating their optoelectronic properties.

According to the simulation results, to increase photon-to-electron conversion efficiencies, grain boundary passivation was suggested. To date, although there are experimental reports about the beneficial roles of grain boundaries in separating and collecting charge carriers efficiently,[10b] there is also experimental evidence showing that grain boundaries notably deteriorate the film optoelectronic properties (**Section 2**).[12d, 14e, 19a, 124] Hence, passivation of grain boundaries generally enhances the PV performance as well as decreases the hysteresis phenomenon in the J-V curves. For instance, although $MAPbI_3$ grain boundaries leads to defects close to VBM that can still acts as a shallow hole trap states, the spontaneous passivation of extrinsic elements such as Cl (in $MAPbI_{3-x}Cl_x$)[76b, 125] and O (from air exposure process)[76b] can weaken the wrong bonds at grain boundaries and thus reduce the shallow trap states.[76b] Other calculated results[125] also demonstrated that the introduction of substitutional Cl dopants at the [001](012)Σ5 grain boundary of $MAPbI_3$ is beneficial in reducing the electron-hole recombination events.[12d, 14e, 19a, 124] These studies highlight that the role of defect tolerance in grain boundaries as well as grain boundary induced deterioration of pristine perovskite optoelectronic properties as the fundamental origin.

4.2. Passivation strategies

Thanks to the theoretical and experimental tools to detect the defects, a deep understanding of the defects of perovskite is obtained. Defects especially the deep-level defects are proven to result in nonradiative recombination losses and limit the performance of the resultant PSCs.[58a] It is necessary to develop effective approaches to decreasing the defect density. Several strategies have been developed, which can successfully passivate defects including point defects and dimensional defects of surface, interfacial and grain boundary defects (summarized in **Table 2**).

4.2.1. Point defects passivation

The common route to passivate point defects is by adding dopants or additives in the perovskite precursor solutions to minimize the defect formation during the perovskite growth process. The dopants or additives of inorganic dopants such as K^+, Ni^{2+}, I_3^-, Al^{3+}, Cs^+ and Rb^+ ions[96a, 126] and organic dopants such as MA[127] and 2,3,5,6-Tetrafluoro-7,7,8,8-tetracyanoquinodimethane (F4TCNQ)[128] are successfully applied into the precursor solutions to passivate the different type of defects density in different degrees. In addition to adding dopants or additives, light has impact on the defect density. It was found that under the light irradiation, the photoluminescence quantum efficiency was enhanced.[129] Combined with theoretical investigations, they proposed that the light irradiation promotes the annihilation of V_I^+/I_i^- Frenkel pairs. Recently, a new behavior in hybrid perovskite was proposed that local distortions can be passivated under light illumination.[130] Mohite and co-workers found that a uniform lattice expansion in hybrid perovskite thin films of $FA_{0.7}MA_{0.25}Cs_{0.05}PbI_3$ occurred under continuous light illumination. After passivation by light, PCE was enhanced from 18.5 to 20.5% with improved stability. However, it was proposed that the limited stability of organometallic PSC during long solar irradiation was due to the formation of light-activated meta-stable deep-level trap states.[130-131] Long light exposure time is detrimental for the performance. They also mentioned that it can self-heal completely by resting them in dark.

The performance of PSCs enhanced after passivation of point defects in perovskite. However, compared with single crystals, perovskite grains behaving as large dimensional defects including surface defects and grain boundaries play a vital role in the influence of the PSC performance. The degradation of perovskite grains was studied to be triggered by the defective surface and grain boundaries.[132] It is desirable to passivate these dimensional defects to boost the performance. In the next subsections, passivation strategies on dimensional defects are described.

4.2.2. Surface/Interface passivation

Theoretical studies of defects (**Section 4.1**) are often divided into the surface defects (i.e., the interface between perovskite atomic structure and a vacuum slab) and interface defects (i.e., the boundary between perovskite and a dissimilar material). As the perovskite layer directly contacts HTL and ETL in PSCs, the surface/interface passivation are discussed together in this section according to the contact layer, i.e., at the perovskite/ETL interface and perovskite/HTL interface. For the surface/interface passivation, a number of passivation molecules were applied on the surfaces of perovskites as they serve as electron donors or electron acceptors, which can interact with charged defects in perovskite.

For perovskite/ETL interface passivation, a fullerene derivative material of PCBM was firstly introduced to passivate the interface of $MAPbI_3/C_{60}$ in the structure of ITO/PEDOT:PSS/$MAPbI_3$/passivation layer/C_{60}/BCP/Al by depositing it on the surface of perovskite layers.[133] The resulted PSC exhibited negligible photocurrent hysteresis and improved device performance. PCBM effectively passivated the trap defects on the surface by almost two orders of magnitude decrease in the range of energy level above 0.40 eV. Other fullerene derivative material such as ethanolamine (ETA)-functionalized fullerene C_{60}-ETA was also successfully introduced to further passivate the TiO_2:TOPD (titanium oxide bis(2,4-pentanedionate)) surface in PSC with a glass/ITO/TiO_2:TOPD/C_{60}-ETA or [6,6]-phenyl-C-61-butyric acid methyl ester (PC60BM) /$MAPbI_3$/Spiro-OMeTAD/Au architecture.[134] Besides fullerene derivative material such as π-conjugated Lewis base with n-type semiconductor property,[135] the chloride can also efficiently passivate charged defects induced by both the cationic and anionic defect sites in the structure of ITO/PTAA/$MAPbI_3$/functional layer (L-α-phosphatidylcholine, choline iodide or choline chloride)/C_{60}/BCP/Cu.[136] TiO_2, a typical and common used ETL, behaves as photocatalyst degrading perovskite. CsBr as an interfacial modifier between perovskite/ETL not only passivated trap states to improve the PCE from 11.5 to 15.3%, but also inhibited the photocatalytic active sites on the TiO_2 to enhance the stability under UV irradiation.[137] As discussed before (**Section 4.1.3 Interfacial defects**), the planar TiO_2 with the (110)-oriented perovskite has a stronger interaction, leading to a stronger interfacial coupling. However, so far the perovskite cannot be well-prepared with all the (110)-oriented perovskite. To enhance the interfacial binding in planar PSCs, the interfacial Cl atoms on the TiO_2 colloidal nanocrystals was introduced.[108] It forms stronger binding and also suppressed deep trap states at the $TiO_2/FA_{0.85}MA_{0.15}PbI_{2.55}Br_{0.45}$ perovskite interface and thus considerably reduce interfacial recombination.

Other than TiO_2, SnO_2 is also well developed for high performance PSCs specially with a planar structure. Compared with TiO_2, SnO_2 shows higher mobility and chemical stability, and the SnO_2 layer can be readily deposited by low temperature solution coating,[138] commercially available precursor solutions,[82a, 84d] atomic layer deposition (ALD),[139] sputtering deposition[84a] and chemical bath,[140] which all show performance over 20%. Qi and coworkers found that for the sputtered SnO_2, the gap states close to the valence band of SnO_2 significantly deteriorated the device performance.[84a] The passivation of the SnO_2 surface helped improve the performance with reduced hysteresis. Liu and coworkers applied ethylene diamine tetraacetic acid (EDTA) to passivate the commercially available SnO_2 nanocrystals.[141] The energy level for the EDTA passivated SnO_2 is better aligned with the conduction band of perovskite thus a higher V_{OC} and a certified 21.52% PCE were obtained. The passivation of SnO_2 with EDTA not only improves the efficiency, but also enhances the device operational stability under light illumination. Fullerene and its derivatives are also good candidates to modify SnO_2 for high performance PSCs.[142] Zhan, Meng, Tu and coworkers developed a fullerene derivative 9-(1-(6-(3,5-bis(hydroxymethyl)phenoxy)-1-hexyl)-1H-1,2,3-triazol-4-yl)-1-nonyl [60]fullerenoacetate (C9), and anchored C9 to the surface of SnO_2 ETL.[143] The anchored C9 could efficiently passivate the oxygen-vacancy-related defects on the surface of the SnO_2 and suppresses charge recombination. The reduced injection barrier also enhanced charge extraction. Li and coworkers introduced NH_4Cl into commercial SnO_2 precursors and found that NH_4Cl induced the coagulation of SnO_2 colloid and enhanced electron mobility with a better energy level alignment.[144] The introduced NH_4^+ and Cl^- could suppress the formation of deep-level defects thus optimize the SnO_2/perovskite interface and reduce charge recombination.

Regarding the studies on perovskite/HTL interface, the organic Lewis bases of thiophene and pyridine was firstly introduced to passivate the $MAPbI_{3-x}Cl_x$/Spiro-OMeTAD interface, inducing less defect density and enhanced performance.[19b] Snaith and co-workers proposed that the Lewis bases could passivate under-coordinated Pb ions in the perovskite crystal via the coordinate bonding between the sulfur atom in thiophene or nitrogen atom in pyridine with under-coordinated Pb ions in the perovskite. Other organic passivation materials such as PCBM was also reported to passivate perovskite/spiro-OMeTAD interface through passivation of under-coordinated I atoms (I^-) at the surface.[145] Besides organic passivation materials (such as poly(methyl methacrylate) (PMMA)[146]), ionic material such as MABr was also used to passivate the perovskite/Spiro-OMeTAD interface.[147] Mhaisalkar, Mathews and co-workers proposed the ions (MA^+ and Br^- ions) can diffuse into the vacancies created by the loss of organic cations and I^-, thus passivate the defects. The modification of the perovskite layer with an ultra-thin inorganic layer like Al_2O_3 could also enhance the perovskite stability against humidity.[148] Koushik and coworkers introduced an ultra-thin Al_2O_3 layer by ALD which could effectively protect the perovskite layer against humidity. In the meantime, charges could also transfer efficiently and the performance was improved with an optimized Al_2O_3 thickness. Although 3D perovskite materials have stronger light absorption and good charge carrier transport properties than 2D perovskites, their moisture stability is inferior to 2D perovskites considering the hydrophobic feature of the large organic cations in 2D perovskite segment. To combine their advantages, a 2D layered PEA_2PbI_4 perovskite layer was in situ grown on the surface of 3D perovskite film to improve the stability of PSCs.[149] In addition, the thin 2D layers also have defect passivation effect to enhance the performance.[150] Paetzold and coworkers recently created a hybrid 2D/3D perovskite heterostructure by spin coating n-butylammonium bromide on a wide band-gap perovskite absorber layer.[151] This thin 2D perovskite layer efficiently mitigated non-radiative recombination and exhibits a record Voc of 1.31 eV for a wide band gap (1.72 eV) PSCs with a standard structure. Recently, the performance of normal structured PSCs passivated by the organic halide salt phenyl ethyl-ammonium iodide (PEAI) was shown to be superior than that of passivated by the 2D layered

PEA_2PbI_4 perovskite at the interface of $FA_{1-x}MA_xPbI_3$/spiro-OMeTAD.[84d] The highest certified efficiency of 23.32% has been achieved by employing PEAI to suppress the surface defects of perovskite. As in the inverted structure PSCs, the bottom hole transport layer will influence the growth of the perovskite layer and its quality. The above-mentioned post growth process also works for inverted structured PSCs. Zhu, Snaith and coworkers developed a solution-processed secondary growth technique to enhance Voc of inverted planar structured PSCs.[49o] To improve the wettability of the perovskite solution on the bottom HTL PTAA, a pre-treatment with dimethylformamide (DMF) was applied. With a high-quality perovskite layer, the solution-processed secondary growth on top of perovskite helped produce a wider bandgap top layer and also mitigated non-radiative recombination, thus a high Voc of 1.21 eV was obtained for perovskite with a band gap of 1.62 eV.

As the passivation of perovskite/ETL and perovskite/HTL are beneficial to reduce defects at the surfaces, it is easy to consider to minimize defects at both interfaces. For example, the passivated PSCs inserting an ultrathin PMMA films at both the perovskite/Spiro-OMeTAD and perovskite/TiO_2 interfaces boosted the Voc from 1.17 eV (passivated PSCs only at perovskite/TiO_2 interface) to 1.21 V.[152] PbI_2 was also applied as passivation layer and a double-side-passivated PSCs by distributing PbI_2 to both front/rear-side surfaces yielded PCE of 22.3%, which was better than the device with only passivation in the perovskite/Spiro-OMeTAD interface of PCE 21.6% and without passivation of 18.8%.[115] The performance of PSCs was further enhanced after both side interface passivation compared to only one side interface passivation. Therefore, passivation of both interfaces (ETL/perovskite and perovskite/HTL) to further reduce defects is key to further improving the optoelectronic properties of PSCs.

4.2.3. Grain boundary passivation

In the former section (**Section 4.1.4)**, we introduced and analyzed the theories of defects on the different types of grain boundaries. However, in real PSCs, it is difficult to control grain boundary structure and chemical composition during formation of perovskite films due to generally fast growth process and a large number of formed grains. Furthermore, it is also difficult to assign whether the passivation contributes to the interface passivation or grain boundary passivation. For instance, the passivation effect of chloride on perovskite surface treatment was comparable to those with blending the chemicals in the precursor solution, i.e. the post surface treatment of perovskite may be enough to passivate the grain boundaries in bulk.[136] Considering these cases, we discuss grain boundary passivation according to two common methods: 1) post-treatment of passivation molecules on the perovskite films with large grain sizes and 2) one-step passivation treatment of grain boundaries with additives in the precursor solution.

The first approach is to decrease defects by reducing the area of grain boundaries with larger grain size. Many efforts have been investigated to obtain large grain size by varying the preparation method such as thermal annealing,[153] solvent annealing with N,N-dimethylformamide [154] or dimethyl sulfoxide,[155] hot-casting technique,[156] recrystallize the perovskite film[157] and tuning the precursor solution by tuning the concentration[158] or adding additives.[159] The grain size of $MAPbI_3$ crystal can be enlarged from 100-300 nm to micrometer-scale or even to millimeter-scale crystalline grains (1 to 2 mm)[156]. Larger grain size of perovskite was shown to have reduced trap density. The resultant PSCs with larger grain size exhibited an enhanced performance including enhanced Jsc and Voc. They usually inclined to ascribe the enhanced J_{sc} to the thicker active layer with improved light-harvesting property and the enhanced V_{oc} to decrease in trap density. The second approach has focused on the usage of additives mixed with the precursor perovskite solutions to passivate the defects in grain boundaries during the crystal growth. Especially, the Pb and I related defects, such as under-coordinated Pb^{2+}/I species and Pb-I antisite defects, in grain boundary will deteriorate the PSCs performance and need to be passivated. Various additives are applied to successfully passivate the defects in grain boundaries, such as D-π-A molecules,[126d] methimazole (MMI),[114] F4TCNQ,[128] guanidinium (GA),[160] ethyl 2-cyanoacrylate (E2CA),[161] 1H,1H-perfluorooctylamine (PFA)[162] and semiconducting molecules with Lewis base or acid functional groups including 7,7'-[4,4-Bis(2-ethylhexyl)-4H-silolo[3,2-b:4,5-b']dithiophene-2,6-diyl]bis[6-fluoro-4-(5'-hexyl-[2,2'-bithiophen]-5-yl)benzo[c][1,2,5]thiadiazole]) (p-DTS($FBTTh_2$)$_2$ (abbreviated as DTS), benzodithiophene (BDT) unit based DR3TBDTT (DR3T)[163] and PCBM.[164] After the introduction of these additives, different types of the Pb and I related defects were passivated and the performance of the PSCs with reduced defects improved.

These studies suggest that perovskites with lager grain sizes and less defects in grain boundaries (especially those defects related to lead and iodine) are beneficial to fabricate high-performance PSCs. Overall, passivation of intrinsic point defects, interfacial defects, and grain boundary defects have been shown to remarkably increase PCE, demonstrating the importance of these defect passivation in the cell performance. Although several passivation molecules are provided to reduce the different types of defects (**Table 2**), new types of passivation materials and techniques need be explored. The new strategies of simultaneous passivation of various types of defects present in perovskites are expected to boost the performance of PSCs closer to their theoretical limit.

5. Conclusion and outlook

In this review, our central focus was to analyze recent advances of metal halide PSCs from the perspective of surface science viewpoint. Surfaces and interfaces in perovskites play major role on the current technological challenges in PSCs such as performance, reproducibility, hysteresis, and stability. For example, efficient generation of charges, extraction, and transport with minimum recombination events through optimized interfaces is crucial to attain high efficiency. These interfaces can be in the form of (i) grain boundaries and/or sub-grain boundaries within a polycrystalline film composed of the same material,[165] (ii) heterojunction interfaces (i.e., the boundary between perovskite and a dissimilar material, e.g., ETL and HTL), (iii) surfaces (i.e., the interface between perovskite atomic structure and a vacuum slab. The initial condition of the morphology, crystal orientation, and chemical composition at interfaces in the as-prepared films are not static; i.e., interfaces are expected to show a physico-chemical dynamical process over the course of solar cell operation time. As consequence, these will sensitively affect charge carrier dynamics induced by the changes in defect density and energy level alignments at the interfaces.[11, 38, 84c]

Case studies that demonstrate the feasibility of bridging the gap between surface-science-related fundamental investigations and polycrystalline film technology applied to PSCs were discussed. The fundamental understanding of correlations between local electronic properties and morphologies to technologically relevant solar cell parameters have progressed significantly (**Section 2**). For example, AFM is a well-established SPM tool for characterizing grains, grain boundaries, and surface roughness.[11, 38, 166] The morphology of the perovskite film as well as its adjacent functional layers play a crucial role in determining the overall performance of PSCs. Larger and oriented grains often lead to enhanced carrier mobility,[167] reduced density of electronic traps (**Section 4**),[25, 90b] and enhanced stability.[132, 168] SPM with multi-modality imaging capability such as pc-AFM and KPFM provide a one-to-one correlation of photocurrent and photovoltage, respectively, to the local morphology (**Section 2.1** and **2.2**).

There now exists a broad consensus that ion migration is the main mechanism governing the macroscopic phenomena of photocurrent, photovoltage, as well as anomalous electronic behavior including hysteretic I-V[169] and switchable PV effects.[36b] As discussed in **Sections 2.1** and **2.2**, spatially-resolved mapping techniques revealed the preferential ion migration phenomena through grain boundaries in perovskite polycrystalline films. However, ion migration is not a phenomena taking place only in polycrystalline films, but it was also reported to take place in $MAPbBr_3$ single crystal (bulk transport)[12c, 170] as well as across the planes of layered 2D perovskites in the form of single crystal[171] and 2D polycrystalline films.[172] Although ion migration was demonstrated to exist in PSCs, questions on (i) what are the characteristic time scales for different perovskites? and (i) how it compares with electronic dynamics of charge generation, transport, recombination remains elusive (**Figure 1c**). Great efforts are been made in the direction to characterize the time scale of ion migration on different perovskite systems. A complete understanding of the time scale dynamics (e.g., interplay of charges and ionic species) is expected to help design solar cells with reliable and stable current-voltage responses. The number of reported works on this topic is still scarce. However, this number is increasing due to new advances in SPM techniques that allows to perform fast scanning and study the electrical property dynamics (**Table 1**). For example, a high speed KPFM (16 s per image) was first described by Leite and co-workers[90e] allowing to monitor in real-time the modifications of CPD maps in perovskite films. In the report by Jesse and co-workers,[170a] ion migration probed in a lateral device structure of Au/$MAPbBr_3$ single crystal/Au showed a complex potential transient dynamics in the μs time scale. Two processes with characteristic fast (electronic) and slow (ion migration) dynamics were probed by their fast-free force recovery (F^3R)-KPFM technique indicating that the imaged dynamics are not simply electronic in nature. Hundreds of μs was the characteristic time scale that the transient behavior in the potential mapping takes to reach equilibrium after the field across the device was applied. More recently, Ginger and co-workers[172b] studied the dynamics of ion migration in 2D layered perovskites of $(C_4H_9NH_3)_2PbI_4$ employing time-resolved G-mode KPFM and fast free time-resolved electrostatic force microscopy (FF-trEFM). Under illumination, the photovoltage also equilibrates after hundreds of µs, a time scale that was associated with ion migration and also with dynamics of trapped electronic carriers that are overlapping (**Figure 1c**). Finally, Berger and co-workers[12c] performed time-resolved KPFM measurements with sub-ms time resolution on a cross-section of complete device of FTO/SnO_2/(MA-FA)Pb(I-Br) mixed perovskite/spiro-MeOTAD/Au. A localized interfacial charging forms at the photoanode interface within 3-10 ms after applying a forward bias to the device. Subsequently, after switching off the forward bias, these interfacial charges were stable for over 500 ms creating a reverse electric field in the cell. This asymmetry in the kinetics indicates the complex physico-chemistry of ion migration and stabilization of the ionic species leading to interfacial charges.[10g, 90e] The longer stabilization of this reverse electric field is associated as cause for generating higher photocurrents observed during the reverse bias scan (in comparison to the forward bias scan) in the solar cell I-V measurements (hysteresis). In all the studies of ion migration dynamics described above, the current-voltage hysteresis in PSCs is dominated by the dynamics of the formation and release of ionic charges at the interfaces.

As highlighted in **Sections 2.3** and **4.2.3**, investigation of dynamics at the atomic level fundamental studies by STM/STS and TEM were reported to provide also unique knowledge that correlates with macroscopic observations in PSCs (**Table 1**). These include (i) perovskite surface reconstruction with characteristic dimmer structure of halides (I or Br)[27, 42] in dark that transforms to the complex structure with characteristic one-dimensional valley and hill pattern upon light illumination. (**Figure 2a,b**) The new structure shows enhanced charge transport properties[26] (associated with ferroelectric domains[31-33]); (ii) The real-space spatial distribution of I and Cl anions on the surfaces of the $MAPbBr_{3-y}I_y$ and $MAPbBr_{3-z}Cl_z$ mixed halide perovskite probed by STM[27] were found to be randomly distributed, which has implications on the halide segregation phenomena.[40-41] (iii) The atomic structure of grain boundaries in $CsPbBr_3$ perovskites measured by STEM-HAADF[8a] and DFT studies reveal the defect tolerance properties of Br-terminated interfaces of grain boundaries; Br-deficient grain boundaries were associated with the presence of Pb dangling bonds that lead to deep-trap levels. These recent studies show the relevance of atomic level studies that leads to the bridging of surface science studies to macroscopic parameters relevant to solar cell operation.

In contrast to local property investigations by microscopy techniques, ensemble averaged measurement techniques also play a pivotal role for the understanding of PSC operation principles (**Section 3**). The typical probing spot sizes of ensemble averaging techniques are in the micrometer to millimeter range, which are comparable to active area sizes in devices. Therefore, fundamental information extracted from such techniques can provide a direct relationship with solar cell parameters. For example, UPS and IPES are widely employed techniques in surface science to determine the quantities of IE, EA, E_F positions and WF on perovskite surfaces (**Section 3.1**).[48-49] XPS is often employed for the surface chemical composition determination (**Section 3.2**), while LEED determines surface crystal structure (**Figure 5a**).[39] An important consideration during the measurements regards the stability of perovskite materials under the environment (e.g., ambient air versus ultrahigh vacuum),[79a] which modification (chemical, structural, defects) of the material leads to artifacts, complicating the interpretation of the results. Therefore, careful consideration of environmental conditions as well as interactions between perovskite and the excitation probe (electron beam, UV, X-ray, and electric field) are important factors for avoiding misinterpretation of the results obtained. PSC is generally composed of stacks of anode/cathode, a perovskite layer as absorber, and selective contact layers (ETL and HTL), resulting in multi-interfaces between these layers (**Figure 13**). Energy level alignments at these interfaces are a versatile tool for evaluating the charge extraction and transport at the interfaces (extended discussion in **Section 3.3**).[48b] On the other hand, STM/STS, UPS, XPS studies are mainly performed in ultra-high vacuum (UHV), which presents a "pressure gap" between these UHV studies and perovskite solar cells that are operated in ambient pressure. How these UHV results can be related to the surface of real PSCs under ambient conditions is crucial, but is not well understood at this stage. The surface evolution under controlled environment will be an important future direction. Some of the surface properties can be studied by both UHV techniques and ambient techniques, it will be helpful to cross check the two sets of results to better understand the surface evolution between UHV and ambient. An example of such studies is that the work function of a thin film can be determined by both UPS (a UHV technique) and Kelvin probe (possible to be operated in ambient or controlled gas environment).[173] Another example is that near-ambient pressure XPS studies can provide more insights about how the surface composition and morphology changes in ambient condition or controlled condition.[174]

In situ studies and time dependent measurements monitoring the evolution of perovskite surfaces during, for example, degradation processes induced by thermal heating, upon controlled gas exposure (H_2O and O_2) and/or irradiation with photons (e.g., visible light, UV, and X-rays) are scarce.[175] Similarly, in operando measurements on PSCs with synchrotron radiation techniques was discussed as a insightful method to study photovoltaic device dynamics under a number of different stimuli such as cooling/heating, current/ voltage, light, and environmental stressing conditions.[175b, 176] An example of in operando measurements was accomplished on a $MAPbI_3$-based solar cell by designing a sample stage for simultaneous I-V curve measurements dependent on temperature and synchrotron-based X-ray diffraction.[176a] A detailed correlation between the perovskite crystal structure and I-V profiles was established on the same device sample, revealing insights into tetragonal to cubic phase transition temperature (60.5−65.4 °C).[176a] In another study,[176b] the crystallinity evolution correlated with device performance was performed with in situ GIWAXS and in operando J-V measurements. To investigate the solar cell performance evolution (in-operando), perovskite films starting from its precursor solutions were deposited on substrates with interdigitated back-contact with alternating HTLs and ETLs. These structures function as working solar cells when the precursor solution deposited across the electrodes solidifies to perovskite film (i.e, photovoltaic activity). It is found that at the first stage of conversion from the precursor solution phase, a high Voc is observed even though the bulk of the material is still present as precursors. This indicates that at the earlier stage of perovskite structure formation, the semiconductor band gap is already well-defined and free of sub-gap trap states. The Jsc continues to increase monotonically upon a solid bulk is initially formed within the film until a complete solid film is formed. This work reveals important dynamics among the different stages of perovskite film conversion and correlation to device performance. In addition, the enhanced pathways for charge diffusion during perovskite film conversion highlights the remarkable defect tolerance of perovskite materials.[176b] The case studies above show that in operando measurements provide further unique insights into the dynamics of PSCs under real operation conditions, which will lead to a new front of technological advances in PSCs.

All the dynamical processes discussed in **Sections 2** and **3** are associated with the fundamental origin of defects in perovskites (**Section 4**). The presence of electronic defects within the band gap limits the efficiency, reproducibility, and stability of PSCs:[90j] (i) point defects in perovskites assist ion migration phenomena (**Figure 9a**);[87] (ii) semiconductor behavior of p-type or n-type in $MAPbI_3$ determined by MA^+ vacancy (acceptor) and I^- vacancy (donor) type defects (**Figure 9b**);[58a, 76a, 88] (iii) light-induced degradation in $MAPbI_3$ related to V_I and I_i Frenkel pair defects dynamics (**Figure 11c**).[89] Therefore, efforts are been made in the direction to characterize experimentally the type of defects in perovskites and minimize defect density by well-controlled perovskite film fabrication technology. In fact, PSCs based on thin-sliced grain boundary free single crystals can be promising for attaining both high efficiency and enhanced stability. Mohamed, Bakr, and co-workers employed single crystal $MAPbI_3$ perovskite sample (thickness = 20 μm) showing an outstanding PCE of 21.09% and FF up to 84.3%.[4] However, technological challenges such as upscaling of perovskite single crystals prevail currently and fabrication of polycrystalline films may be a viable route for upscaling processes considering fabrication costs.[71b, 71d, 84b, 177] The analyses of strategies in device architectures (**Figure 13**) that led to the best lab-scale research-cell efficiencies provide important insights and promising trend that enhanced performance and stability can be achieved in PSCs and solar modules.[3, 177c, 178] From a historical view point, developments of PSC architectures could be separated into three stages. In the first stage, the replacement of liquid electrolyte to solid state HTL was a major breakthrough;[179] the second stage is characterized by the perovskite composition engineering;[44] and the current third stage is characterized by the interface engineering (or passivation) that boosted the certified efficiencies higher than 22.67%.[83, 84d] For example, Noh, Seo and co-workers[83, 180] employed n-hexyl trimethyl ammonium bromide (HTAB) inserted between P3HT and $(FAPbI_3)_{0.95}(MAPbBr_3)_{0.05}$ perovskite layer. The $(N^+(CH_3)_3^-)$ moiety in HTAB coordinates with defects in Pb^{2+} undercoordinated defects in perovskites, while the aliphatic $(C_6H_{13}^-)$ moiety coordinates with P3HT via van der Waals interaction promoting self-assembly of P3HT on HTAB improving further hole extraction. This device structure led to the high certified PCE of 22.67% due to reduction of non-radiative recombination processes (i.e., defect passivation) and enhanced physical contact between perovskite and P3HT. In another recent work, You and co-workers[84d] employed PEAI as a passivation material and spin-coating on top of $FA_{1-x}MA_xPbI_3$ ($x \sim 0.08$) perovskite films. This strategy leads to the certified PCE of 23.3% in the NREL chart.[3] PEAI coating on the perovskite layer was proposed to heal defects by filling the iodine vacancies on the surface and at the grain boundaries.[84d] In all examples above, the dynamical processes of the interactions between passivating molecule and defect in perovskite was described on the basis of DFT calculations.[90j] It is important to note that identification of the different types of defects experimentally is imperative, but challenging (**Section 4** and **Table 2**). In this regard, computational studies are further expected to aid a more in-depth understanding of degradation dynamics, interfacial properties, and the role of defects on efficiency and stability that can be corroborated by surface science techniques.

Acknowledgements

This work was supported by funding from the Energy Materials and Surface Sciences Unit of the Okinawa Institute of Science and Technology Graduate University, the OIST R&D Cluster Research Program, the OIST Proof of Concept (POC) Program, and JSPS KAKENHI Grant Number JP18K05266.

Received: ((will be filled in by the editorial staff))
Revised: ((will be filled in by the editorial staff))
Published online: ((will be filled in by the editorial staff))

References

[1] N.-G. Park, H. Segawa, *ACS Photonics* **2018,** *5*, 2970.
[2] K. Yoshikawa, H. Kawasaki, W. Yoshida, T. Irie, K. Konishi, K. Nakano, T. Uto, D. Adachi, M. Kanematsu, H. Uzu, K. Yamamoto, *Nat. Energy* **2017,** *2*, 17032.
[3] *National Renewable Energy Laboratory (NREL). Research-Cell Efficiency Chart.* *https://www.nrel.gov/pv/cell-efficiency.html and Champion Module Efficiency Chart.* *https://www.nrel.gov/pv/module-efficiency.html* (Accessed August 11th).
[4] Z. Chen, B. Turedi, A. Y. Alsalloum, C. Yang, X. Zheng, I. Gereige, A. AlSaggaf, O. F. Mohammed, O. M. Bakr, *ACS Energy Lett.* **2019,** *4*, 1258.
[5] Y. Wang, M. I. Dar, L. K. Ono, T. Zhang, M. Kan, Y. Li, L. Zhang, X. Wang, Y. Yang, X. Gao, Y. Qi, M. Grätzel, Y. Zhao, *Science* **2019,** *365*, 591.
[6] S. Yang, S. Chen, E. Mosconi, Y. Fang, X. Xiao, C. Wang, Y. Zhou, Z. Yu, J. Zhao, Y. Gao, F. De Angelis, J. Huang, *Science* **2019,** *365*, 473.
[7] (a) E. Aydin, M. De Bastiani, S. De Wolf, *Adv. Mater.* **2019,** *31*, 1900428; (b) B. Chen, P. N. Rudd, S. Yang, Y. Yuan, J. Huang, *Chem. Soc. Rev.* **2019,** *48*, 3842; (c) Y. Rakita, I. Lubomirsky, D. Cahen, *Mater. Horizons* **2019,** *6*, 1297.
[8] (a) A. S. Thind, G. Luo, J. A. Hachtel, M. V. Morrell, S. B. Cho, A. Y. Borisevich, J.-C. Idrobo, Y. Xing, R. Mishra, *Adv. Mater.* **2019,** *31*, 1805047; (b) Y. Zhou, O. S. Game, S. Pang, N. P. Padture, *J. Phys. Chem. Lett.* **2015,** *6*, 4827.
[9] (a) J. Shi, Y. Li, Y. Li, D. Li, Y. Luo, H. Wu, Q. Meng, *Joule* **2018,** *2*, 879; (b) W. Tress, *Adv. Energy Mater.* **2017,** *7*, 1602358.
[10] (a) J.-J. Li, J.-Y. Ma, Q.-Q. Ge, J.-S. Hu, D. Wang, L.-J. Wan, *ACS Appl. Mater. Interfaces* **2015,** *7*, 28518; (b) J. S. Yun, A. Ho-Baillie, S. Huang, S. H. Woo, Y. Heo, J. Seidel, F. Huang, Y.-B. Cheng, M. A. Green, *J. Phys. Chem. Lett.* **2015,** *6*, 875; (c) J. Xu, A. Buin, A. H. Ip, W. Li, O. Voznyy, R. Comin, M. Yuan, S. Jeon, Z. Ning, J. J. McDowell, P. Kanjanaboos, J.-P. Sun, X. Lan, L. N. Quan, D. H. Kim, I. G. Hill, P. Maksymovych, E. H. Sargent, *Nat. Commun.* **2015,** *6*, 7081; (d) Y. Kutes, Y. Zhou, J. L. Bosse, J. Steffes, N. P. Padture, B. D. Huey, *Nano Lett.* **2016,** *16*, 3434; (e) S. Y. Leblebici, L. Leppert, Y. Li, S. E. Reyes-Lillo, S. Wickenburg, E. Wong, J. Lee, M.

Melli, D. Ziegler, D. K. Angell, D. F. Ogletree, Paul D. Ashby, F. M. Toma, J. B. Neaton, I. D. Sharp, A. Weber-Bargioni, *Nat. Energy* **2016,** *1*, 16093; (f) Z. Zhao, X. Chen, H. Wu, X. Wu, G. Cao, *Adv. Funct. Mater.* **2016,** *26*, 3048; (g) Y. Shao, Y. Fang, T. Li, Q. Wang, Q. Dong, Y. Deng, Y. Yuan, H. Wei, M. Wang, A. Gruverman, J. Shield, J. Huang, *Energy Environ. Sci.* **2016,** *9*, 1752.

[11] L. K. Ono, Y. B. Qi, *J. Phys. Chem. Lett.* **2016,** *7*, 4764.

[12] (a) D.-H. Kang, N.-G. Park, *Adv. Mater.* **2019,** *31*, 1805214; (b) P. Liu, W. Wang, S. Liu, H. Yang, Z. Shao, *Adv. Energy Mater.* **2019,** *9*, 1803017; (c) S. A. L. Weber, I. M. Hermes, S.-H. Turren-Cruz, C. Gort, V. W. Bergmann, L. Gilson, A. Hagfeldt, M. Graetzel, W. Tress, R. Berger, *Energy Environ. Sci.* **2018,** *11*, 2404; (d) J.-W. Lee, S.-H. Bae, N. De Marco, Y.-T. Hsieh, Z. Dai, Y. Yang, *Mater. Today Energy* **2018,** *7*, 149.

[13] (a) D.-Y. Son, J.-W. Lee, Y. J. Choi, I.-H. Jang, S. Lee, P. J. Yoo, H. Shin, N. Ahn, M. Choi, D. Kim, N.-G. Park, *Nat. Energy* **2016,** *1*, 16081; (b) C. Lu, Z. Hu, Y. Wang, K. Sun, B. Shen, C. Gao, C. Yang, J. Zhang, Y. Zhu, *Adv. Mater. Interfaces* **2019,** *6*, 1801253.

[14] (a) Z. Wu, S. R. Raga, E. J. Juarez-Perez, X. Yao, Y. Jiang, L. K. Ono, Z. Ning, H. Tian, Y. B. Qi, *Adv. Mater.* **2017,** *29*, 1703670; (b) X. Zheng, B. Chen, J. Dai, Y. Fang, Y. Bai, Y. Lin, H. Wei, Xiao C. Zeng, J. Huang, **2017,** *2*, 17102; (c) X. Zheng, Y. Deng, B. Chen, H. Wei, X. Xiao, Y. Fang, Y. Lin, Z. Yu, Y. Liu, Q. Wang, J. Huang, *Adv. Mater.* **2018**, 1803428; (d) F. Zhang, D. Q. Bi, N. Pellet, C. X. Xiao, Z. Li, J. J. Berry, S. M. Zakeeruddin, K. Zhu, M. Gratzel, *Energy Environ. Sci.* **2018,** *11*, 3480; (e) T. Niu, J. Lu, R. Munir, J. Li, D. Barrit, X. Zhang, H. Hu, Z. Yang, A. Amassian, K. Zhao, S. Liu, *Adv. Mater.* **2018,** *30*, 1706576; (f) C.-T. Lin, F. De Rossi, J. Kim, J. Baker, J. Ngiam, B. Xu, S. Pont, N. Aristidou, S. A. Haque, T. Watson, M. A. McLachlan, J. R. Durrant, *J. Mater. Chem. A* **2019,** *7*, 3006; (g) Z. Wang, A. Pradhan, M. A. Kamarudin, M. Pandey, S. S. Pandey, P. Zhang, C. H. Ng, A. S. M. Tripathi, T. Ma, S. Hayase, *ACS Appl Mater Interfaces* **2019,** *11*, 10012; (h) S. Ye, H. Rao, Z. Zhao, L. Zhang, H. Bao, W. Sun, Y. Li, F. Gu, J. Wang, Z. Liu, Z. Bian, C. Huang, *J. Am. Chem. Soc.* **2017,** *139*, 7504; (i) M. Wang, B. Li, J. Yuan, F. Huang, G. Cao, J. Tian, *ACS Appl. Mater. Interfaces* **2018,** *10*, 37005; (j) W. Gao, K. Zielinski, B. N. Drury, A. D. Carl, R. L. Grimm, *J. Phys. Chem. C* **2018,** *122*, 17882; (k) S. Yang, J. Dai, Z. Yu, Y. Shao, Y. Zhou, X. Xiao, X. C. Zeng, J. Huang, *J. Am. Chem. Soc.* **2019**, DOI: 10.1021/jacs.8b13091; (l) W.-Q. Wu, Z. Yang, P. N. Rudd, Y. Shao, X. Dai, H. Wei, J. Zhao, Y. Fang, Q. Wang, Y. Liu, Y. Deng, X. Xiao, Y. Feng, J. Huang, *Sci. Adv.* **2019,** *5*, eaav8925.

[15] M.-C. Shih, S.-S. Li, C.-H. Hsieh, Y.-C. Wang, H.-D. Yang, Y.-P. Chiu, C.-S. Chang, C.-W. Chen, *Nano Lett.* **2017,** *17*, 1154.

[16] T. Hwang, D. Cho, J. Kim, J. Kim, S. Lee, B. Lee, K. H. Kim, S. Hong, C. Kim, B. Park, *Nano Energy* **2016,** *25*, 91.

[17] G. E. Eperon, D. Moerman, D. S. Ginger, *ACS Nano* **2016,** *10*, 10258.

[18] K. Lu, Y. Lei, R. Qi, J. Liu, X. Yang, Z. Jia, R. Liu, Y. Xiang, Z. Zheng, *J. Mater. Chem. A* **2017,** *5*, 25211.

[19] (a) D. W. deQuilettes, S. M. Vorpahl, S. D. Stranks, H. Nagaoka, G. E. Eperon, M. E. Ziffer, H. J. Snaith, D. S. Ginger, *Science* **2015,** *348*, 683; (b) N. K. Noel, A. Abate, S. D. Stranks, E. S. Parrott, V. M. Burlakov, A. Goriely, H. J. Snaith, *ACS Nano* **2014,** *8*, 9815.

[20] L. S. C. Pingree, O. G. Reid, D. S. Ginger, *Adv. Mater.* **2009,** *21*, 19.

[21] V. W. Bergmann, S. A. L. Weber, F. Javier Ramos, M. K. Nazeeruddin, M. Grätzel, D. Li, A. L. Domanski, I. Lieberwirth, S. Ahmad, R. Berger, *Nat. Commun.* **2014,** *5*, 5001.

[22] M. Cai, N. Ishida, X. Li, X. Yang, T. Noda, Y. Wu, F. Xie, H. Naito, D. Fujita, L. Han, *Joule* **2018,** *2*, 296.

[23] S. Panigrahi, S. Jana, T. Calmeiro, D. Nunes, R. Martins, E. Fortunato, *ACS Nano* **2017,** *11*, 10214.

[24] (a) A. Guerrero, E. J. Juarez-Perez, J. Bisquert, I. Mora-Sero, G. Garcia-Belmonte, *Appl. Phys. Lett.* **2014,** *105*, 133902; (b) C.-S. Jiang, M. Yang, Y. Zhou, B. To, S. U. Nanayakkara, J. M. Luther, W. Zhou, J. J. Berry, J. van de Lagemaat, N. P. Padture, K. Zhu, M. M. Al-Jassim, *Nat. Commun.* **2015,** *6*, 8397; (c) V. W. Bergmann, Y. Guo, H. Tanaka, I. M. Hermes, D. Li, A. Klasen, S. A. Bretschneider, E. Nakamura, R. Berger, S. A. L. Weber, *ACS Appl. Mater. Interfaces* **2016,** *8*, 19402; (d) Z. Li, C. Xiao, Y. Yang, S. P. Harvey, D. H. Kim, J. A. Christians, M. Yang, P. Schulz, S. U. Nanayakkara, C.-S. Jiang, J. M. Luther, J. J. Berry, M. C. Beard, M. M. Al-Jassim, K. Zhu, *Energy Environ. Sci.* **2017,** *10*, 1234; (e) J. Will, Y. Hou, S. Scheiner, U. Pinkert, I. M. Hermes, S. A. L. Weber, A. Hirsch, M. Halik, C. Brabec, T. Unruh, *ACS Appl. Mater. Interfaces* **2018,** *10*, 5511; (f) P. Cui, D. Wei, J. Ji, H. Huang, E. Jia, S. Dou, T. Wang, W. Wang, M. Li, *Nat. Energy* **2019,** *4*, 150; (g) Z. Kang, H. Si, M. Shi, C. Xu, W. Fan, S. Ma, A. Kausar, Q. Liao, Z. Zhang, Y. Zhang, *Sci. China. Mater.* **2019,** *62*, 776.

[25] L. K. Ono, Y. B. Qi, *J. Phys. D. Appl. Phys.* **2018,** *51*, 093001.

[26] H. C. Hsu, B. C. Huang, S. C. Chin, C. R. Hsing, D. L. Nguyen, M. Schnedler, R. Sankar, R. E. Dunin-Borkowski, C. M. Wei, C. W. Chen, P. Ebert, Y. P. Chiu, *ACS Nano* **2019,** *13*, 4402.

[27] J. Hieulle, X. Wang, C. Stecker, D.-Y. Son, L. Qiu, R. Ohmann, L. K. Ono, A. Mugarza, Y. Yan, Y. B. Qi, *J. Am. Chem. Soc.* **2019,** *141*, 3515.

[28] (a) L. D. Whalley, J. M. Frost, Y.-K. Jung, A. Walsh, *J. Chem. Phys.* **2017,** *146*, 220901; (b) D. A. Egger, A. M. Rappe, L. Kronik, *Acc. Chem. Res.* **2016,** *49*, 573.

[29] (a) X. Wu, L. Z. Tan, X. Shen, T. Hu, K. Miyata, M. T. Trinh, R. Li, R. Coffee, S. Liu, D. A. Egger, I. Makasyuk, Q. Zheng, A. Fry, J. S. Robinson, M. D. Smith, B. Guzelturk, H. I. Karunadasa, X. Wang, X. Zhu, L. Kronik, A. M. Rappe, A. M. Lindenberg, *Sci. Adv.* **2017,** *3*, e1602388; (b) A. N. Beecher, O. E. Semonin, J. M. Skelton, J. M. Frost, M. W. Terban, H. Zhai, A. Alatas, J. S. Owen, A. Walsh, S. J. L. Billinge, *ACS Energy Lett.* **2016,** *1*, 880; (c) J. Gong, M. Yang, X. Ma, R. D. Schaller, G. Liu, L. Kong, Y. Yang, M. C. Beard, M. Lesslie, Y. Dai, B. Huang, K. Zhu, T. Xu, *J. Phys. Chem. Lett.* **2016,** *7*, 2879; (d) J. M. Frost, A. Walsh, *Acc. Chem. Res.* **2016,** *49*, 528; (e) A. M. A. Leguy, J. M. Frost, A. P. McMahon, V. G. Sakai, W. Kockelmann, C. Law, X. Li, F. Foglia, A. Walsh, B. C. O/'Regan, J. Nelson, J. T. Cabral, P. R. F. Barnes, *Nat. Commun.* **2015,** *6*, 7124.

[30] D. A. Egger, A. Bera, D. Cahen, G. Hodes, T. Kirchartz, L. Kronik, R. Lovrincic, A. M. Rappe, D. R. Reichman, O. Yaffe, *Adv. Mater.* **2018,** *30*, 1800691.

[31] J. M. Frost, K. T. Butler, F. Brivio, C. H. Hendon, M. van Schilfgaarde, A. Walsh, *Nano Lett.* **2014,** *14*, 2584.

[32] A. Pecchia, D. Gentilini, D. Rossi, M. Auf der Maur, A. Di Carlo, *Nano Lett.* **2016,** *16*, 988.

[33] H. Röhm, T. Leonhard, A. D. Schulz, S. Wagner, M. J. Hoffmann, A. Colsmann, *Adv. Mater.* **2019,** *31*, 1806661.

[34] S. G, P. Mahale, B. P. Kore, S. Mukherjee, M. S. Pavan, C. De, S. Ghara, A. Sundaresan, A. Pandey, T. N. Guru Row, D. D. Sarma, *J. Phys. Chem. Lett.* **2016**, 2412.

[35] (a) H. Röhm, T. Leonhard, M. J. Hoffmann, A. Colsmann, *Energy Environ. Sci.* **2017,** *10*, 950; (b) P. Wang, J. Zhao, L. Wei, Q. Zhu, S. Xie, J. Liu, X. Meng, J. Li, *Nanoscale* **2017,** *9*, 3806; (c) Y. Kutes, L. Ye, Y. Zhou, S. Pang, B. D. Huey, N. P.

Padture, *J. Phys. Chem. Lett.* **2014,** *5*, 3335; (d) B. Chen, X. Zheng, M. Yang, Y. Zhou, S. Kundu, J. Shi, K. Zhu, S. Priya, *Nano Energy* **2015,** *13*, 582; (e) H.-S. Kim, S. K. Kim, B. J. Kim, K.-S. Shin, M. K. Gupta, H. S. Jung, S.-W. Kim, N.-G. Park, *J. Phys. Chem. Lett.* **2015,** *6*, 1729; (f) B. Chen, J. Shi, X. Zheng, Y. Zhou, K. Zhu, S. Priya, *J. Mater. Chem. A* **2015,** *3*, 7699; (g) Y.-J. Kim, T.-V. Dang, H.-J. Choi, B.-J. Park, J.-H. Eom, H.-A. Song, D. Seol, Y. Kim, S.-H. Shin, J. Nah, S.-G. Yoon, *J. Mater. Chem. A* **2016,** *4*, 756; (h) I. M. Hermes, S. A. Bretschneider, V. W. Bergmann, D. Li, A. Klasen, J. Mars, W. Tremel, F. Laquai, H.-J. Butt, M. Mezger, R. Berger, B. J. Rodriguez, S. A. L. Weber, *J. Phys. Chem. C* **2016,** *120*, 5724.

[36] (a) E. Strelcov, Q. Dong, T. Li, J. Chae, Y. Shao, Y. Deng, A. Gruverman, J. Huang, A. Centrone, *Sci. Adv.* **2017,** *3*, e1602165; (b) Z. Xiao, Y. Yuan, Y. Shao, Q. Wang, Q. Dong, C. Bi, P. Sharma, A. Gruverman, J. Huang, *Nat Mater* **2015,** *14*, 193; (c) M. Coll, A. Gomez, E. Mas-Marza, O. Almora, G. Garcia-Belmonte, M. Campoy-Quiles, J. Bisquert, *J. Phys. Chem. Lett.* **2015,** *6*, 1408; (d) Z. Fan, J. Xiao, K. Sun, L. Chen, Y. Hu, J. Ouyang, K. P. Ong, K. Zeng, J. Wang, *J. Phys. Chem. Lett.* **2015,** *6*, 1155.

[37] M. U. Rothmann, W. Li, Y. Zhu, U. Bach, L. Spiccia, J. Etheridge, Y.-B. Cheng, *Nat. Commun.* **2017,** *8*, 14547.

[38] J. Hieulle, C. Stecker, R. Ohmann, L. K. Ono, Y. B. Qi, *Small Methods* **2018,** *2*, 1700295.

[39] T. W. Kim, S. Uchida, T. Matsushita, L. Cojocaru, R. Jono, K. Kimura, D. Matsubara, M. Shirai, K. Ito, H. Matsumoto, T. Kondo, H. Segawa, *Adv. Mater.* **2018,** *30*, 1705230.

[40] (a) E. T. Hoke, D. J. Slotcavage, E. R. Dohner, A. R. Bowring, H. I. Karunadasa, M. D. McGehee, *Chem. Sci.* **2015,** *6*, 613; (b) D. J. Slotcavage, H. I. Karunadasa, M. D. McGehee, *ACS Energy Lett.* **2016,** *1*, 1199; (c) E. L. Unger, L. Kegelmann, K. Suchan, D. Sörell, L. Korte, S. Albrecht, *J. Mater. Chem. A* **2017,** *5*, 11401.

[41] C. G. Bischak, C. L. Hetherington, H. Wu, S. Aloni, D. F. Ogletree, D. T. Limmer, N. S. Ginsberg, *Nano Lett.* **2017,** *17*, 1028.

[42] (a) R. Ohmann, L. K. Ono, H.-S. Kim, H. Lin, M. V. Lee, Y. Li, N.-G. Park, Y. B. Qi, *J. Am. Chem. Soc.* **2015,** *137*, 16049; (b) L. She, M. Liu, D. Zhong, *ACS Nano* **2016,** *10*, 1126; (c) L. She, M. Liu, X. Li, Z. Cai, D. Zhong, *Surf. Sci.* **2017,** *656*, 17; (d) L. Cai, L. She, H. Qin, L. Xu, D. Zhong, *Surf. Sci.* **2018,** *675*, 78; (e) A. J. Yost, A. Pimachev, C.-C. Ho, S. B. Darling, L. Wang, W.-F. Su, Y. Dahnovsky, T. Chien, *ACS Appl. Mater. Interfaces* **2016,** *8*, 29110.

[43] (a) Q. Sun, P. Fassl, Y. Vaynzof, *ACS Appl. Energy Mater.* **2018,** *1*, 2410; (b) J.-P. Correa-Baena, Y. Luo, T. M. Brenner, J. Snaider, S. Sun, X. Li, M. A. Jensen, N. T. P. Hartono, L. Nienhaus, S. Wieghold, J. R. Poindexter, S. Wang, Y. S. Meng, T. Wang, B. Lai, M. V. Holt, Z. Cai, M. G. Bawendi, L. Huang, T. Buonassisi, D. P. Fenning, *Science* **2019,** *363*, 627; (c) S. Wieghold, J. Tresback, J.-P. Correa-Baena, N. T. P. Hartono, S. Sun, Z. Liu, M. Layurova, Z. A. VanOrman, A. S. Bieber, J. Thapa, B. Lai, Z. Cai, L. Nienhaus, T. Buonassisi, *Chem. Mater.* **2019,** *31*, 3712; (d) M. Vrućinić, C. Matthiesen, A. Sadhanala, G. Divitini, S. Cacovich, S. E. Dutton, C. Ducati, M. Atatüre, H. Snaith, R. H. Friend, H. Sirringhaus, F. Deschler, *Adv. Sci.* **2015,** *2*, 1500136; (e) J. Chae, Q. Dong, J. Huang, A. Centrone, *Nano Lett.* **2015,** *15*, 8114; (f) H. R. Jung, B. P. Nguyen, H.-J. Jin, T. T. T. Nguyen, S. Yoon, W. S. Woo, C. W. Ahn, S. Cho, I. W. Kim, W. Jo, *CrystEngComm* **2018,** *20*, 6551; (g) B. Philippe, M. Saliba, J.-P. Correa-Baena, U. B. Cappel, S.-H. Turren-Cruz, M. Grätzel, A. Hagfeldt, H. Rensmo, *Chem. Mater.* **2017,** *29*, 3589.

[44] L. K. Ono, E. J. Juárez-Pérez, Y. B. Qi, *ACS Appl. Mater. Interfaces* **2017,** *9*, 30197.

[45] (a) R. Brenes, D. Guo, A. Osherov, N. K. Noel, C. Eames, E. M. Hutter, S. K. Pathak, F. Niroui, R. H. Friend, M. S. Islam, H. J. Snaith, V. Bulović, T. J. Savenije, S. D.

Stranks, *Joule* **2017,** *1*, 155; (b) R. Brenes, C. Eames, V. Bulović, M. S. Islam, S. D. Stranks, *Adv. Mater.* **2018,** *30*, 1706208.

[46] G. Paul, S. Chatterjee, H. Bhunia, A. J. Pal, *J. Phys. Chem. C* **2018,** *122*, 20194.

[47] (a) U. Dasgupta, A. Bera, A. J. Pal, *ACS Energy Lett.* **2017,** *2*, 582; (b) S. Chatterjee, A. J. Pal, *J. Mater. Chem. A* **2018,** *6*, 3793.

[48] (a) A. Kahn, *Mater. Horizons* **2016,** *3*, 7; (b) S. Wang, T. Sakurai, W. Wen, Y. B. Qi, *Adv. Mater. Interfaces* **2018,** *5*, 1800260; (c) P. Schulz, D. Cahen, A. Kahn, *Chem. Rev.* **2019,** *119*, 3349.

[49] (a) P. Schulz, E. Edri, S. Kirmayer, G. Hodes, D. Cahen, A. Kahn, *Energy Environ. Sci.* **2014,** *7*, 1377; (b) J. Endres, D. A. Egger, M. Kulbak, R. A. Kerner, L. Zhao, S. H. Silver, G. Hodes, B. P. Rand, D. Cahen, L. Kronik, A. Kahn, *J. Phys. Chem. Lett.* **2016,** *7*, 2722; (c) S. Tao, I. Schmidt, G. Brocks, J. Jiang, I. Tranca, K. Meerholz, S. Olthof, *Nat. Commun.* **2019,** *10*, 2560; (d) D. Shin, D. Kang, J. Jeong, S. Park, M. Kim, H. Lee, Y. Yi, *J. Phys. Chem. Lett.* **2017,** *8*, 5423; (e) P. Caprioglio, F. Zu, C. M. Wolff, J. A. Márquez Prieto, M. Stolterfoht, P. Becker, N. Koch, T. Unold, B. Rech, S. Albrecht, D. Neher, *Sustain. Energ. Fuels* **2019,** *3*, 550; (f) C. Wang, C. Wang, X. Liu, J. Kauppi, Y. Shao, Z. Xiao, C. Bi, J. Huang, Y. Gao, *Appl. Phys. Lett.* **2015,** *106*, 111603; (g) C. Wang, X. Liu, C. Wang, Z. Xiao, C. Bi, Y. Shao, J. Huang, Y. Gao, *J. Vac. Sci. Technol. B* **2015,** *33*, 032401; (h) J. Endres, M. Kulbak, L. Zhao, B. P. Rand, D. Cahen, G. Hodes, A. Kahn, *J. Appl. Phys.* **2017,** *121*, 035304; (i) C. Wang, B. R. Ecker, H. Wei, J. Huang, J.-Q. Meng, Y. Gao, *Phys. Chem. Chem. Phys.* **2017,** *19*, 5361; (j) M.-C. Jung, S. R. Raga, L. K. Ono, Y. B. Qi, *Sci. Rep.* **2015,** *5*, 9863; (k) Z. Wu, Z. Liu, Z. Hu, Z. Hawash, L. Qiu, Y. Jiang, L. K. Ono, Y. B. Qi, *Adv. Mater.* **2019,** *31*, 1804284; (l) Y. Jiang, M. R. Leyden, L. Qiu, S. Wang, L. K. Ono, Z. Wu, E. J. Juarez-Perez, Y. B. Qi, *Adv. Funct. Mater.* **2018,** *28*, 1703835; (m) Z. Hawash, S. R. Raga, D.-Y. Son, L. K. Ono, N.-G. Park, Y. B. Qi, *J. Phys. Chem. Lett.* **2017,** *8*, 3947; (n) J. Liang, Z. Liu, L. Qiu, Z. Hawash, L. Meng, Z. Wu, Y. Jiang, L. K. Ono, Y. B. Qi, *Adv. Energy Mater.* **2018,** *8*, 1800504; (o) D. Luo, W. Yang, Z. Wang, A. Sadhanala, Q. Hu, R. Su, R. Shivanna, G. F. Trindade, J. F. Watts, Z. Xu, T. Liu, K. Chen, F. Ye, P. Wu, L. Zhao, J. Wu, Y. Tu, Y. Zhang, X. Yang, W. Zhang, R. H. Friend, Q. Gong, H. J. Snaith, R. Zhu, *Science* **2018,** *360*, 1442; (p) K. Yan, J. Chen, H. Ju, F. Ding, H. Chen, C.-Z. Li, *J. Mater. Chem. A* **2018,** *6*, 15495; (q) C. Li, J. Wei, M. Sato, H. Koike, Z.-Z. Xie, Y.-Q. Li, K. Kanai, S. Kera, N. Ueno, J.-X. Tang, *ACS Appl. Mater. Interfaces* **2016,** *8*, 11526; (r) R. Comin, G. Walters, E. S. Thibau, O. Voznyy, Z.-H. Lu, E. H. Sargent, *J. Mater. Chem. C* **2015,** *3*, 8839; (s) E. M. Miller, Y. Zhao, C. C. Mercado, S. K. Saha, J. M. Luther, K. Zhu, V. Stevanović, C. L. Perkins, J. van de Lagemaat, *Phys. Chem. Chem. Phys.* **2014,** *16*, 22122; (t) Q.-D. Ou, C. Li, Q.-K. Wang, Y.-Q. Li, J.-X. Tang, *Adv. Mater. Interfaces* **2017,** *4*, 1600694.

[50] (a) A. Miyata, A. Mitioglu, P. Plochocka, O. Portugall, J. T.-W. Wang, S. D. Stranks, H. J. Snaith, R. J. Nicholas, *Nat. Phys.* **2015,** *11*, 582; (b) X. Chen, H. Lu, Y. Yang, M. C. Beard, *J. Phys. Chem. Lett.* **2018,** *9*, 2595; (c) F. Ruf, M. F. Aygüler, N. Giesbrecht, B. Rendenbach, A. Magin, P. Docampo, H. Kalt, M. Hetterich, *APL Mater.* **2019,** *7*, 031113.

[51] S. Prathapani, P. Bhargava, S. Mallick, *Appl. Phys. Lett.* **2018,** *112*, 092104.

[52] F. Zu, P. Amsalem, D. A. Egger, R. Wang, C. M. Wolff, H. Fang, M. A. Loi, D. Neher, L. Kronik, S. Duhm, N. Koch, *J. Phys. Chem. Lett.* **2019,** *10*, 601.

[53] R. E. Brandt, V. Stevanović, D. S. Ginley, T. Buonassisi, *MRS Commun.* **2015,** *5*, 265.

[54] M.-I. Lee, A. Barragán, M. N. Nair, V. L. R. Jacques, D. Le Bolloc'h, P. Fertey, K. Jemli, F. Lédée, G. Trippé-Allard, E. Deleporte, A. Taleb-Ibrahimi, A. Tejeda, *J. Phys. D. Appl. Phys.* **2017,** *50*, 26LT02.

[55] (a) F. Zu, P. Amsalem, M. Ralaiarisoa, T. Schultz, R. Schlesinger, N. Koch, *ACS Appl. Mater. Interfaces* **2017,** *9*, 41546; (b) F.-S. Zu, P. Amsalem, I. Salzmann, R.-B. Wang, M. Ralaiarisoa, S. Kowarik, S. Duhm, N. Koch, *Adv. Optical Mater.* **2017,** *5*, 1700139.

[56] D. Meggiolaro, E. Mosconi, F. De Angelis, *ACS Energy Lett.* **2019,** *4*, 779.

[57] P. Schulz, L. L. Whittaker-Brooks, B. A. MacLeod, D. C. Olson, Y.-L. Loo, A. Kahn, *Adv. Mater. Interfaces* **2015,** *2*, 1400532.

[58] (a) W.-J. Yin, T. Shi, Y. Yan, *Appl. Phys. Lett.* **2014,** *104*, 063903; (b) E. J. Juarez-Perez, Z. Hawash, S. R. Raga, L. K. Ono, Y. B. Qi, *Energy Environ. Sci.* **2016,** *9*, 3406.

[59] (a) Y. Zou, Q. Meng, H. Mao, D. Zhu, *Org. Electron.* **2017,** *41*, 307; (b) S. Olthof, K. Meerholz, *Sci. Rep.* **2017,** *7*, 40267; (c) K.-G. Lim, S. Ahn, Y.-H. Kim, Y. B. Qi, T.-W. Lee, *Energy Environ. Sci.* **2016,** *9*, 932; (d) X. Zhou, X. Li, Y. Liu, F. Huang, D. Zhong, *Appl. Phys. Lett.* **2016,** *108*, 121601.

[60] S. Olthof, *APL Mater.* **2016,** *4*, 091502.

[61] Q.-K. Wang, R.-B. Wang, P.-F. Shen, C. Li, Y.-Q. Li, L.-J. Liu, S. Duhm, J.-X. Tang, *Adv. Mater. Interfaces* **2015,** *2*, 1400528.

[62] X. Liu, C. Wang, L. Lyu, C. Wang, Z. Xiao, C. Bi, J. Huang, Y. Gao, *Phys. Chem. Chem. Phys.* **2015,** *17*, 896.

[63] (a) Y. Zhao, A. M. Nardes, K. Zhu, *Appl. Phys. Lett.* **2014,** *104*, 213906; (b) P. Liu, X. Liu, L. Lyu, H. Xie, H. Zhang, D. Niu, H. Huang, C. Bi, Z. Xiao, J. Huang, Y. Gao, *Appl. Phys. Lett.* **2015,** *106*, 193903.

[64] S. Chen, T. W. Goh, D. Sabba, J. Chua, N. Mathews, C. H. A. Huan, T. C. Sum, *APL Mater.* **2014,** *2*, 081512.

[65] G. Ji, B. Zhao, F. Song, G. Zheng, X. Zhang, K. Shen, Y. Yang, S. Chen, X. Gao, *Appl. Surf. Sci.* **2017,** *393*, 417.

[66] M.-F. Lo, Z.-Q. Guan, T.-W. Ng, C.-Y. Chan, C.-S. Lee, *Adv. Funct. Mater.* **2015,** *25*, 1213.

[67] A. Zohar, M. Kulbak, I. Levine, G. Hodes, A. Kahn, D. Cahen, *ACS Energy Lett.* **2019,** *4*, 1.

[68] H. Wang, A. Guerrero, A. Bou, A. M. Al-Mayouf, J. Bisquert, *Energy Environ. Sci.* **2019,** *12*, 2054.

[69] M. Kulbak, I. Levine, E. Barak‐Kulbak, S. Gupta, A. Zohar, I. Balberg, G. Hodes, D. Cahen, *Adv. Energy Mater.* **2018,** *8*, 1800398.

[70] P. Fassl, V. Lami, A. Bausch, Z. Wang, M. T. Klug, H. J. Snaith, Y. Vaynzof, *Energy Environ. Sci.* **2018,** *11*, 3380.

[71] (a) I. A. Howard, T. Abzieher, I. M. Hossain, H. Eggers, F. Schackmar, S. Ternes, B. S. Richards, U. Lemmer, U. W. Paetzold, *Adv. Mater.* **2019,** *31*, 1806702; (b) L. Qiu, L. K. Ono, Y. B. Qi, *Mater. Today Energy* **2018,** *7*, 169; (c) M. Remeika, Y. B. Qi, *J. Energy Chem.* **2018,** *27*, 1101; (d) L. K. Ono, M. R. Leyden, S. Wang, Y. B. Qi, *J. Mater. Chem. A* **2016,** *4*, 6693.

[72] (a) R. Wang, M.-P. Zhuo, J. Li, T. Zhai, J. Yang, K. Fu, L.-S. Liao, L. Liu, S. Duhm, *Adv. Mater. Interfaces* **2019,** *6*, 1801827; (b) R. Wang, C. Wu, Y. Hu, J. Li, P. Shen, Q. Wang, L. Liao, L. Liu, S. Duhm, *ACS Appl. Mater. Interfaces* **2017,** *9*, 7859; (c) J. Emara, T. Schnier, N. Pourdavoud, T. Riedl, K. Meerholz, S. Olthof, *Adv. Mater.* **2016,** *28*, 553; (d) H. Xie, X. Liu, L. Lyu, D. Niu, Q. Wang, J. Huang, Y. Gao, *J. Phys. Chem. C* **2016,** *120*, 215; (e) T. G. Kim, S. W. Seo, H. Kwon, J. Hahn, J. W. Kim, *Phys. Chem. Chem. Phys.* **2015,** *17*, 24342.

[73] S. Singh, D. Kabra, *J. Mater. Chem. C* **2018,** *6*, 12052.

[74] Q. Wang, Y. Shao, H. Xie, L. Lyu, X. Liu, Y. Gao, J. Huang, *Appl. Phys. Lett.* **2014,** *105*, 163508.

[75] (a) S. R. Raga, M.-C. Jung, M. V. Lee, M. R. Leyden, Y. Kato, Y. B. Qi, *Chem. Mater.* **2015,** *27*, 1597; (b) B. Conings, J. Drijkoningen, N. Gauquelin, A. Babayigit, J. D'Haen, L. D'Olieslaeger, A. Ethirajan, J. Verbeeck, J. Manca, E. Mosconi, F. D. Angelis, H.-G. Boyen, *Adv. Energy Mater.* **2015,** *5*, 1500477; (c) B. Conings, L. Baeten, C. De Dobbelaere, J. D'Haen, J. Manca, H.-G. Boyen, *Advanced Materials* **2014,** *26*, 2041.

[76] (a) W.-J. Yin, T. Shi, Y. Yan, *Adv. Mater.* **2014,** *26*, 4653; (b) W.-J. Yin, H. Chen, T. Shi, S.-H. Wei, Y. Yan, *Adv. Electron. Mater.* **2015,** *1*, 1500044.

[77] (a) L. Liu, J. A. McLeod, R. Wang, P. Shen, S. Duhm, *Appl. Phys. Lett.* **2015,** *107*, 061904; (b) W. Xu, L. Liu, L. Yang, P. Shen, B. Sun, J. A. McLeod, *Nano Lett.* **2016,** *16*, 4720.

[78] (a) M.-C. Jung, Y. M. Lee, H.-K. Lee, J. Park, S. R. Raga, L. K. Ono, S. Wang, M. R. Leyden, B. D. Yu, S. Hong, Y. B. Qi, *Appl. Phys. Lett.* **2016,** *108*, 073901; (b) I. Maeng, Y. M. Lee, J. Park, S. R. Raga, C. Kang, C.-S. Kee, B. D. Yu, S. Hong, L. K. Ono, Y. B. Qi, M.-C. Jung, M. Nakamura, *Sci. Rep.* **2019,** *9*, 5811.

[79] (a) E. J. Juarez-Perez, L. K. Ono, M. Maeda, Y. Jiang, Z. Hawash, Y. B. Qi, *J. Mater. Chem. A* **2018,** *6*, 9604; (b) E. J. Juarez-Perez, L. K. Ono, I. Uriarte, E. J. Cocinero, Y. B. Qi, *ACS Appl. Mater. Interfaces* **2019,** *11*, 12586.

[80] P. Willmott, *John Wiley & Sons, Ltd* **2011**, DOI:10.1002/9781119970958.

[81] M. Stolterfoht, P. Caprioglio, C. M. Wolff, J. A. Márquez, J. Nordmann, S. Zhang, D. Rothhardt, U. Hörmann, Y. Amir, A. Redinger, L. Kegelmann, F. Zu, S. Albrecht, N. Koch, T. Kirchartz, M. Saliba, T. Unold, D. Neher, *Energy Environ. Sci.* **2019**.

[82] (a) Q. Jiang, X. Zhang, J. You, *Small* **2018,** *14*, 1801154; (b) J. Urieta-Mora, I. García-Benito, A. Molina-Ontoria, N. Martín, *Chem. Soc. Rev.* **2018,** *47*, 8541; (c) P.-K. Kung, M.-H. Li, P.-Y. Lin, Y.-H. Chiang, C.-R. Chan, T.-F. Guo, P. Chen, *Adv. Mater. Interfaces* **2018,** *5*, 1800882.

[83] E. H. Jung, N. J. Jeon, E. Y. Park, C. S. Moon, T. J. Shin, T.-Y. Yang, J. H. Noh, J. Seo, *Nature* **2019,** *567*, 511.

[84] (a) L. Qiu, Z. Liu, L. K. Ono, Y. Jiang, D.-Y. Son, Z. Hawash, S. He, Y. B. Qi, *Adv. Funct. Mater.* **2018**, DOI: 10.1002/adfm.201806779; (b) L. Qiu, S. He, Y. Jiang, D.-Y. Son, L. K. Ono, Z. Liu, T. Kim, T. Bouloumis, S. Kazaoui, Y. B. Qi, *J. Mater. Chem. A* **2019,** *7*, 6920; (c) L. Qiu, L. K. Ono, Y. Jiang, M. R. Leyden, S. R. Raga, S. Wang, Y. B. Qi, *J. Phys. Chem. B* **2018,** *122*, 511; (d) Q. Jiang, Y. Zhao, X. Zhang, X. Yang, Y. Chen, Z. Chu, Q. Ye, X. Li, Z. Yin, J. You, *Nat. Photonics* **2019,** *13*, 460.

[85] C. Chen, Z. Song, C. Xiao, D. Zhao, N. Shrestha, C. Li, G. Yang, F. Yao, X. Zheng, R. J. Ellingson, C.-S. Jiang, M. Al-Jassim, K. Zhu, G. Fang, Y. Yan, *Nano Energy* **2019,** *61*, 141.

[86] J. J. Yoo, S. Wieghold, M. Sponseller, M. Chua, S. N. Bertram, N. T. P. Hartono, J. Tresback, E. Hansen, J.-P. Correa-Baena, V. Bulovic, T. Buonassisi, S. S. Shin, M. G. Bawendi, *Energy Environ. Sci.* **2019**.

[87] (a) J. M. Azpiroz, E. Mosconi, J. Bisquert, F. De Angelis, *Energy Environ. Sci.* **2015,** *8*, 2118; (b) A. J. Barker, A. Sadhanala, F. Deschler, M. Gandini, S. P. Senanayak, P. M. Pearce, E. Mosconi, A. J. Pearson, Y. Wu, A. R. Srimath Kandada, T. Leijtens, F. De Angelis, S. E. Dutton, A. Petrozza, R. H. Friend, *ACS Energy Lett.* **2017,** *2*, 1416; (c) Y. Yuan, J. Huang, *Acc. Chem. Res.* **2016,** *49*, 286; (d) A. Alkauskas, M. D. McCluskey, C. G. V. d. Walle, *J. Appl. Phys.* **2016,** *119*, 181101.

[88] J.-S. Park, A. Walsh, *Nat. Energy* **2019,** *4*, 95.

[89] S. G. Motti, D. Meggiolaro, A. J. Barker, E. Mosconi, C. A. R. Perini, J. M. Ball, M. Gandini, M. Kim, F. De Angelis, A. Petrozza, *Nat. Photonics* **2019,** *13*, 532.

[90] (a) S. Mahajan, *Acta Mater.* **2000,** *48*, 137; (b) J. S. Park, S. Kim, Z. Xie, A. Walsh, *Nat. Rev. Mater.* **2018,** *3*, 194; (c) J. M. Ball, A. Petrozza, *Nat. Energy* **2016,** *1*, 16149;

(d) T. M. Brenner, D. A. Egger, L. Kronik, G. Hodes, D. Cahen, *Nat. Rev. Mater.* **2016,** *1*, 15007; (e) J. L. Garrett, E. M. Tennyson, M. Hu, J. Huang, J. N. Munday, M. S. Leite, *Nano Lett.* **2017,** *17*, 2554; (f) S. Yun, X. Zhou, J. Even, A. Hagfeldt, *Angew. Chem. Int. Ed.* **2017,** *56*, 15806; (g) C. Ran, J. Xu, W. Gao, C. Huang, S. Dou, *Chem. Soc. Rev.* **2018,** *47*, 4581; (h) C.-J. Yu, *Journal of Physics: Energy* **2019,** *1*, 022001; (i) D. Meggiolaro, F. De Angelis, *ACS Energy Lett.* **2018,** *3*, 2206; (j) L. K. Ono, S. Liu, Y. B. Qi, *Angew. Chem. Int. Ed.* **2019**, DOI: 10.1002/ange.201905521.

[91] J. Peng, Y. Chen, K. Zheng, T. Pullerits, Z. Liang, *Chem. Soc. Rev.* **2017,** *46*, 5714.

[92] J. Kim, S.-H. Lee, J. H. Lee, K.-H. Hong, *J. Phys. Chem. Lett.* **2014,** *5*, 1312.

[93] Q. A. Akkerman, G. Rainò, M. V. Kovalenko, L. Manna, *Nat. Mater.* **2018,** *17*, 394.

[94] M. H. Du, *J. Mater. Chem. A* **2014,** *2*, 9091.

[95] M. L. Agiorgousis, Y.-Y. Sun, H. Zeng, S. Zhang, *J. Am. Chem. Soc.* **2014,** *136*, 14570.

[96] (a) W. S. Yang, B.-W. Park, E. H. Jung, N. J. Jeon, Y. C. Kim, D. U. Lee, S. S. Shin, J. Seo, E. K. Kim, J. H. Noh, S. I. Seok, *Science* **2017,** *356*, 1376; (b) S. Wang, Y. Jiang, Emilio J. Juarez-Perez, L. K. Ono, Y. B. Qi, *Nat. Energy* **2016,** *2*, 16195; (c) R. G. Wilks, M. Bär, *Nat. Energy* **2017,** *2*, 16204.

[97] M.-H. Du, *J. Phys. Chem. Lett.* **2015,** *6*, 1461.

[98] P. Xu, S. Chen, H.-J. Xiang, X.-G. Gong, S.-H. Wei, *Chem. Mater.* **2014,** *26*, 6068.

[99] W. Ming, H. Shi, M.-H. Du, *J. Mater. Chem. A* **2016,** *4*, 13852.

[100] J. Xu, J.-B. Liu, B.-X. Liu, B. Huang, *J. Phys. Chem. Lett.* **2017,** *8*, 4391.

[101] Z. Xiao, W. Meng, J. Wang, Y. Yan, *ChemSusChem* **2016,** *9*, 2628.

[102] (a) J. Haruyama, K. Sodeyama, L. Han, Y. Tateyama, *J. Phys. Chem. Lett.* **2014,** *5*, 2903; (b) J. Haruyama, K. Sodeyama, L. Han, Y. Tateyama, *Acc. Chem. Res.* **2016,** *49*, 554; (c) H. Uratani, K. Yamashita, *J. Phys. Chem. Lett.* **2017,** *8*, 742; (d) E. Mosconi, J. M. Azpiroz, F. De Angelis, *Chem. Mater.* **2015,** *27*, 4885; (e) C. Quarti, F. De Angelis, D. Beljonne, *Chem. Mater.* **2017,** *29*, 958; (f) J. Yin, D. Cortecchia, A. Krishna, S. Chen, N. Mathews, A. C. Grimsdale, C. Soci, *J. Phys. Chem. Lett.* **2015,** *6*, 1396; (g) W. Geng, C.-J. Tong, Z.-K. Tang, C. Yam, Y.-N. Zhang, W.-M. Lau, L.-M. Liu, *Journal of Materiomics* **2015,** *1*, 213; (h) L. Zhang, X. Liu, J. Li, S. McKechnie, *Sol. Energy Mater. Sol. Cells* **2018,** *175*, 1; (i) Y. Ouyang, Y. Li, P. Zhu, Q. Li, Y. Gao, J. Tong, L. Shi, Q. Zhou, C. Ling, Q. Chen, Z. Deng, H. Tan, W. Deng, J. Wang, *J. Mater. Chem. A* **2019,** *7*, 2275; (j) A. Torres, L. G. C. Rego, *J. Phys. Chem. C* **2014,** *118*, 26947; (k) Y. Wang, B. G. Sumpter, J. Huang, H. Zhang, P. Liu, H. Yang, H. Zhao, *J. Phys. Chem. C* **2015,** *119*, 1136.

[103] (a) Y. Liu, K. Palotas, X. Yuan, T. Hou, H. Lin, Y. Li, S.-T. Lee, *ACS Nano* **2017,** *11*, 2060; (b) X. Huang, T. R. Paudel, P. A. Dowben, S. Dong, E. Y. Tsymbal, *Physical Review B* **2016,** *94*, 195309.

[104] B. Akbali, G. Topcu, T. Guner, M. Ozcan, M. M. Demir, H. Sahin, *Phys. Rev. Mater.* **2018,** *2*, 034601.

[105] (a) R. Lindblad, D. Bi, B.-w. Park, J. Oscarsson, M. Gorgoi, H. Siegbahn, M. Odelius, E. M. J. Johansson, H. Rensmo, *J. Phys. Chem. Lett.* **2014,** *5*, 648; (b) S. D. Stranks, *ACS Energy Lett.* **2017,** *2*, 1515.

[106] D. Meggiolaro, S. G. Motti, E. Mosconi, A. J. Barker, J. Ball, C. Andrea Riccardo Perini, F. Deschler, A. Petrozza, F. De Angelis, *Energy Environ. Sci.* **2018,** *11*, 702.

[107] (a) J. Shi, X. Xu, D. Li, Q. Meng, *Small* **2015,** *11*, 2472; (b) A. Fakharuddin, L. Schmidt-Mende, G. Garcia-Belmonte, R. Jose, I. Mora-Sero, *Adv. Energy Mater.* **2017,** *7*, 1700623.

[108] (a) E. Mosconi, E. Ronca, F. De Angelis, *J. Phys. Chem. Lett.* **2014,** *5*, 2619; (b) S. Colella, E. Mosconi, G. Pellegrino, A. Alberti, V. L. P. Guerra, S. Masi, A. Listorti, A. Rizzo, G. G. Condorelli, F. De Angelis, G. Gigli, *J. Phys. Chem. Lett.* **2014,** *5*, 3532;

(c) E. Mosconi, G. Grancini, C. Roldán-Carmona, P. Gratia, I. Zimmermann, M. K. Nazeeruddin, F. De Angelis, *Chem. Mater.* **2016,** *28*, 3612; (d) V. Roiati, E. Mosconi, A. Listorti, S. Colella, G. Gigli, F. De Angelis, *Nano Lett.* **2014,** *14*, 2168; (e) F. De Angelis, *Acc. Chem. Res.* **2014,** *47*, 3349; (f) A. Akbari, J. Hashemi, E. Mosconi, F. De Angelis, M. Hakala, *J. Mater. Chem. A* **2017,** *5*, 2339; (g) R. Long, W.-H. Fang, O. V. Prezhdo, *J. Phys. Chem. C* **2017,** *121*, 3797; (h) J. Haruyama, K. Sodeyama, L. Han, Y. Tateyama, *J. Am. Chem. Soc.* **2015,** *137*, 10048; (i) W. Geng, C.-J. Tong, J. Liu, W. Zhu, W.-M. Lau, L.-M. Liu, *Sci. Rep.* **2016,** *6*, 20131; (j) L.-y. Wei, W. Ma, C. Lian, S. Meng, *J. Phys. Chem. C* **2017,** *121*, 5905; (k) R. Long, O. V. Prezhdo, *ACS Nano* **2015,** *9*, 11143; (l) H. Tan, A. Jain, O. Voznyy, X. Lan, F. P. García de Arquer, J. Z. Fan, R. Quintero-Bermudez, M. Yuan, B. Zhang, Y. Zhao, F. Fan, P. Li, L. N. Quan, Y. Zhao, Z.-H. Lu, Z. Yang, S. Hoogland, E. H. Sargent, *Science* **2017,** *355*, 722.

[109] H.-J. Feng, T. R. Paudel, E. Y. Tsymbal, X. C. Zeng, *J. Am. Chem. Soc.* **2015,** *137*, 8227.

[110] J. Yang, B. D. Siempelkamp, E. Mosconi, F. De Angelis, T. L. Kelly, *Chem. Mater.* **2015,** *27*, 4229.

[111] H.-J. Feng, J. Huang, X. C. Zeng, *Adv. Mater. Interfaces* **2016,** *3*, 1600267.

[112] C.-X. Qian, Z.-Y. Deng, K. Yang, J. Feng, M.-Z. Wang, Z. Yang, S. Liu, H.-J. Feng, *Appl. Phys. Lett.* **2018,** *112*, 093901.

[113] E. Edri, S. Kirmayer, A. Henning, S. Mukhopadhyay, K. Gartsman, Y. Rosenwaks, G. Hodes, D. Cahen, *Nano Lett.* **2014,** *14*, 1000.

[114] L. Liu, S. Huang, Y. Lu, P. Liu, Y. Zhao, C. Shi, S. Zhang, J. Wu, H. Zhong, M. Sui, H. Zhou, H. Jin, Y. Li, Q. Chen, *Adv. Mater.* **2018,** *30*, 1800544.

[115] Y. Zhao, Q. Li, W. Zhou, Y. Hou, Y. Zhao, R. Fu, D. Yu, X. Liu, Q. Zhao, *Solar RRL* **2019,** *3*, 1800296.

[116] Y. Yan, W.-J. Yin, Y. Wu, T. Shi, N. R. Paudel, C. Li, J. Poplawsky, Z. Wang, J. Moseley, H. Guthrey, H. Moutinho, S. J. Pennycook, M. M. Al-Jassim, *J. Appl. Phys.* **2015,** *117*, 112807.

[117] (a) A. P. Sutton, R. W. Balluff, *Interfaces in crystalline materials*. Clarendon Oxford, Oxford: 1995; (b) P. Lejcek, *Grain Boundary Segregation in Metals*. Springer-Verlag Berlin Heidelberg, Berlin: 2010; (c) H. Ogawa, *Mater. Trans.* **2006,** *47*, 2706; (d) M. D. Sangid, H. Sehitoglu, H. J. Maier, T. Niendorf, *Materials Science and Engineering: A* **2010,** *527*, 7115.

[118] F. Zhu, L. Men, Y. Guo, Q. Zhu, U. Bhattacharjee, P. M. Goodwin, J. W. Petrich, E. A. Smith, J. Vela, *ACS Nano* **2015,** *9*, 2948.

[119] (a) W.-J. Yin, T. Shi, Y. Yan, *J. Phys. Chem. C* **2015,** *119*, 5253; (b) M. Imaeda, T. Mizoguchi, Y. Sato, H. S. Lee, S. D. Findlay, N. Shibata, T. Yamamoto, Y. Ikuhara, *Physical Review B* **2008,** *78*, 245320.

[120] (a) Y. Yu, D. Zhang, C. Kisielowski, L. Dou, N. Kornienko, Y. Bekenstein, A. B. Wong, A. P. Alivisatos, P. Yang, *Nano Lett.* **2016,** *16*, 7530; (b) Y. Yu, D. Zhang, P. Yang, *Nano Lett.* **2017,** *17*, 5489.

[121] Y. Guo, Q. Wang, W. A. Saidi, *J. Phys. Chem. C* **2017,** *121*, 1715.

[122] J. Xu, J.-B. Liu, B.-X. Liu, J. Wang, B. Huang, *Adv. Funct. Mater.* **2019,** *29*, 1805870.

[123] W.-J. Yin, Y. Wu, S.-H. Wei, R. Noufi, M. M. Al-Jassim, Y. Yan, *Adv. Energy Mater.* **2014,** *4*, 1300712.

[124] (a) B. S. Tosun, H. W. Hillhouse, *J. Phys. Chem. Lett.* **2015,** *6*, 2503; (b) B. R. Sutherland, *Joule* **2018,** *2*, 820; (c) S. Sidhik, A. C. Pasarán, C. Rosiles Pérez, T. López-Luke, E. De la Rosa, *J. Mater. Chem. C* **2018,** *6*, 7880.

[125] R. Long, J. Liu, O. V. Prezhdo, *J. Am. Chem. Soc.* **2016,** *138*, 3884.

[126] (a) D.-Y. Son, S.-G. Kim, J.-Y. Seo, S.-H. Lee, H. Shin, D. Lee, N.-G. Park, *J. Am. Chem. Soc.* **2018,** *140*, 1358; (b) X. Gong, L. Guan, H. Pan, Q. Sun, X. Zhao, H. Li, H. Pan, Y. Shen, Y. Shao, L. Sun, Z. Cui, L. Ding, M. Wang, *Adv. Funct. Mater.* **2018,** *28*, 1804286; (c) J. T.-W. Wang, Z. Wang, S. Pathak, W. Zhang, D. W. deQuilettes, F. Wisnivesky-Rocca-Rivarola, J. Huang, P. K. Nayak, J. B. Patel, H. A. Mohd Yusof, Y. Vaynzof, R. Zhu, I. Ramirez, J. Zhang, C. Ducati, C. Grovenor, M. B. Johnston, D. S. Ginger, R. J. Nicholas, H. J. Snaith, *Energy & Environmental Science* **2016,** *9*, 2892; (d) T. Wu, Y. Wang, X. Li, Y. Wu, X. Meng, D. Cui, X. Yang, L. Han, *Adv. Energy Mater.* **2019,** *9*, 1803766.

[127] H. Tan, F. Che, M. Wei, Y. Zhao, M. I. Saidaminov, P. Todorović, D. Broberg, G. Walters, F. Tan, T. Zhuang, B. Sun, Z. Liang, H. Yuan, E. Fron, J. Kim, Z. Yang, O. Voznyy, M. Asta, E. H. Sargent, *Nat. Commun.* **2018,** *9*, 3100.

[128] C. Liu, Z. Huang, X. Hu, X. Meng, L. Huang, J. Xiong, L. Tan, Y. Chen, *ACS Appl. Mater. Interfaces* **2018,** *10*, 1909.

[129] E. Mosconi, D. Meggiolaro, H. J. Snaith, S. D. Stranks, F. De Angelis, *Energy Environ. Sci.* **2016,** *9*, 3180.

[130] H. Tsai, R. Asadpour, J.-C. Blancon, C. C. Stoumpos, O. Durand, J. W. Strzalka, B. Chen, R. Verduzco, P. M. Ajayan, S. Tretiak, J. Even, M. A. Alam, M. G. Kanatzidis, W. Nie, A. D. Mohite, *Science* **2018,** *360*, 67.

[131] W. Nie, J.-C. Blancon, A. J. Neukirch, K. Appavoo, H. Tsai, M. Chhowalla, M. A. Alam, M. Y. Sfeir, C. Katan, J. Even, S. Tretiak, J. J. Crochet, G. Gupta, A. D. Mohite, *Nat. Commun.* **2016,** *7*, 11574.

[132] Q. Wang, B. Chen, Y. Liu, Y. Deng, Y. Bai, Q. Dong, J. Huang, *Energy Environ. Sci.* **2017,** *10*, 516.

[133] Y. Shao, Z. Xiao, C. Bi, Y. Yuan, J. Huang, *Nat. Commun.* **2014,** *5*, 5784.

[134] F. Cai, L. Yang, Y. Yan, J. Zhang, F. Qin, D. Liu, Y.-B. Cheng, Y. Zhou, T. Wang, *J. Mater. Chem. A* **2017,** *5*, 9402.

[135] Y. Lin, L. Shen, J. Dai, Y. Deng, Y. Wu, Y. Bai, X. Zheng, J. Wang, Y. Fang, H. Wei, W. Ma, X. C. Zeng, X. Zhan, J. Huang, *Adv. Mater.* **2017,** *29*, 1604545.

[136] X. Zheng, B. Chen, J. Dai, Y. Fang, Y. Bai, Y. Lin, H. Wei, Xiao C. Zeng, J. Huang, *Nature Energy* **2017,** *2*, 17102.

[137] W. Li, W. Zhang, S. Van Reenen, R. J. Sutton, J. Fan, A. A. Haghighirad, M. B. Johnston, L. Wang, H. J. Snaith, *Energy Environ. Sci.* **2016,** *9*, 490.

[138] W. Ke, G. Fang, Q. Liu, L. Xiong, P. Qin, H. Tao, J. Wang, H. Lei, B. Li, J. Wan, G. Yang, Y. Yan, *J. Am. Chem. Soc.* **2015,** *137*, 6730.

[139] J. P. Correa Baena, L. Steier, W. Tress, M. Saliba, S. Neutzner, T. Matsui, F. Giordano, T. J. Jacobsson, A. R. Srimath Kandada, S. M. Zakeeruddin, A. Petrozza, A. Abate, M. K. Nazeeruddin, M. Grätzel, A. Hagfeldt, *Energy Environ. Sci.* **2015,** *8*, 2928.

[140] E. H. Anaraki, A. Kermanpur, L. Steier, K. Domanski, T. Matsui, W. Tress, M. Saliba, A. Abate, M. Grätzel, A. Hagfeldt, J.-P. Correa-Baena, *Energy Environ. Sci.* **2016,** *9*, 3128.

[141] D. Yang, R. Yang, K. Wang, C. Wu, X. Zhu, J. Feng, X. Ren, G. Fang, S. Priya, S. Liu, *Nat. Commun.* **2018,** *9*, 3239.

[142] W. Ke, D. Zhao, C. Xiao, C. Wang, A. J. Cimaroli, C. R. Grice, M. Yang, Z. Li, C.-S. Jiang, M. Al-Jassim, K. Zhu, M. G. Kanatzidis, G. Fang, Y. Yan, *J. Mater. Chem. A* **2016,** *4*, 14276.

[143] K. Liu, S. Chen, J. Wu, H. Zhang, M. Qin, X. Lu, Y. Tu, Q. Meng, X. Zhan, *Energy Environ. Sci.* **2018,** *11*, 3463.

[144] Z. Liu, K. Deng, J. Hu, L. Li, *Angew. Chem. Int. Ed.* **2019,** *58*, 11497.

[145] Y. Zhao, W. Zhou, W. Ma, S. Meng, H. Li, J. Wei, R. Fu, K. Liu, D. Yu, Q. Zhao, *ACS Energy Lett.* **2016,** *1*, 266.

[146] F. Wang, A. Shimazaki, F. Yang, K. Kanahashi, K. Matsuki, Y. Miyauchi, T. Takenobu, A. Wakamiya, Y. Murata, K. Matsuda, *J. Phys. Chem. C* **2017,** *121*, 1562.

[147] G. Han, T. M. Koh, S. S. Lim, T. W. Goh, X. Guo, S. W. Leow, R. Begum, T. C. Sum, N. Mathews, S. Mhaisalkar, *ACS Appl. Mater. Interfaces* **2017,** *9*, 21292.

[148] D. Koushik, W. J. H. Verhees, Y. Kuang, S. Veenstra, D. Zhang, M. A. Verheijen, M. Creatore, R. E. I. Schropp, *Energy Environ. Sci.* **2017,** *10*, 91.

[149] (a) P. Chen, Y. Bai, S. Wang, M. Lyu, J.-H. Yun, L. Wang, *Adv. Funct. Mater.* **2018,** *28*, 1706923; (b) K. T. Cho, G. Grancini, Y. Lee, E. Oveisi, J. Ryu, O. Almora, M. Tschumi, P. A. Schouwink, G. Seo, S. Heo, J. Park, J. Jang, S. Paek, G. Garcia-Belmonte, M. K. Nazeeruddin, *Energy Environ. Sci.* **2018,** *11*, 952.

[150] Y. Lin, Y. Bai, Y. Fang, Z. Chen, S. Yang, X. Zheng, S. Tang, Y. Liu, J. Zhao, J. Huang, *J. Phys. Chem. Lett.* **2018,** *9*, 654.

[151] S. Gharibzadeh, B. Abdollahi Nejand, M. Jakoby, T. Abzieher, D. Hauschild, S. Moghadamzadeh, J. A. Schwenzer, P. Brenner, R. Schmager, A. A. Haghighirad, L. Weinhardt, U. Lemmer, B. S. Richards, I. A. Howard, U. W. Paetzold, *Adv. Energy Mater.* **2019,** *9*, 1803699.

[152] J. Peng, J. I. Khan, W. Liu, E. Ugur, T. Duong, Y. Wu, H. Shen, K. Wang, H. Dang, E. Aydin, X. Yang, Y. Wan, K. J. Weber, K. R. Catchpole, F. Laquai, S. De Wolf, T. P. White, *Adv. Energy Mater.* **2018,** *8*, 1801208.

[153] A. Dualeh, N. Tétreault, T. Moehl, P. Gao, M. K. Nazeeruddin, M. Grätzel, *Adv. Funct. Mater.* **2014,** *24*, 3250.

[154] Z. Xiao, Q. Dong, C. Bi, Y. Shao, Y. Yuan, J. Huang, *Adv. Mater.* **2014,** *26*, 6503.

[155] J. Liu, C. Gao, X. He, Q. Ye, L. Ouyang, D. Zhuang, C. Liao, J. Mei, W. Lau, *ACS Appl. Mater. Interfaces* **2015,** *7*, 24008.

[156] W. Nie, H. Tsai, R. Asadpour, J.-C. Blancon, A. J. Neukirch, G. Gupta, J. J. Crochet, M. Chhowalla, S. Tretiak, M. A. Alam, H.-L. Wang, A. D. Mohite, *Science* **2015,** *347*, 522.

[157] S. M. Jain, Z. Qiu, L. Häggman, M. Mirmohades, M. B. Johansson, T. Edvinsson, G. Boschloo, *Energy Environ. Sci.* **2016,** *9*, 3770.

[158] Q. Wang, Y. Shao, Q. Dong, Z. Xiao, Y. Yuan, J. Huang, *Energy Environ. Sci.* **2014,** *7*, 2359.

[159] (a) W. Zhang, S. Pathak, N. Sakai, T. Stergiopoulos, P. K. Nayak, N. K. Noel, A. A. Haghighirad, V. M. Burlakov, D. W. deQuilettes, A. Sadhanala, W. Li, L. Wang, D. S. Ginger, R. H. Friend, H. J. Snaith, *Nat. Commun.* **2015,** *6*, 10030; (b) H. Jiang, Z. Yan, H. Zhao, S. Yuan, Z. Yang, J. Li, B. Liu, T. Niu, J. Feng, Q. Wang, D. Wang, H. Yang, Z. Liu, S. F. Liu, *ACS Appl. Energy Mater.* **2018,** *1*, 900.

[160] N. De Marco, H. Zhou, Q. Chen, P. Sun, Z. Liu, L. Meng, E.-P. Yao, Y. Liu, A. Schiffer, Y. Yang, *Nano Lett.* **2016,** *16*, 1009.

[161] X. Li, W. Zhang, W. Zhang, H.-Q. Wang, J. Fang, *Nano Energy* **2019,** *58*, 825.

[162] P. Guo, Q. Ye, X. Yang, J. Zhang, F. Xu, D. Shchukin, B. Wei, H. Wang, *J. Mater. Chem. A* **2019,** *7*, 2497.

[163] T. Niu, J. Lu, R. Munir, J. Li, D. Barrit, X. Zhang, H. Hu, Z. Yang, A. Amassian, K. Zhao, S. Liu, *Adv. Mater.* **2018,** *30*, 1706576.

[164] J. Xu, A. Buin, A. H. Ip, W. Li, O. Voznyy, R. Comin, M. Yuan, S. Jeon, Z. Ning, J. J. McDowell, P. Kanjanaboos, J.-P. Sun, X. Lan, L. N. Quan, D. H. Kim, I. G. Hill, P. Maksymovych, E. H. Sargent, *Nat. Commun.* **2015,** *6*, 7081.

[165] W. Li, S. K. Yadavalli, D. Lizarazo-Ferro, M. Chen, Y. Zhou, N. P. Padture, R. Zia, *ACS Energy Lett.* **2018,** *3*, 2669.

[166] (a) Y. B. Qi, *Surf. Sci. Rep.* **2011,** *66*, 379; (b) E. M. Tennyson, J. M. Howard, M. S. Leite, *ACS Energy Lett.* **2017,** *2*, 1825; (c) R. Giridharagopal, P. A. Cox, D. S. Ginger, *Acc. Chem. Res.* **2016,** *49*, 1769.

[167] D. H. Kim, J. Park, Z. Li, M. Yang, J.-S. Park, I. J. Park, J. Y. Kim, J. J. Berry, G. Rumbles, K. Zhu, *Adv. Mater.* **2017,** *29*, 1606831.

[168] L. K. Ono, Y. B. Qi, S. F. Liu, *Joule* **2018,** *2*, 1961.

[169] H. J. Snaith, A. Abate, J. M. Ball, G. E. Eperon, T. Leijtens, N. K. Noel, S. D. Stranks, J. T.-W. Wang, K. Wojciechowski, W. Zhang, *J. Phys. Chem. Lett.* **2014,** *5*, 1511.

[170] (a) L. Collins, M. Ahmadi, T. Wu, B. Hu, S. V. Kalinin, S. Jesse, *ACS Nano* **2017,** *11*, 8717; (b) Y. Almadori, D. Moerman, J. L. Martinez, P. Leclère, B. Grévin, *Beilstein J. Nanotechnol.* **2018,** *9*, 1695.

[171] H. Tian, L. Zhao, X. Wang, Y.-W. Yeh, N. Yao, B. P. Rand, T.-L. Ren, *ACS Nano* **2017,** *11*, 12247.

[172] (a) S. Silver, Q. Dai, H. Li, J.-L. Brédas, A. Kahn, *Adv. Energy Mater. 0*, 1901005; (b) R. Giridharagopal, J. T. Precht, S. Jariwala, L. Collins, S. Jesse, S. V. Kalinin, D. S. Ginger, *ACS Nano* **2019,** *13*, 2812.

[173] Y. Zhou, C. Fuentes-Hernandez, J. Shim, J. Meyer, A. J. Giordano, H. Li, P. Winget, T. Papadopoulos, H. Cheun, J. Kim, M. Fenoll, A. Dindar, W. Haske, E. Najafabadi, T. M. Khan, H. Sojoudi, S. Barlow, S. Graham, J.-L. Brédas, S. R. Marder, A. Kahn, B. Kippelen, *Science* **2012,** *336*, 327.

[174] (a) D. I. Patel, S. Bahr, P. Dietrich, M. Meyer, A. Thißen, M. R. Linford, *Surface Science Spectra* **2019,** *26*, 024002; (b) J. Chun-Ren Ke, A. S. Walton, D. J. Lewis, A. Tedstone, P. O'Brien, A. G. Thomas, W. R. Flavell, *Chemical Communications* **2017,** *53*, 5231; (c) J. Lin, M. Lai, L. Dou, C. S. Kley, H. Chen, F. Peng, J. Sun, D. Lu, S. A. Hawks, C. Xie, F. Cui, A. P. Alivisatos, D. T. Limmer, P. Yang, *Nat. Mater.* **2018,** *17*, 261; (d) J. C.-R. Ke, D. J. Lewis, A. S. Walton, B. F. Spencer, P. O'Brien, A. G. Thomas, W. R. Flavell, *J. Mater. Chem. A* **2018,** *6*, 11205.

[175] (a) K. Motoki, Y. Miyazawa, D. Kobayashi, M. Ikegami, T. Miyasaka, T. Yamamoto, K. Hirose, *J. Appl. Phys.* **2017,** *121*, 085501; (b) B.-A. Chen, J.-T. Lin, N.-T. Suen, C.-W. Tsao, T.-C. Chu, Y.-Y. Hsu, T.-S. Chan, Y.-T. Chan, J.-S. Yang, C.-W. Chiu, H. M. Chen, *ACS Energy Lett.* **2017,** *2*, 342.

[176] (a) L. T. Schelhas, J. A. Christians, J. J. Berry, M. F. Toney, C. J. Tassone, J. M. Luther, K. H. Stone, *ACS Energy Lett.* **2016,** *1*, 1007; (b) M. Alsari, O. Bikondoa, J. Bishop, M. Abdi-Jalebi, L. Y. Ozer, M. Hampton, P. Thompson, M. T. Hörantner, S. Mahesh, C. Greenland, J. E. Macdonald, G. Palmisano, H. J. Snaith, D. G. Lidzey, S. D. Stranks, R. H. Friend, S. Lilliu, *Energy Environ. Sci.* **2018,** *11*, 383.

[177] (a) L. K. Ono, T. Kim, Y. Jiang, Y. B. Qi, S. F. Liu, *ACS Energy Lett.* **2018,** *3*, 1898; (b) L. K. Ono, N.-G. Park, K. Zhu, W. Huang, Y. B. Qi, *ACS Energy Lett.* **2017,** *2*, 1749; (c) L. Qiu, S. He, L. K. Ono, S. Liu, Y. B. Qi, *ACS Energy Lett.* **2019**, DOI: 10.1021/acsenergylett.9b01396.

[178] M. A. Green, E. D. Dunlop, D. H. Levi, J. Hohl-Ebinger, M. Yoshita, A. W. Y. Ho-Baillie, *Prog. Photovolt. Res. Appl.* **2019,** *27*, 565.

[179] (a) H. S. Kim, C. R. Lee, J. H. Im, K. B. Lee, T. Moehl, A. Marchioro, S. J. Moon, R. Humphry-Baker, J. H. Yum, J. E. Moser, M. Grätzel, N. G. Park, *Sci. Rep.* **2012,** *2*, 591; (b) Z. Hawash, L. K. Ono, Y. B. Qi, *Adv. Mater. Interfaces* **2018,** *5*, 1700623; (c) L. K. Ono, Z. Hawash, E. J. Juarez-Perez, L. B. Qiu, Y. Jiang, Y. B. Qi, *J Phys D Appl Phys* **2018,** *51*.

[180] L. Han, *Nature* **2019,** *567*, 465.

[181] A. Kojima, K. Teshima, Y. Shirai, T. Miyasaka, *J. Am. Chem. Soc.* **2009,** *131*, 6050.

[182] J.-H. Im, C.-R. Lee, J.-W. Lee, S.-W. Park, N.-G. Park, *Nanoscale* **2011,** *3*, 4088.

[183] J. Burschka, N. Pellet, S. J. Moon, R. Humphry-Baker, P. Gao, M. K. Nazeeruddin, M. Grätzel, *Nature* **2013,** *499*, 316.

[184] N. J. Jeon, J. H. Noh, Y. C. Kim, W. S. Yang, S. Ryu, S. I. Seok, *Nat Mater* **2014,** *13*, 897.

[185] N. J. Jeon, J. H. Noh, W. S. Yang, Y. C. Kim, S. Ryu, J. Seo, S. I. Seok, *Nature* **2015,** *517*, 476.

[186] W. S. Yang, J. H. Noh, N. J. Jeon, Y. C. Kim, S. Ryu, J. Seo, S. I. Seok, *Science* **2015,** *348*, 1234.

[187] D. Bi, C. Yi, J. Luo, J.-D. Décoppet, F. Zhang, Shaik M. Zakeeruddin, X. Li, A. Hagfeldt, M. Grätzel, *Nat. Energy* **2016,** *1*, 16142.

[188] M. Saliba, T. Matsui, J.-Y. Seo, K. Domanski, J.-P. Correa-Baena, M. K. Nazeeruddin, S. M. Zakeeruddin, W. Tress, A. Abate, A. Hagfeldt, M. Gratzel, *Energy Environ. Sci.* **2016,** *9*, 1989.

[189] Q. Jiang, Y. Zhao, X. Zhang, X. Yang, Y. Chen, Z. Chu, Q. Ye, X. Li, Z. Yin, J. You, *Nat. Photon.* **2019**, DOI: 10.1038/s41566.

[190] (a) Y. Y. Zhou, M. J. Yang, W. W. Wu, A. L. Vasiliev, K. Zhu, N. P. Padture, *J. Mater. Chem. A* **2015,** *3*, 8178; (b) M. A. Green, Y. Hishikawa, E. D. Dunlop, D. H. Levi, J. Hohl-Ebinger, M. Yoshita, A. W. Y. Ho-Baillie, *Prog. Photovolt. Res. Appl.* **2019,** *27*, 3.

[191] T. W. Kim, N. Shibayama, L. Cojocaru, S. Uchida, T. Kondo, H. Segawa, *Adv. Funct. Mater.* **2018,** *28*, 1804039.

[192] Y. Luo, P. Khoram, S. Brittman, Z. Zhu, B. Lai, S. P. Ong, E. C. Garnett, D. P. Fenning, *Adv. Mater.* **2017,** *29*, 1703451.

[193] Y. Zhong, R. Munir, J. Li, M.-C. Tang, M. R. Niazi, D.-M. Smilgies, K. Zhao, A. Amassian, *ACS Energy Lett.* **2018,** *3*, 1078.

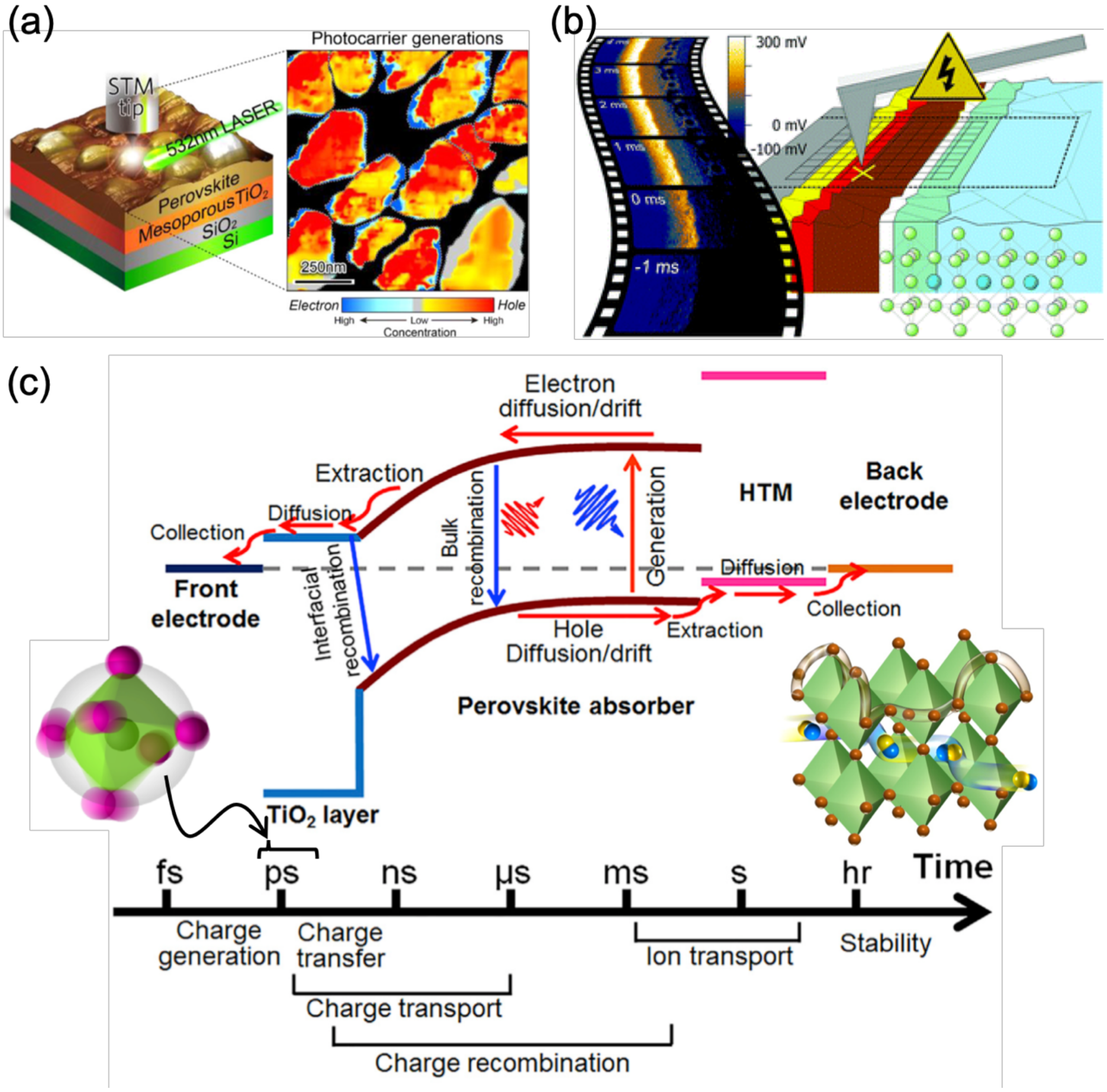

Figure 1. a) Spatially resolved imaging on photoinduced charge transfer behaviors in perovskite grains under light illumination mapped by light-modulated scanning tunneling microscopy. Reprinted with permission from ref. [15]. Copyright 2017, American Chemical Society. b) A method based on Kelvin probe force microscopy that enables mapping of charge redistribution in an operating device upon a voltage- or light pulse with sub-millisecond resolution was developed. Reprinted with permission from ref. [12c]. Copyright 2018, The Royal Society of Chemistry. c) Possible charge excitation, recombination, transport, and extraction at electrodes processes and the corresponding time-scale taking place in PSCs. Reprinted with permission from ref. [9a]. Copyright 2018, Elsevier Ltd. The picture in the left side as inset (octahedron dynamics in ps time scale) in panel c) was reprinted with permission from ref. [29a]. The picture in the right side as inset (ion migration in ms to s time scale) was reprinted with permission from ref. [10g]. Copyright 2016, The Royal Society of Chemistry.

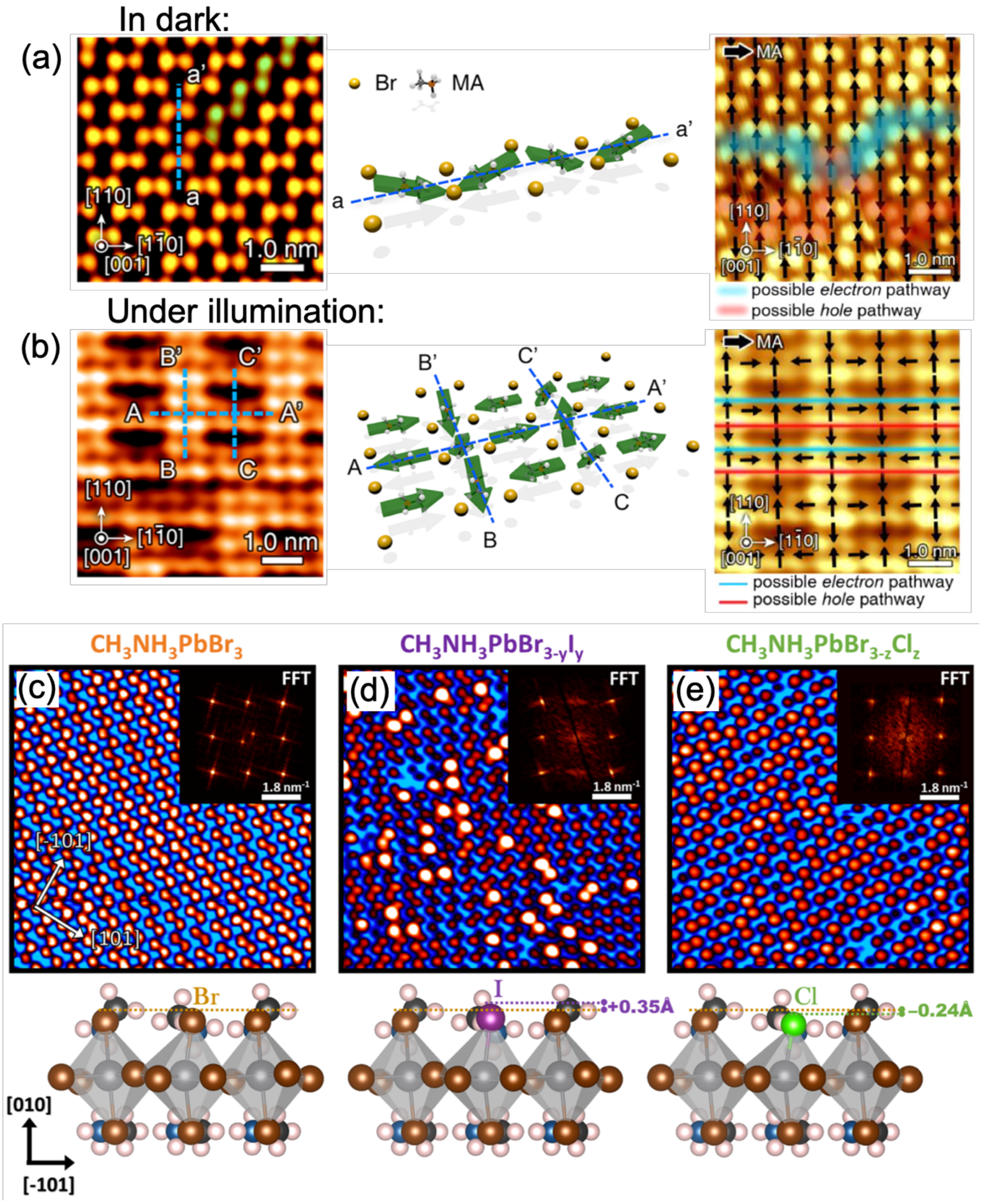

Figure 2. a) Comparison of the surface structure and molecule orientation pattern in the dark and b) under illumination. STM images reveal a transition from a) the dominant dimer structure in dark to b) a 4 × 2 structure under laser illumination. DFT calculations reveal $CH_3NH_3^+$ molecule dipole alignments lead to the transition from a) to b) surface pattern under illumination. The orientation of $CH_3NH_3^+$ molecule dipoles are indicated by arrows. The blue lines indicate a low electron potential energy pathway and the red ones indicate a low hole potential energy pathway. The fading out illustrates the lack of potential modulation in the 2 × 2 phase in dark.

A movie showing the proposed model of MA rotation and its influence on Br surface arrangement is available as supplementary work in this work. Reprinted with permission from ref. [26]. Copyright 2019, American Chemical Society. c-e) Large area STM images (10 nm × 10 nm) of the c) pristine $CH_3NH_3PbBr_3$, d) $CH_3NH_3PbBr_{3-y}I_y$, and e) $CH_3NH_3PbBr_{3-z}Cl_z$ mixed-halide perovskites. Inset: FFT results obtained from the topographic STM images showing no additional peak at low k-values for the mixed-halide perovskite, suggesting that there is no long-range ordering of the additional iodine and chlorine ions at the surface. Relative positions of the I (+0.35 Å) and Cl (−0.24 Å) ions with respect to the top $CH_3NH_3Br_3$ structure. Color code: Pb (gray), Br (brown), I (purple), Cl (green), C (black), N (blue), H (light pink). Reprinted with permission from ref. [27]. Copyright 2019, American Chemical Society.

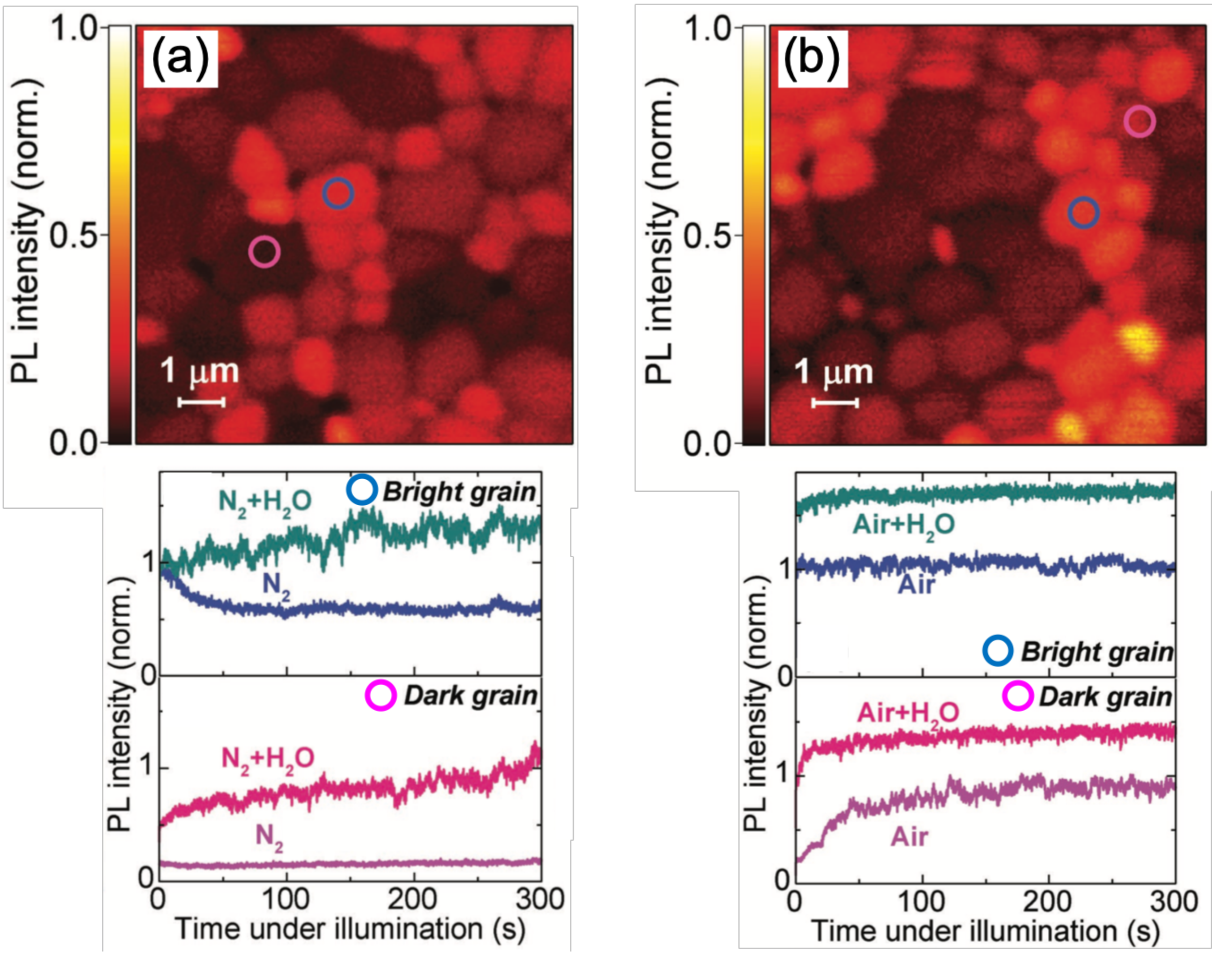

Figure 3. Microscale confocal PL map of a $MAPbI_3$ perovskite film in a) dry nitrogen, and humidified nitrogen (~45% RH), b) dry air, and humidified air (~45% RH) normalized to the maximum intensity. PL intensity as a function of time under illumination from a bright grain (blue circle) and a dark grain (pink circle) under the different gas environment. The PL intensity for each trace over time is given relative to the starting value for the bright grain in nitrogen, which is normalized to 1. Reprinted with permission from ref. [45b]. Copyright 2018, WILEY-VCH Verlag GmbH & Co. KGaA, Weinheim.

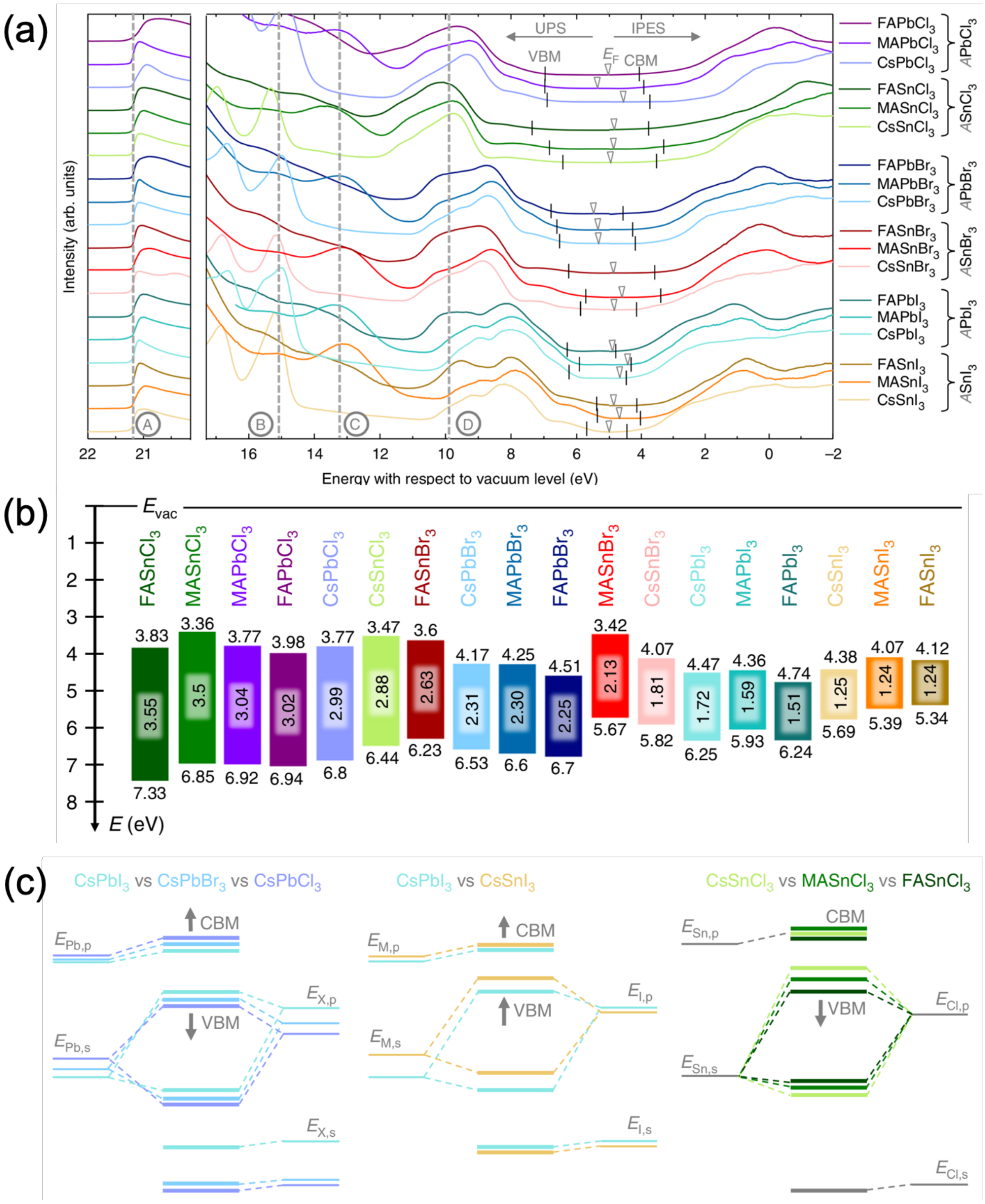

Figure 4. a) UPS and IPES spectra of 18 Sn- and Pb-based halide perovskites. For easy comparison, the secondary electron cutoff (SECO) onsets were aligned at the He-Iα excitation energy (21.22 eV), marked by line A. Lines, B, C, and D indicate the common features corresponding to the Cs, MA, and FA related states, respectively. The extracted absolute positions of IE and EA are indicated by vertical markers, while and E_F is indicated by triangles. b) Diagram of energy levels of the 18 metal halide perovskites with IE, EA, and E_{Opt} values indicated in eV. Minor deviations between E_{Opt} and difference between IE and EA (i.e., E_G) can

be inferred and assigned to contribution of exciton bind energy and/or error measurements. c) Trends of changes in energy levels in ABX_3 perovskites when varying the X halide anions (left panel), M metal cations (middle panel), and A cations (right panel). Arrows indicate the direction of shifts in energy levels upon the anion or cation substitutions. Reprinted with permission from ref. [49c]. Copyright 2019, Springer Nature.

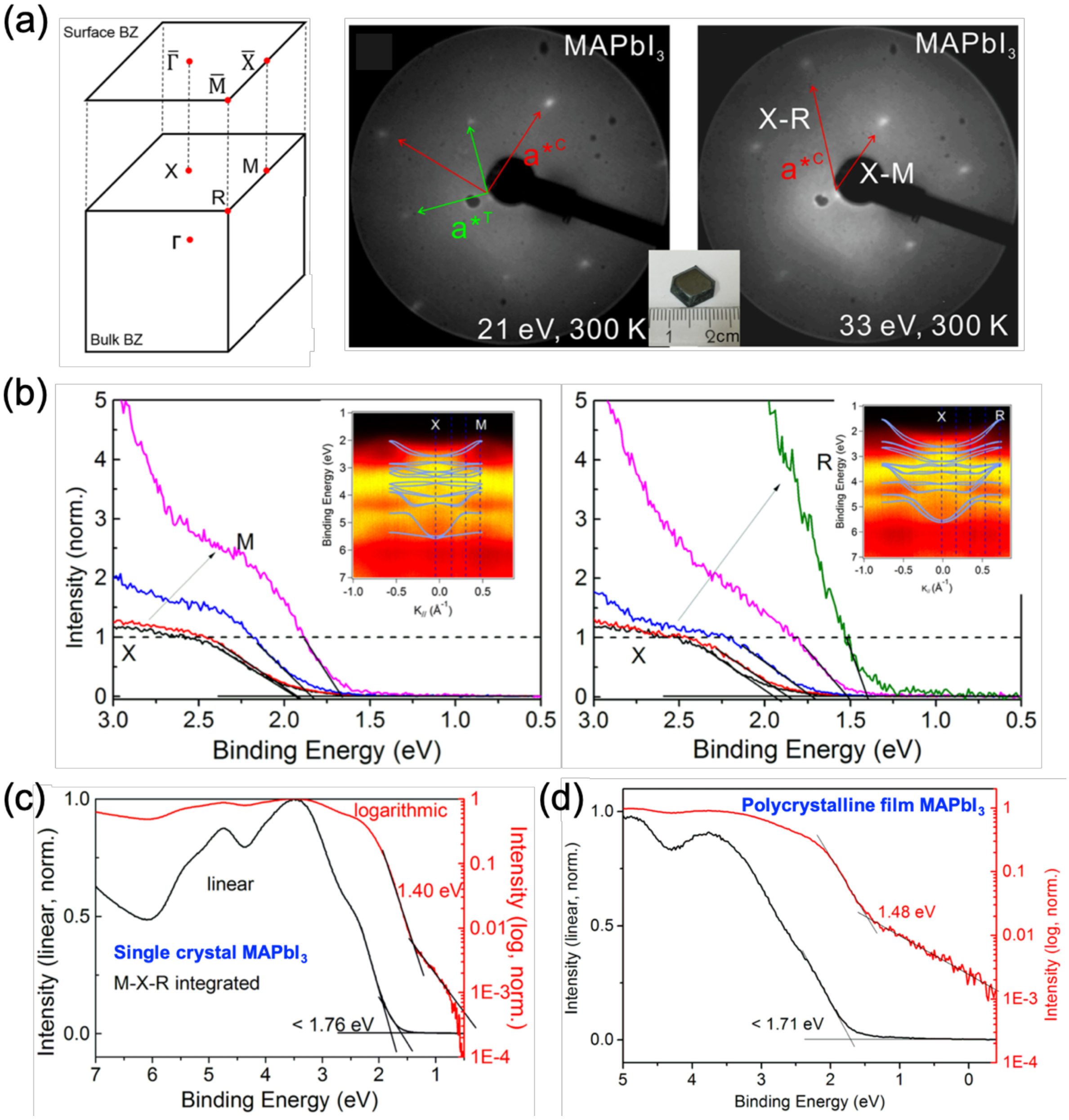

Figure 5. a) Schematic of the surface and first bulk Brillouin zone (BZ) of a cubic lattice. LEED patterns of (001) plane of $MAPbI_3$ single crystal acquired at electron energies of 21 eV and 33 eV at 295 K. The reciprocal lattice parameters a^{*C} and a^{*T} refer to the cubic and tetragonal phases, respectively. b) Photoemission spectra for defined emission angles with selected wave vector (k) values along the X—M and X—R directions. Inset shows the band structure of of $MAPbI_3$ single crystal measured ARPES. c) Integrated photoemission spectra of all k values along the X—M and X—R directions acquired on $MAPbI_3$ single crystal, which translates to a simulated polycrystalline $MAPbI_3$ film. d) Actual UPS measurements on the polycrystalline film of $MAPbI_3$. The photoemission intensities are displayed in linear and logarithmic scales to highlight the variations in the onset of VBM determination. Reprinted with permission from ref. [52]. Copyright 2019, American Chemical Society.

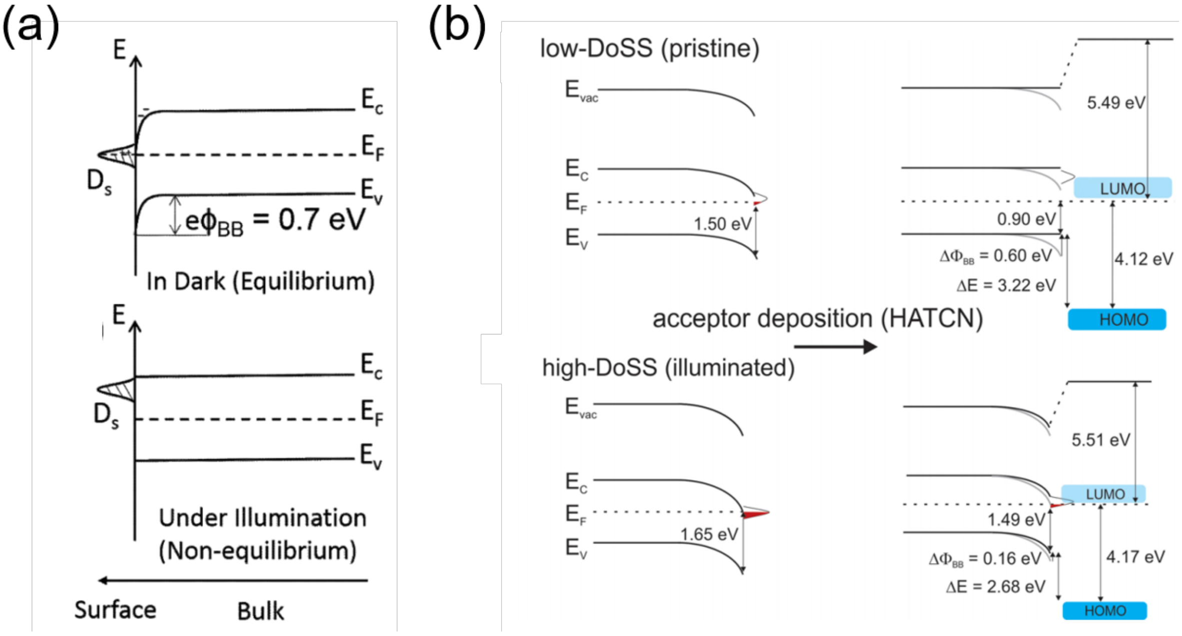

Figure 6. Effect of surface states on the band structure of $MAPbI_3$. a) the surface band bending is caused by the surface trap states with E_F pinned to CBM. Under illumination the traps are filled with photo-excited charges and the flat band structure is formed. Reprinted from ref. [55b] Copyright 2017, WILEY-VCH Verlag GmbH & Co. KGaA, Weinheim. b) the density of surface state influence the energy level alignment with the coating of ETL. Reprinted from ref. [55a]. Copyright 2017, American Chemical Society.

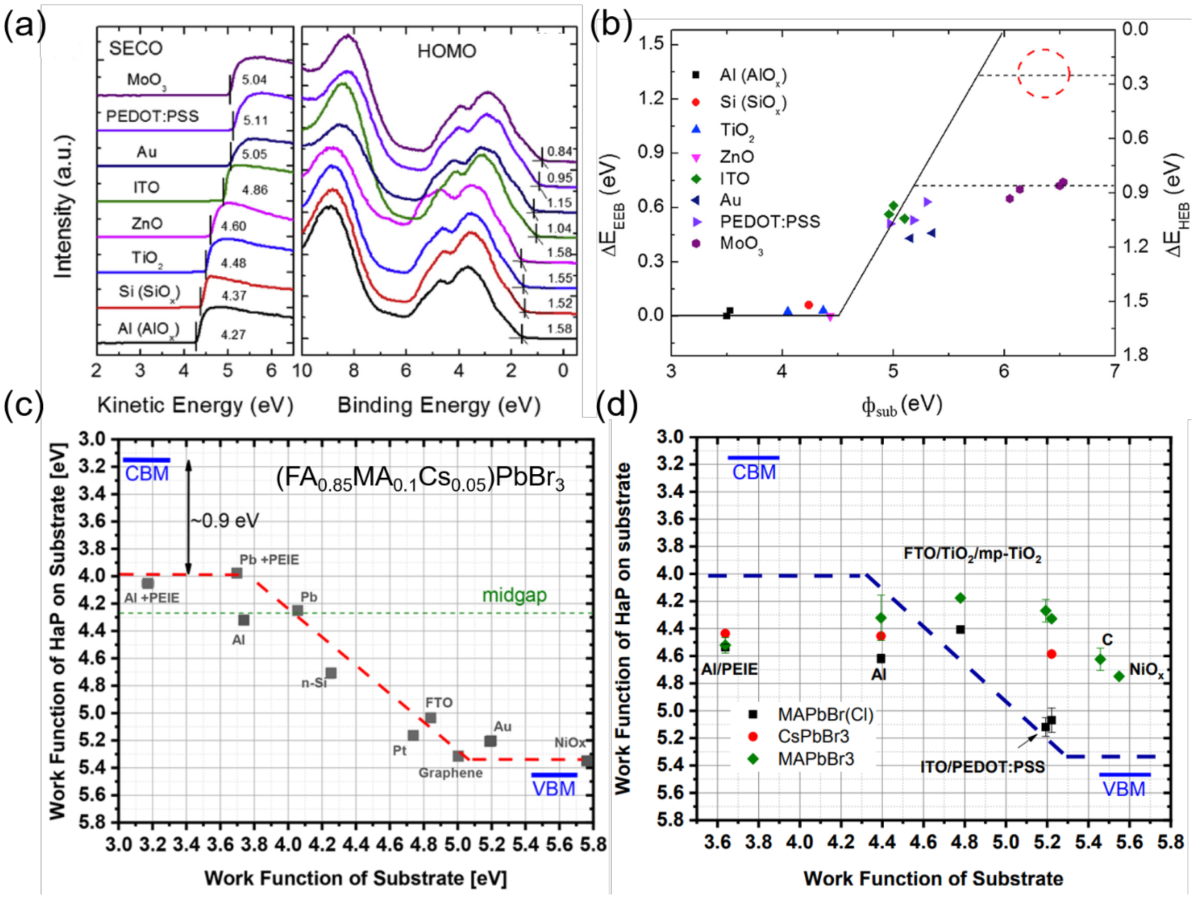

Figure 7. Influence of the underlying substrate on the perovskite electronic properties. a) and b) evaporated $MAPbI_3$ on substrate with increasing WF. The deposited $MAPbI_3$ also shows increased WF and shift of VBM to lower binding energy. Reprinted from ref. [59a]. Copyright 2017, Elsevier Ltd. c) the WF evolution of $(FA_{0.85}MA_{0.1}Cs_{0.05})PbBr_3$ on the substrates with increasing WF. d) the WF evolution of MAPbBr(Cl), $MAPbBr_3$ and $CsPbBr_3$ on the substrates with increasing WF. Reprinted from ref. [67]. Copyright 2019, American Chemical Society.

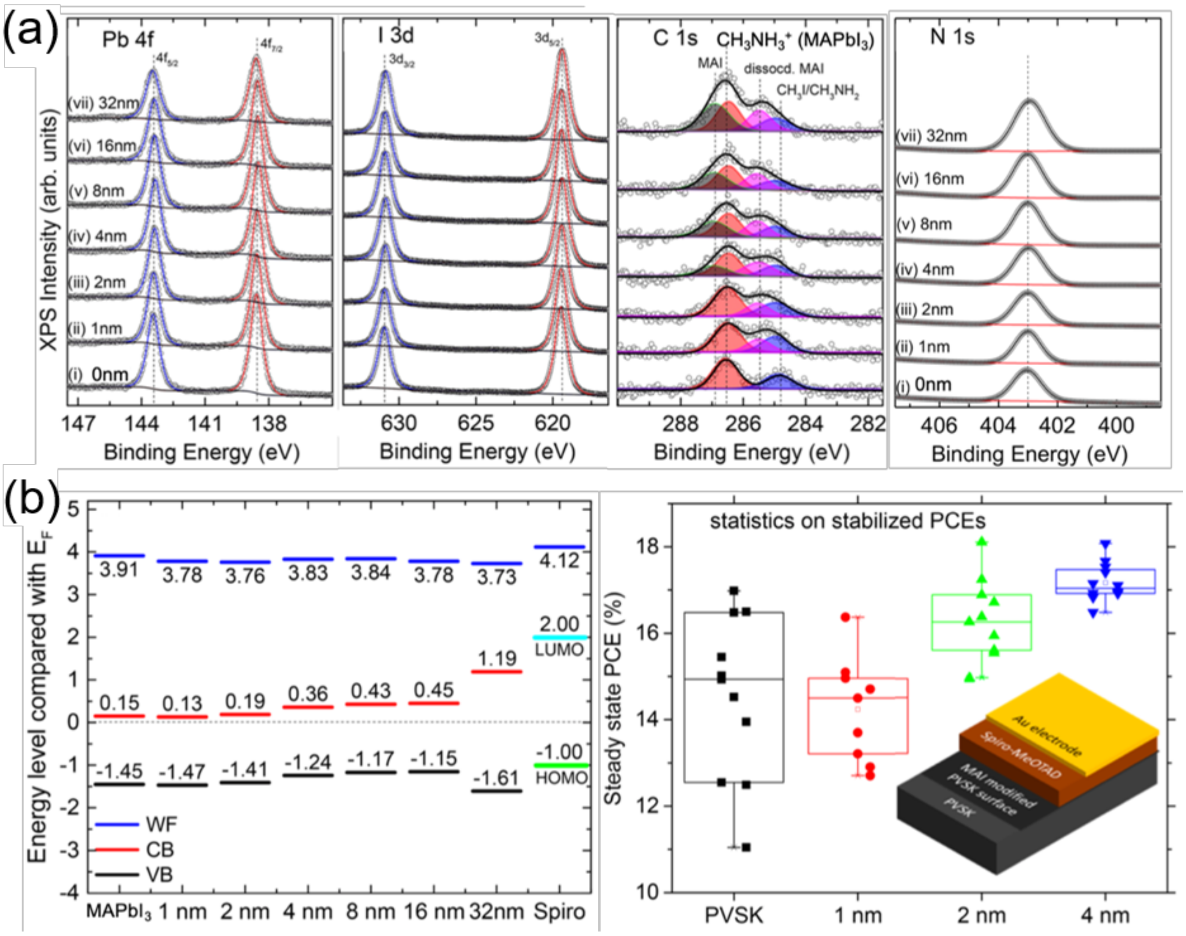

Figure 8. a) XPS spectra (Al-kα = 1486.6 eV) corresponding to Pb 4f, I 3d, C 1s, and N 1s core levels of the pristine $MAPbI_3$ perovskite and after depositing additional excess of MAI layer (from 1 nm up to 32 nm). b) (Left panel) Schematic energy diagram of valence band (VB), conduction band (CB), and work function (WF) with respect to the Fermi level (E_F). (Right panel) Statistics of steady-state PCEs with $MAPbI_3$-based PSCs as a function of excess MAI layer thickness. A schematic of device architecture with interface modification is shown in the inset. Reprinted with permission from ref. [49m]. Copyright 2017, American Chemical Society.

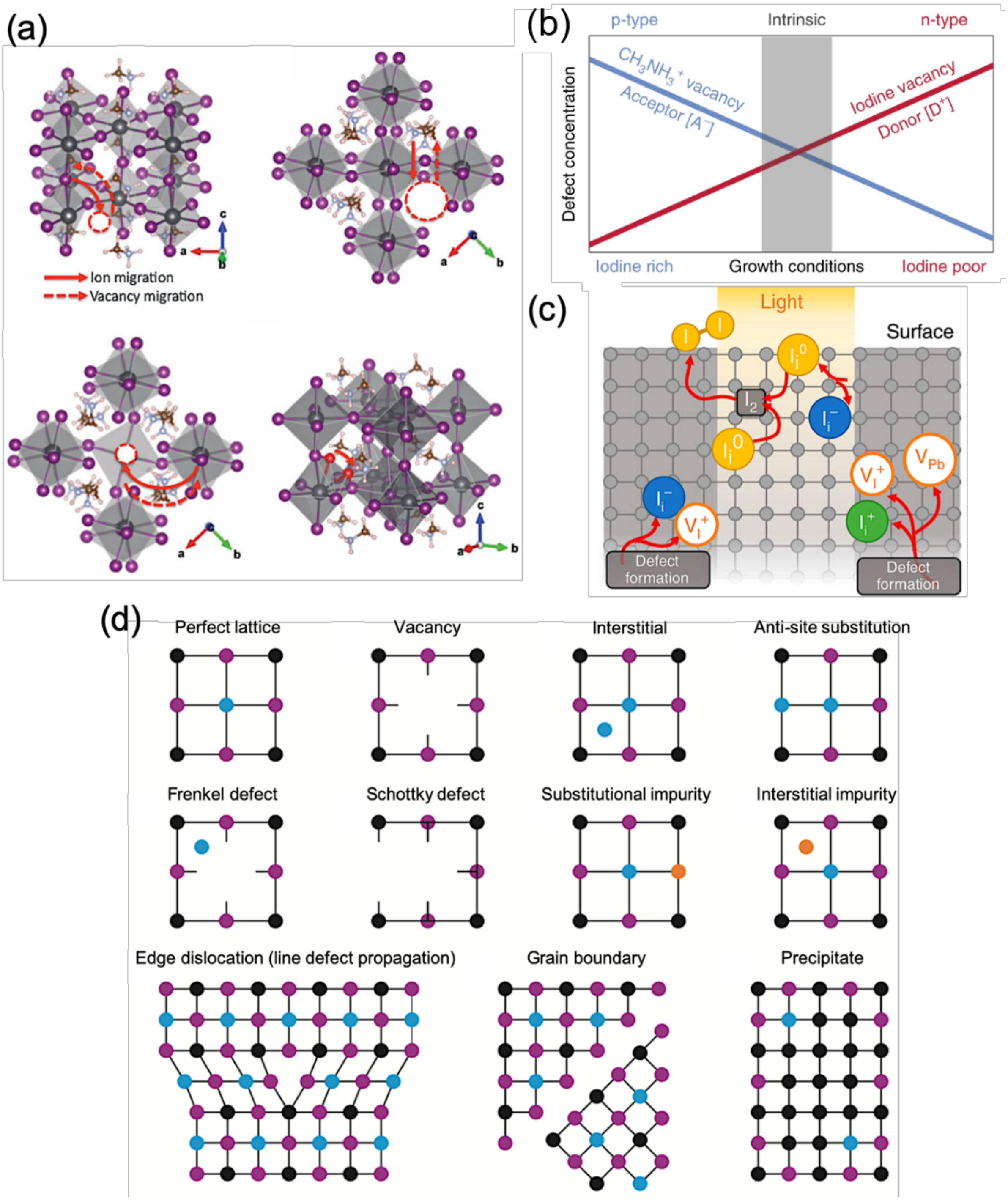

Figure 9. a) Migration pathways for the vacancies of iodine (V_I), methylammonium (V_{MA}), lead (V_{Pb}), and interstitial iodine (I_i) defects. Solid lines represent migration of the ions, while the dashed lines indicate trajectories of the vacancies. Reprinted with permission from ref. [87a]. Copyright 2015, The Royal Society of Chemistry. b) Control of defect concentration in $MAPbI_3$ that can be achieved during crystal growth and annealing. Three regimes in $MAPbI_3$ semiconductor behavior leading to n-type (electron rich), p-type (hole rich), and intrinsic ($[A^+] \sim [D^-]$) characteristics. Reprinted with permission from ref. [88]. Copyright 2019, Springer Nature. c) Dynamics of light-induced degradation in $MAPbI_3$. On the basis of hybrid-DFT,

$MAPbI_3$ shows the defect chemistry dominated by Pb vacancy (V_{Pb}) and interstitial iodide (I_i). Proposal of I_i^+/I_i^- pair defect formation: (i) $MAPbI_3 \rightarrow V_{Pb}^{2-} + V_I^+ + I_i^+$ and (ii) $MAPbI_3 \rightarrow V_I^+ + I_i^-$. Sequential electron and hole trapping take place on the I_i^+/I_i^- pair defect leading to I_2: $I_i^+/I_i^- + 1e \rightarrow I_i^0/I_i^- + 1h \rightarrow 2I_i^0 \rightarrow I_2$. A surface-coordinated I_2 molecule can remain bound to the surface or grain boundary. Reprinted with permission from ref. [89]. Copyright 2019, Springer Nature. d) Illustration of the type of defects in perovskite crystal lattice: blue, black, and purple dots represent A, M, and X site ions, respectively. Orange dots represent impurity atoms. Defects are often divided into two categories of point defects (i.e., vacancy, interstitial, anti-site substitution, Frenkel and Schottky defects, substitutional and interstitial impurities) and dimensional defects (i.e., edge dislocation (line defect propagation), grain boundary, and precipitates). Theoretical studies provide useful but limited guidance as the results are dependent on the choice of modules and calculation methods, especially the dimensional defects, which has a relatively larger model system size and complex environment. Reprinted with permission from ref. [90c]. Copyright 2016, Springer Nature.

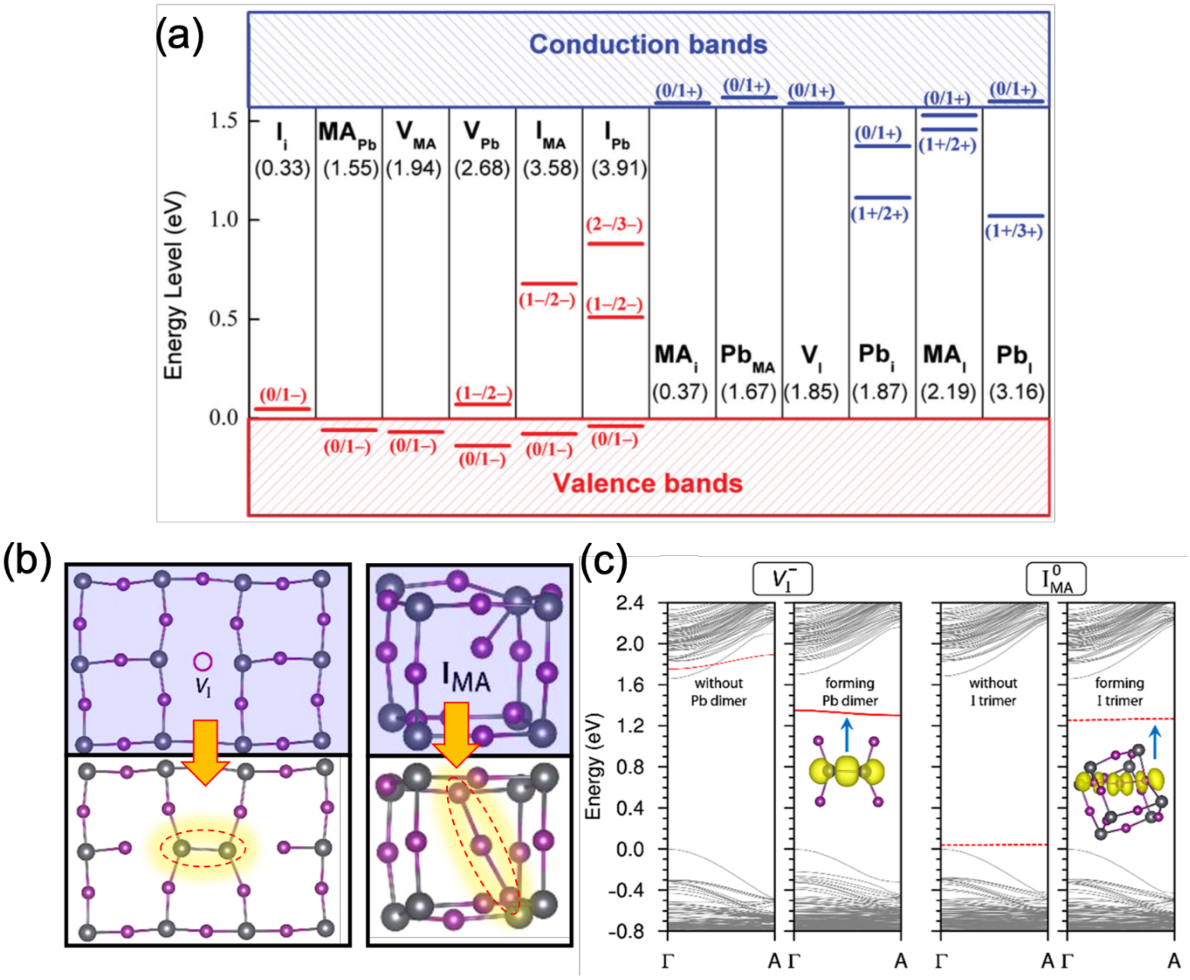

Figure 10. a) Calculated defect energy levels of point defects. The formation energies of defects are indicated by the values within parenthesis. The acceptor (red) type and donor (blue) type of defects are ordered by the formation energies. Reprinted with permission from ref. [76a]. Copyright 2014, WILEY-VCH Verlag GmbH & Co. KGaA, Weinheim. b) Atomic structure changes before (shaded) and after (non-shaded) illustrating the steps for the formation of Pb dimer from V_I and I trimmer from I_{MA}. c) Reprinted with permission from ref. [95]. Copyright 2014, American Chemical Society.

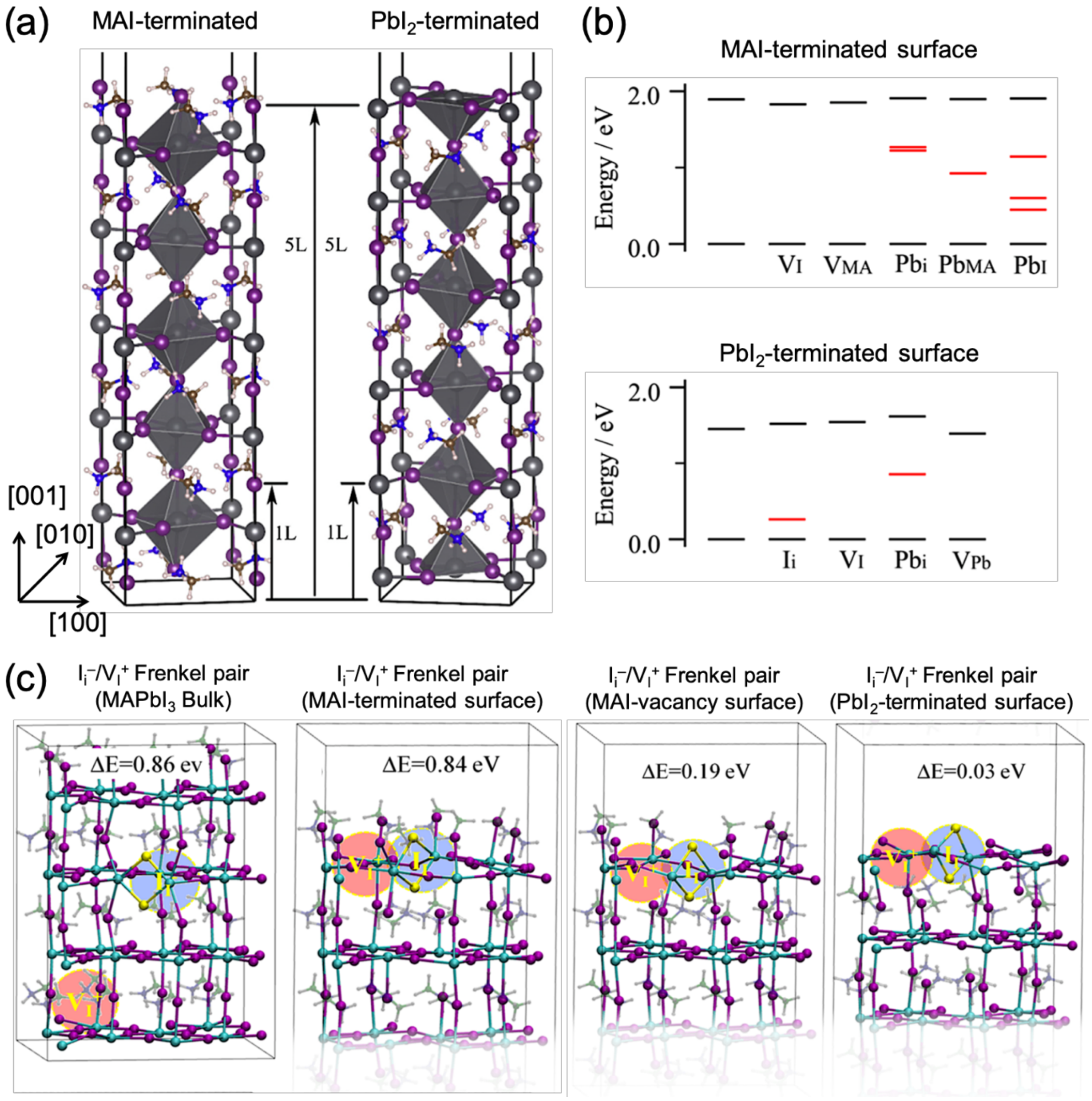

Figure 11. a) DFT optimized geometrical structures of 5-layer slabs with (001) surface of $MAPbI_3$ perovskite including a vacuum layer of 20 Å. Two surface terminations are widely studied: MAI- and PbI_2-terminated surfaces. Reprinted with permission from ref. [102g]. Copyright 2015, Elsevier Ltd. b) VBM, CBM, and point defects energy levels with respect to the VBM (E = 0). Defect levels are represented by red horizontal lines, while the VBM and CBM are represented by the lower and upper black lines, respectively. Reprinted with permission from ref. [102c]. Copyright 2017, American Chemical Society. c) Optimized structures and formation energies for I_i^-/V_I^+ Frenkel pair in the $MAPbI_3$ bulk, at MAI-terminated surface, at a MAI-vacant site, and at PbI_2-terminated surface. Reprinted with permission from ref. [56]. Copyright 2019, American Chemical Society.

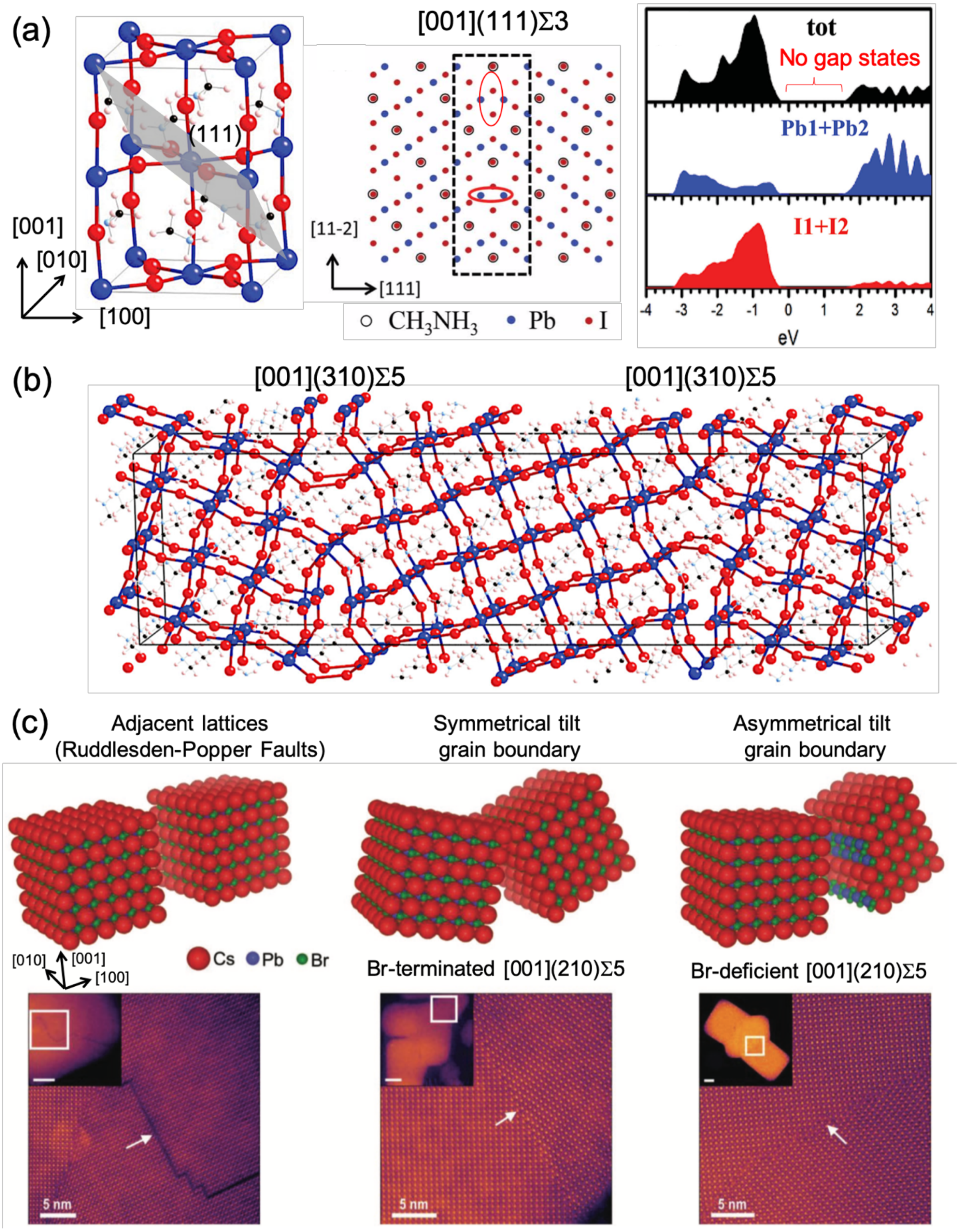

Figure 12. a) Tetragonal $MAPbI_3$ crystal structure phase. Structural model for a [001](111)Σ3 grain boundary in $MAPbI_3$. The red circles indicate the new bonds formed at the grain boundary, which DFT calculations reveal the non-generation of deep level defects. b) Schematic of a super cell structure of [001](310)Σ5 grain boundary. Reprinted with permission from ref. [76b]. Copyright 2015, WILEY-VCH Verlag GmbH & Co. KGaA, Weinheim. c) Schematic

formation of different planar faults of Ruddlesden-Popper (RP), Br-terminated and Br-deficient [001](210)Σ5 during the fusion of $CsPbBr_3$ nanocrystals and their respective HAADF images. Reprinted with permission from ref. [8a]. Copyright 2019, WILEY-VCH Verlag GmbH & Co. KGaA, Weinheim.

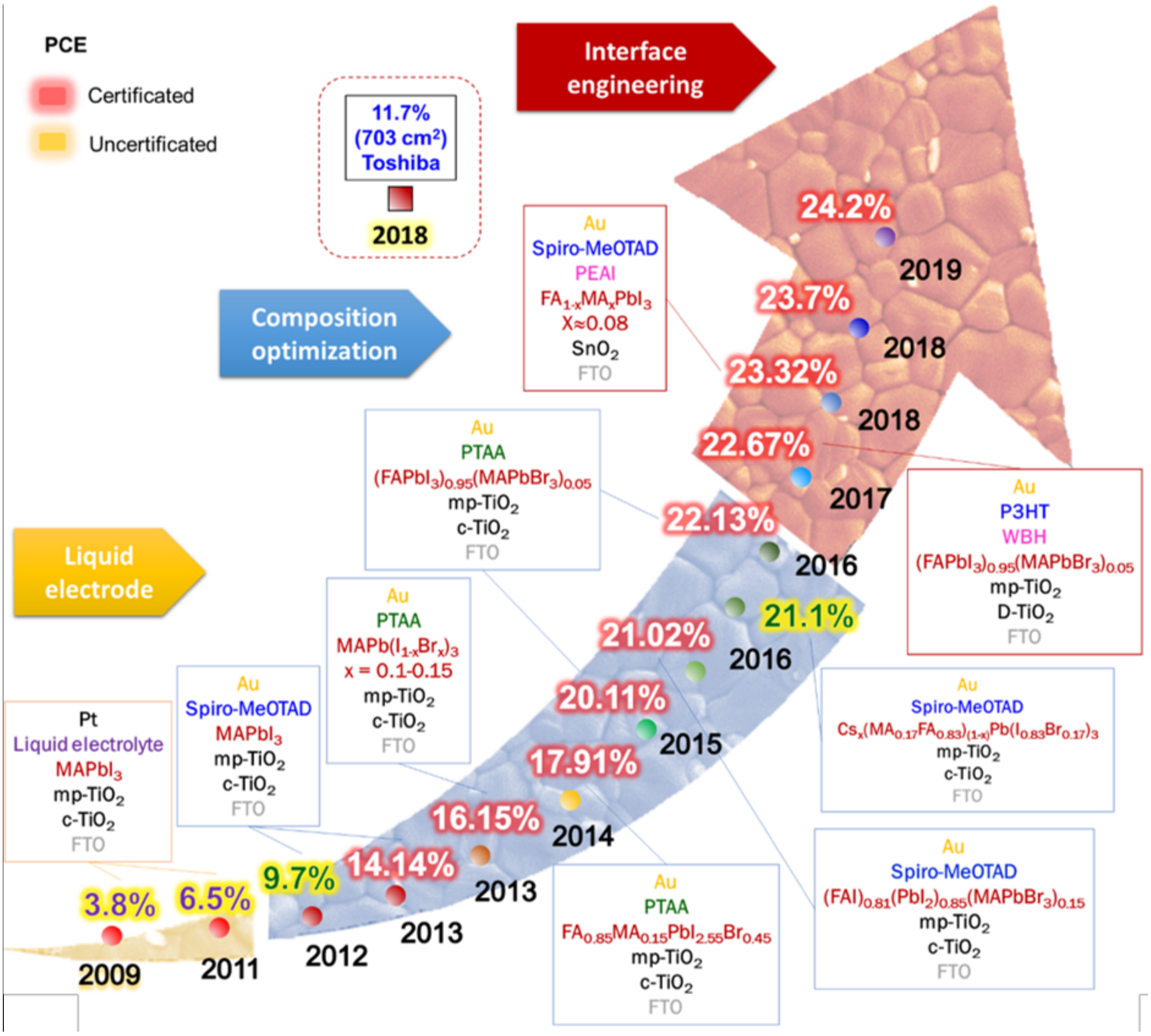

Figure 13. Selected lab-scale perovskite-based solar cell efficiencies and their corresponding device architecture evolved over the years.[25, 44, 179b] The corresponding references to each of the efficiency numbers are as following: 3.8%,[181] 6.5%,[182] 9.7%,[179a] 14.1%,[183] 16.15%,[184] 17.91%,[185] 20.11%[186] 21.02%,[187] 21.1%,[188] 22.13%,[96a] 22.67%,[83] 23.32%.[189] The certified efficiencies divulged by NREL are represented by red-colored numbers.[190] Toshiba Corporation holds the certified efficiency with the largest perovskite solar module (dash square symbol).[28a]

Table 1. Selected microscopic studies that emphasize multi-modal measurements as well as focused on the dynamical processes taking place within a PSC. This table is complementary to the one published in ref. [11].

Technique; measurement conditions	Subject	Spatial resolution; detection depth; quantitative/qualitative	Static/Dynamic (movie availability)	Perovskite; processing	Main findings	Ref
STM/STS; UHV, 4.5 K.	Atomic surface structure and electronic structure.	Atomic resolution (~0.2 Å); top surface; quantitative	Static	$MAPbBr_3$ single crystal.	• Surface reconstruction with dimmer and zigzag structures. • MABr-terminated surface.	[42a]
STM; 78 K.	Atomic surface structure and electronic structure.	Atomic resolution (~0.2 Å); top surface; quantitative	Static	$MAPbI_3$ polycrystalline film; vacuum deposition.	• Surface reconstruction with dimmer and zigzag structures. • MAI-terminated surface.	[42b-d]
Cross-sectional STM/STS	Topography and electronic structure.	Atomic resolution (~0.2 Å); top surface; quantitative	Static	$MAPbI_{3-x}Cl_x$ polycrystalline film; solution processed; 50 K.	• $MAPbI_{3-x}Cl_x$ / Si(100) cleaved in-situ. • Two domains with different DOS are observed in the length scale of 10-20 nm. • DFT corroborates the scenario of local I/Cl stoichiometric ratios. • The domain with low dI/dV corresponds to lower I/Cl, while high dI/dV was attributed to high Cl-contents.	[42e]
STM	Atomic surface structure.	Atomic resolution (~0.2 Å); top surface;	Static	$MAPbBr_3$, $MAPbBr_{3-y}I_y$ and $MAPbBr_{3-z}Cl_z$ polycrystalline films;	• Br ions substituted by I or Cl ions. • Substituted halides show randomly distributed.	[27]

		quantitative		vacuum deposition; 5 K, UHV.	• disordered surface structure with no phase segregation.	
Photoexcited cross-sectional STM/STS	Atomic surface structure under laser diode (532 nm, 140 mW/cm^2).	Atomic resolution (~0.2 Å); top surface; quantitative	Dynamic (yes)	MAPbBr$_3$ single crystal; 4.3 K.	• Photo-induced atomic-scale reordering of MA cations. • Rotation of MA induced by excitation of electron-hole pairs in spatially displaced orbital states.	[26]
Light-modulated STM; UHV; Laser diode (532 nm, 3 mW/cm^2); 100 K.	Topography and electronic structure mapping.	Atomic resolution (~0.2 Å); top surface; quantitative	Static; Comparison dark versus light.	MAPbI$_3$ polycrystalline film on mp-TiO$_2$/c-TiO$_2$/SiO$_2$/Si; solution processed.	• Interfacial electronic structure at the heterointerfaces between MAPbI$_3$ and PbI$_2$. • Spatially resolved mapping images of photoinduced band bending of VB and CB. • Real-space observations of photocarrier generation. • Enhanced charge separation and reduced back recombination deduced for PbI$_2$ passivation layer	[15]
Real-time in-situ HRTEM	Thermal degradation.	Atomic-scale; atomic-scale HRTEM observation of the outermost surface of the crystalline; qualitative	Dynamics (yes)	MAPbI$_3$ on FTO	• Precipitation of trigonal PbI$_2$ grains and its detailed process during thermal degradation. • Precipitation of the PbI$_2$ grains did not originate directly from the crystalline MAPbI$_3$ layer, but from the amorphized MAPbI$_3$ layer.	[191]

Frequency-modulation KPFM	CPD maps on cross-sectional complete devices.	A lateral resolution <50 nm; quantitative	Dynamic (no)	ITO/c-TiO$_2$/MAPbI$_3$/spiro-MeOTAD/Ag	• Upon illumination, space charge layers are formed at the interfaces of the selective contacts with MAPbI$_3$ layer within seconds. • Distinct differences in the charging dynamics at the interfaces of MAPbI$_3$ with adjacent layers are observed. • Such differences in charging rates at different interfaces were associated to a combination of ion migration and interfacial trap states.	[24c]
KPFM	CPD maps on cross-sectional complete devices.	Nanometer resolution; quantitative	Static; poling the device with +1 V and –1 V.	FTO/c-TiO$_2$/(FA-MA)Pb(I-Br)/spiro-MeOTAD/Au	• Influence of extrinsic ions (Li$^+$ ion migration). • Li$^+$ ions in the HTL layer diffuse across the perovskite layer and accumulate in the ETL layer. • Accumulation of Li$^+$ at the c-TiO$_2$ interface improves carrier injection from perovskite to c-TiO$_2$.	[24d]
High-speed illuminated heterodyne-KPFM (16 s/scan); air (<15% RH); 500 nm	Topography and Voc mapping.	A lateral resolution <50 nm; quantitative	Dynamic (yes)	MAPbI$_3$ polycrystalline film on PEDOT/ITO; solution processed.	• Local Voc mapping shows voltage variations >300 mV under 1-sun within a perovskite grain. • The time-dependent changes of local Voc were observed under dark conditions	[90e]

laser light at 54 μW.					and proposed due to reversible intragrain ion migration.	
Fast free force recovery (F^3R)-KPFM	CPD mapping with high temporal resolution (>10 μs)	Quantitative	Dynamic (yes)	$MAPbBr_3$ single crystal.	• Ion migration induced laterally across Au (drain)/$MAPbBr_3$/Au (source = ground) lateral device structure. • After drain voltage is switched on, a complex potential transient is observed, including both fast and slow processes, indicating that the imaging mechanism is not simply electronic in nature. • The establishment of the interface region does not appear instantaneous; instead, it is stablished ~30 μs after the removal of the field and disappears ~92 μs after the application of the field across the device. • These were correlated with the finite transport rates of ions in the material.	[170a]
KPFM	Time-dependent mapping of surface photovoltage.	Quantitative	Dynamic (no)	$MAPbBr_3$ single crystal.	• Interplay of convoluted processes of charge carrier dynamics and ion migration. • Time-dependent changes of the surface potential under illumination taking place on the scale of a few seconds. This time scale assigned to ion migration.	[170b]

					• Photopotential decay at the sub-millisecond time scale was related to the photocarrier lifetime.	
Time-resolved G-mode KPFM and fast free time-resolved (FF-tr)EFM.	CPD mapping with time resolution in the order of μs time scales.	Spatial resolution: 100 nm; Quantitative	Dynamic (yes)	Layered 2D perovskite of $(C_4H_9NH_3)_2PbI_4$.	• Under illumination, the photovoltage equilibrates over hundreds of μs, a time scale associated with ion migration and trapped electronic carriers. • On the contrary to 3D perovskites, the surface photovoltage of the 2D grain interiors evolves more rapidly in time than at the grain boundaries. • The slower evolution at grain boundaries was associated to a combination of ion migration occurring between PbI_4 planes in the 2D layered perovskite as well as electronic carriers traversing the traps present in grain boundaries.	[172b]
Time resolved (tr-)KPFM	CPD maps on cross-sectional complete devices.	The lateral KPFM resolution of 50 nm; quantitative	Dynamic (yes)	Cross-section on FTO/SnO_2/(MA-FA)Pb(I-Br) perovskite/spiro-MeOTAD/Au	• A localized interfacial charge forms at the photoanode interface within 10 ms after applying a forward bias to the device. • After switching off the forward bias, these interfacial charges were stable for over 500 ms and created a reverse electric field in the cell.	[12c]

					• This reverse electric field was associated with the higher photocurrents during reverse bias scans in I-V measurements (hysteresis).	
KPFM and pc-AFM	CPD maps on $MAPbI_3$ films deposited on ETL and HTL.	In nanometer resolution; quantitative	Dynamic, Light on/off with KPFM (no)	Three samples: S1. $MAPbI_3$/c-TiO_2/FTO. S2. $MAPbI_3$/PEDOT:PSS/FTO. S3. $MAPbI_3$/FTO.	• The average difference value (ΔV) of CPD values obtained between in dark and under illumination is associated with the efficacy for charge extraction at perovskite/contact layer interfaces. • The magnitude of ΔV is related to the density of charge carrier at the surface, while ΔV polarity is associated to the type of charge carrier (electrons or holes).	[13b]
KPFM; N_2 filled glovebox; >50 mW/cm^2 from 350 to 750 nm.	CPD maps on cross-sectional complete devices.	Lateral resolution 20~50 nm; quantitative	Static; Comparison dark versus light.	Cell 1. ITO/TiO_2/$MAPbI_3$/spiro-MeOTAD/Au; Cell 2. ITO/C_{60}-C_6-PA SAM/$MAPbI_3$/spiro-MeOTAD/Au	• Under Jsc or Voc conditions, SAM cell showed higher positive potential (LCPD profiles). This high potential (i.e., charge-up) for SAM cell was higher than for TiO_2 cell. • The positive charge-up means an unbalanced e-h extractions with a more efficient electron extraction in SAM cells.	[24e]
KPFM	CPD maps on cross-sectional complete devices.	Quantitative	Static	Cell 1 (planar). FTO/c-TiO_2/$MAPbI_3$ (excess PbI_2 or MAI)/spiro-MeOTAD/Ag;	• The diode junction behaves differently between planar and mesoporous PSCs. • Regardless of $MAPbI_3$ stoichiometry (PbI_2- or MAI-rich conditions), a major	[22]

				Cell 2 (mesoporous). FTO/c-TiO_2/mp-TiO_2+$MAPbI_3$ (excess PbI_2 or MAI)/spiro-MeOTAD/Ag	potential drop takes place at the perovskite+mp-TiO_2 exhibiting one diode junction. • In contrast, the major potential drop was found on both sides of the perovskite layer in planar PSCs, indicating two diode junctions, which the generated ca	
KPFM	CPD maps on cross-sectional complete devices.	A nominal tip radius of ~25 nm; quantitative	Static	FTO/c-TiO_2/n-type perovskite/p-type perovskite/spiro-MeOTAD/Au	• A potential drop is observed at the interface of the n-type/p-type perovskite layers caused by the carrier separation at the interface. • It demonstrates the existence of a built-in electric field and hence the existence of a p-n junction.	[24f]
CL/SE	Halide segregation	All CL images were acquired with 512 × 512 pixels of a 10 µm × 10 µm field of view.	Dynamic (yes)	$MAPb(I_xBr_{1-x})_3$ polycrystalline films; solution-processed.	• Photoinduced halide segregation arises when charged excitations generate sufficient lattice strain to destabilize the solid solution.	[41]
Nanoprobe (nano)-XRF	Halide segregation	250 nm resolution; qualitative.	Dynamic (no)	$MAPbBr_3$ single crystal.	• Nano-XRF mapping employed to identify the spatial distribution of elements within $MAPbBr_3$ single crystal under applied bias. • A direct relationship between migration and local optoelectronic response by PL mapping is provided.	[192]

					• As Br⁻ migrates from the negatively biased electrode and the perovskite becomes locally sub-stoichiometric, the PL intensity decreases.	
PL mapping	Influence of atmospheric gases (O_2, H_2O, N_2)	Qualitative.	Dynamic (no)	$MAPbI_3$(~250 nm) on cover slip glass.	• The response of each grain to continuous illumination and atmospheric environment was studied. • PL mapping in N_2 shows the grain-to-grain heterogeneity with bright and dark grains. • PL mapping under N_2 + H_2O (~45% RH) reveals both the bright and dark grains to show a gradual rise in intensity. • PL mapping under dry air reveals that bright grain exhibits stable PL over time, while the dark grain, which likely has a higher defect density than the bright grain, shows significant PL enhancement under illumination and eventually reached the same intensity as the bright grain. • PL mapping under air + H_2O (~45% RH) shows an initial baseline increase (i.e., before any light illumination) in the emission intensity for both bright and dark grains. Then the emission from both bright	[45b]

					and dark grains slowly rises over time under illumination with again a greater relative increase for the dark grain than the bright grain.	

Abbreviations: UHV = ultrahigh vacuum; STM = scanning tunneling microscopy; STS = scanning tunneling spectroscopy; HRTEM = high resolution transmission electron microscopy; KPFM = Kelvin probe force microscopy; LCPD = local contact potential difference; XRF = X-ray fluorescence; PL = photoluminescence; SAM = self-assembled monolayer; CL = cathode luminescence; SE = secondary electrons; FTO = fluorine-doped tin oxide, C_{60}-C_6-PA = C60-functionalized 6-octyl phosphonic acid; PEDOT:PSS = poly(3,4-ethylenedioxythiophene) polystyrene sulfonate.

Table 2. The type of defects, related characterizing method and its effect related to photovoltaic parameters.

Type of defects	Healing process	Perovskite	Method	Sample	Activation energy/ Or V_{TEF} (only to SCLC)	Defect density/cm^{-3}	Voc/V	Jsc/mA/cm^2	FF/%	PCE	Ref
Grain boundary											
	DMF vapor	$MAPbI_3$	TAS	Control	0.30-0.40 eV	5.3×10^{18}	0.96	16.8	69.5	10.5	[154]
				Passivation		1.8×10^{18}	0.96	21.0	76.0	15.1	
	Hydroxylamine hydrochloride	$MAPbI_3$	SCLC	Control	V_{TEF} 0.60 V	2.1×10^{16}	1.05	22.01	74.80	16.85	[159b]
				Passivation	V_{TEF} 0.34 V	1.2×10^{16}	1.10	22.42	76.07	18.69	
	ITIC	$MAPbI_3$	SCLC	Control	V_{TEF} 0.90 V	3.2×10^{16}	1.06	21.07	74.7	16.66	[163]
				Passivation	V_{TEF} 0.17 V	5.9×10^{15}	1.07	22.02	75.5	18.03	
	E2CA	$MAPbI_3$	SCLC	Control	V_{TEF} 0.68 V	1.06×10^{16}	1.07	21.92	77.9	18.23	[161]
				Passivation	V_{TEF} 0.49 V	0.77×10^{16}	1.09	22.06	80.5	19.51	
	PFA	$MAPbI_3$	SCLC	Control	V_{TEF} 2.02 V	2.9×10^{16}	0.98	20.14	63.39	12.71	[162]
				Passivation	V_{TEF} 0.12 V	9.3×10^{15}	1.05	21.71	70.97	16.18	
Surface/Interface											
	PFA	$MAPbI_3$	SCLC	Control	V_{TEF} 2.02 V	2.9×10^{16}	0.98	20.14	63.39	12.71	[162]
				Passivation	V_{TEF} 0.87 V	1.4×10^{15}	1.04	20.45	68.10	14.48	
	choline chloride	$MAPbI_3$	TAS	Control	Deeper0.35-0.40 eV	Higher	1.04	22.5	73	17.1	[18]
				Passivation	shallow0.40-0.52 eV	Lower	1.15	22.9	76	20.0	
	PCBM	$MAPbI_3$	TAS	Control	Deeper >0.40 eV	1×10^{19}	1.10	22.81	73.8	18.5	[133]

				Passivation	Shallow 0.35-0.40 eV	1×10^{17}	1.21	22.60	76.1	20.9	
	C_{60}-ETA	$MAPbI_3$	SCLC	Control	-	4.14×10^{16}	1.09	22.35	75.56	18.03	[134]
				Passivation	-	1.99×10^{16}	1.09	22.75	78.56	19.12	
	π-conjugated Lewis base	$MAPbI_3$	TAS	Control	0.33–0.45	1×10^{19}	1.03	19.37	-	13.5	[135]
				Passivation		1×10^{18}	1.11	22.96	-	19.5	
	CsBr	$MAPbI_{3-x}Cl_x$	TAS	Control	0.16-0.40 eV	5.0×10^{16}	0.99	18.7	69	13.1	[137]
				Passivation		2.0×10^{16}	1.06	20.7	75	16.3	
	PbI_2	$Cs_{0.02}MA_{0.03}FA_{0.95}Pb(I_{0.95}Br_{0.05})_3$	TAS	Control	0.06-0.20 eV	Higher	1.04	23.8	75.2	18.8	[115]
				Passivation		Lower	1.15	24.8	78.4	22.3	
Bulk point defect											
I_Frenkel defect	K^+(KI)	$(FAPbI_3)_{0.875}(CsPbBr_3)_{0.125}$	SCLC	Control	V_{TEF} 0.79 V	1.37×10^{16}	1.03	21.8	67	15	[126a]
				Passivation	V_{TEF} 0.62 V	0.85×10^{16}	1.14	21.7	72	18	
Deep-defect	MA	$Cs_{0.2}FA_{0.8}Pb(I_{0.75}Br_{0.25})_3$	TAS	Control	Deep 0.18 eV	2.1×10^{16}	1.16	19.9	76	17.5	[193]
				Passivation		Disappeared					
				Control	Shallow 0.11 eV	0.6×10^{16}	1.21	21.0	79	20.0	
				Passivation		1.1×10^{16}					
PbI_3^- antisite defect	Ni^{2+}	$MAPbI_3$	TAS	Control	Shallow 0.05 eV	Higher	1.08	21.55	74	17.2	[126b]
				Passivation		Lower	1.13	22.64	81	20.6	

Pb_i and antisite defects	I_3^-	$MAFAPbI_{3-x}Br_x$	DLTS	ControlControl	Deep/Deep/Semi shallow 0.78/0.82/0.46 eV	Same/5.28 × 10^{14}/- Same/5.28 × 10^{14}/-	1.07	23.5	80.8	20.3	[96a]
				Passivation		Same/8.81×10^{13}/ Disappeared	1.10	24.1	81.9	21.6	
	Rb5Cs5	$FA_{0.83}MA_{0.17}Pb(I_{0.83}Br_{0.17})_3$	TSC	Control	-	7.3×10^{16}	1.12	19.21	70	15.08	[126d]
				Passivation	-	1.6×10^{16}	1.14	20.65	72	17.02	

Abbreviations: DMF = Dimethylformamide; TFL = Trap-filled limit; SCLC = space charge limited current; TAS = thermal (thermal admittance spectroscopy; TSC = thermal stimulated current; DLTS = deep-level transient spectroscopy.

Yabing Qi is Professor and Unit Director of Energy Materials and Surface Sciences Unit at Okinawa Institute of Science and Technology Graduate University in Japan. He received his B.S., M.Phil., and Ph.D. from Nanjing Univ., Hong Kong Univ. of Sci. and Tech., and UC Berkeley, respectively. His research interests include perovskite solar cells, surface/interface sciences, lithium ion batteries, organic electronics, energy materials and devices (https://groups.oist.jp/emssu).

Table of Contents

Progress of Surface Science Studies on ABX_3 Based Metal Halide Perovskite Solar Cells

*Longbin Qiu†, Sisi He†, Luis K. Ono†, Yabing Qi**

Dr. L. Qiu, Dr. S. He, Dr. L. K. Ono, Prof. Y. B. Qi
Energy Materials and Surface Sciences Unit (EMSSU), Okinawa Institute of Science and Technology Graduate University (OIST), 1919-1 Tancha, Onna-son, Kunigami-gun, Okinawa 904-0495, Japan.
*Corresponding author: Yabing Qi, E-Mail: Yabing.Qi@OIST.jp
†These authors contributed equally to this work.

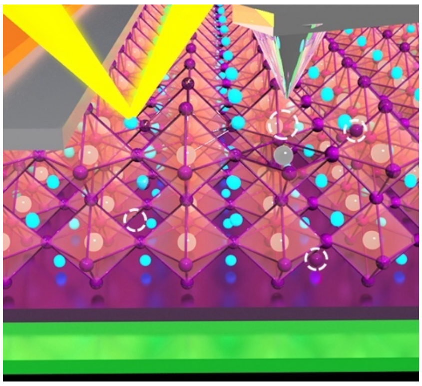

Recent case studies demonstrate how probing of local heterogeneities and ensembled average properties in larger scale of perovskites by surface science techniques can help build connections between material properties and perovskite solar cell performance. In this review article, we also focus on how generation and healing of electronic defects within the semiconductor band gap influence perovskite solar cell efficiency, lifetime, as well as reproducibility.